

Tiedekunta/Osasto — Fakultet/Sektion — Faculty	Laitos — Institution — Department	
Faculty of Science	Institute of Physics	
Tekijä — Författare — Author		
<b>Stefan Richter</b>		
Työn nimi — Arbetets titel — Title		
Invariant mass reconstruction in a search for light charged Higgs bosons in pp collisions at $\sqrt{s} = 7 \text{ TeV}$		
Oppiaine — Läroämne — Subject		
Physics		
Työn laji — Arbetets art — Level	Aika — Datum — Month and year	Sivumäärä — Sidoantal — Number of pages
Master's thesis	July 2013	121
Tiivistelmä — Referat — Abstract		
<p>An algorithm for invariant mass reconstruction in a search for light charged Higgs bosons (<math>H^\pm</math>) produced in top quark decays and decaying to a tau lepton and neutrino, <math>H^\pm \rightarrow \tau^\pm \nu_\tau</math>, is presented. Here, 'light' means lighter than the top quark. The algorithm uses the top quark mass as a kinematical constraint to allow the calculation of the longitudinal momentum of the neutrinos. The invariant mass of the tau-and-neutrino system is then calculated using the missing transverse energy, the calculated longitudinal momentum of the neutrinos, and the measured momentum of the visible decay products of the tau lepton.</p>		
<p>Methods for resolving ambiguities and recovering unphysical results arising in the invariant mass reconstruction are presented.</p>		
<p>The invariant mass distribution could be used to extract a possible signal, replacing or complementing the transverse mass distribution that has been used so far in the analysis.</p>		
<p>In a preliminary data analysis using pp collision data at <math>\sqrt{s} = 7 \text{ TeV}</math> corresponding to an integrated luminosity of <math>5.1 \text{ fb}^{-1}</math> recorded by the CMS experiment, it is shown that using invariant mass distribution obtained with the presented algorithm allows to set a more stringent upper limit on the signal branching fraction <math>\mathcal{B}(t \rightarrow H^\pm b) \times \mathcal{B}(H^\pm \rightarrow \tau^\pm \nu_\tau)</math> than does using the transverse mass distribution. An expected upper limit at the 95% confidence level between around 0.37% to 2.5% (transverse mass) and 0.13% to 1.9% (invariant mass) is found, depending on the <math>H^\pm</math> mass.</p>		
<p>These results suggest that using the invariant mass reconstructed with the new algorithm may improve the signal sensitivity of the search.</p>		
Avainsanat — Nyckelord — Keywords		
Charged Higgs bosons, very high-energy pp interactions, decays of tau leptons, kinematics		
Säilytyspaikka — Förvaringsställe — Where deposited		
Kumpula Campus Library (Gustaf Hällströmin katu 2, 00014 University of Helsinki)		
Muuta tietoa — Övriga uppgifter — Additional information		
Summaries for the general public are available in several languages in the appendix.		

Tiedekunta/Osasto — Fakultet/Sektion — Faculty	Laitos — Institution — Department			
Matemaattis-luonnonlaitteellinen tiedekunta	Fysiikan laitos			
Tekijä — Författare — Author				
<b>Stefan Richter</b>				
Työn nimi — Arbetsets titel — Title				
Invariantin massan rekonstruktio kevyiden varattujen Higgsin bosonien etsinnässä pp-törmäyksissä energialla $\sqrt{s} = 7 \text{ TeV}$				
Oppiaine — Läröämme — Subject				
<b>Fysiikka</b>				
Työn laji — Arbetsets art — Level	Aika — Datum — Month and year	Sivumäärä — Sidoantal — Number of pages		
Pro gradu	Heinäkuu 2013	121		
Tiivistelmä — Referat — Abstract				
<p>Tässä työssä esitetään algoritmi invariantin massan rekonstruoimiseksi. Sitä käytetään analyysissä, jossa etsitään kevyitä varattuja Higgsin bosoneita (<math>H^\pm</math>), jotka syntyvät huippu-kvarkkien hajoamisissa ja jotka hajoavat edelleen tau-leptoniksi ja neutriinoksi, <math>H^\pm \rightarrow \tau^\pm \nu_\tau</math>. Kevyt tarkoittaa tässä yhteydessä kevyempi kuin huippu-kvarkki. Algoritmi käyttää huippu-kvarkin massaa kineemaattisena rajoituksena, jonka avulla pystytään laskemaan neutriinojen pitkittäinen liikemäärä. Taun ja neutriinon muodostaman järjestelmän invariantti massa pystytään sen jälkeen laskemaan käyttäen puuttuvaa poikittaista energiota, neutriinojen laskettua pitkittäistä liikemäärää sekä tau-leptonien suoraan havaittavien hajoamistutteiden kokeellisesti määritettyä liikemäärää.</p>				
Invariantin massan rekonstruktiossa saattaa ilmetä monikäsitusyksiä tai epäfysikaalisia tuloksia. Tässä työssä esitetään keinot näiden haasteiden ratkaisemiseksi.				
Invariantin massan jakaumaa voidaan käyttää mahdollisen signaalin havaitsemiseen, johon analyysissä on tähän asti käytetty ainoastaan poikittaisen massan jakaumaa. Poikittaisen massan sijaan analyysissä voidaan käyttää invarianttia massaa tai kummankin massan yhdistelmää.				
<p>Työssä on tehty alustava data-analyysi, jossa on käytetty CMS -kokeen tallentamaa dataa protoni-protoni-törmäyksistä. Datan määrä vastaa integroitua luminositeettiä <math>5.1 \text{ fb}^{-1}</math>, ja massakeskipiste-energia törmäyksissä oli <math>\sqrt{s} = 7 \text{ TeV}</math>. Data-analyysin tulokset osoittavat, että uuden algoritmin avulla saadun invariantin massan jakauman käyttö sallii tiukemman ylärajan asettamisen signaalihajoamissuhteelle <math>\mathcal{B}(t \rightarrow H^\pm b) \times \mathcal{B}(H^\pm \rightarrow \tau^\pm \nu_\tau)</math> kuin poikittaisen massan jakauman käyttö. Odotusarvoinen yläraja 95%:n luottamustasolla on tulosten perusteella välillä 0.37–2.5% (poikittainen massa) ja välillä 0.13%–1.9% (invariantti massa) varatun Higgsin bosonin massasta riipuen.</p>				
Nämä alustavat tulokset viittaavat siihen, että uuden algoritmin avulla rekonstruoidun invariantin massan jakauman käyttö saattaa parantaa etsinnän herkkyyttä mahdolliselle signaalille.				
Avainsanat — Nyckelord — Keywords				
Varatut Higgsin bosonit, korkeaenergiset pp-törmäykset, tau-leptonin hajoamiset, kinematiikka				
Säilytyspaikka — Förvaringsställe — Where deposited				
Kumpulan kampuskirjasto (Gustaf Hällströmin katu 2, 00014 Helsingin yliopisto)				
Muuta tietoa — Övriga uppgifter — Additional information				
Yleistajuisia yhteenvetotoja usealla eri kielessä on sisällytetty tutkielman liitteisiin.				



Pro gradu -tutkielma  
Examensarbete  
Master's thesis

# Invariant mass reconstruction in a search for light charged Higgs bosons in pp collisions at $\sqrt{s} = 7 \text{ TeV}$

Stefan Richter  
27.7.2013

Ohjaaja | Handledare | Advisor  
Dr. Sami Lehti

Tarkastajat | Examinatorer | Examiners  
Prof. Paula Eerola  
Dr. Sami Lehti

## Abstract

An algorithm for invariant mass reconstruction in a search for light charged Higgs bosons ( $H^\pm$ ) produced in top quark decays and decaying to a tau lepton and neutrino,  $H^\pm \rightarrow \tau^\pm \nu_\tau$ , is presented. Here, ‘light’ means lighter than the top quark. The algorithm uses the top quark mass as a kinematical constraint to allow the calculation of the longitudinal momentum of the neutrinos. The invariant mass of the tau-and-neutrino system is then calculated using the missing transverse energy, the calculated longitudinal momentum of the neutrinos, and the measured momentum of the visible decay products of the tau lepton.

Methods for resolving ambiguities and recovering unphysical results arising in the invariant mass reconstruction are presented.

The invariant mass distribution could be used to extract a possible signal, replacing or complementing the transverse mass distribution that has been used so far in the analysis.

In a preliminary data analysis using pp collision data at  $\sqrt{s} = 7$  TeV corresponding to an integrated luminosity of  $5.1 \text{ fb}^{-1}$  recorded by the CMS experiment, it is shown that using invariant mass distribution obtained with the presented algorithm allows to set a more stringent upper limit on the signal branching fraction  $\mathcal{B}(t \rightarrow H^\pm b) \times \mathcal{B}(H^\pm \rightarrow \tau^\pm \nu_\tau)$  than does using the transverse mass distribution. An expected upper limit at the 95% confidence level between around 0.37% to 2.5% (transverse mass) and 0.13% to 1.9% (invariant mass) is found, depending on the  $H^\pm$  mass.

These results suggest that using the invariant mass may improve the sensitivity to a possible signal of the search.

<3

This master's thesis was prepared on the basis of research done at the Helsinki Institute of Physics (Helsinki, Finland) and CERN (Geneva, Switzerland) in the spring and summer of 2013. It was a turbulent period of time in my life, as is evidenced by the fact that writing of this thesis was done in such places as airplanes, a student residence at Trinity College Dublin, my parents' garden, trains, the shore of Lake Geneva, and the old university library in Heidelberg. I would like to express my deep gratefulness to the people who have accompanied me on the way and far beyond it.

First of all, I would like to thank my awesome supervisor Dr. Sami Lehti for providing me the opportunity to do this exciting research, providing valuable help and straight feedback, letting me work independently and try things my own way, reading my thesis and sending me comments even during his holiday, and granting me a lot of flexibility in all practical matters. I also thank Prof. Paula Eerola for always being there to provide help and good advice, reading my thesis, and showing genuine interest in my progress. My warmest regards go to the rest of my fellow charged Higgs hunters: Dr. Alexandros Attikis, Dr. Cristina Ferro, Doc. Ritva Kinnunen, Dr. Matti Kortelainen, and Dr. Lauri Wendland. It was great fun and very instructive to work with you. Thank you for your advice and interest. Special thanks go to Matti for the computing assistance and the excellent tools he provided that made work a lot more efficient and pleasant.

I thank all past and present members of the CMS collaboration for building and maintaining the experiment, the colleagues in the CERN accelerator departments for the excellent performance of the LHC, and the technical and administrative staffs at CERN.

As my studies draw to a close with the completion of this thesis, I want to grasp the opportunity to thank all of my family, especially my grandmothers Edith and Lieselene, my parents Erika and Hans-Peter, my wonderful sister Annika and my dear brother Martin for all the support, understanding, and kindness they have shown me in the past years. Um es auf meine Art zu sagen: ihr seid für mich die beste Familie, die ich mir je vorstellen könnte. I also wish to thank my dear friends, especially Torsti, Stephan, and Joona for sharing big and small plans and being like brothers to me; the Europa-Kolleg alumni for living the dream of a world where distance and frontiers have lost their meaning; my choir Dominante and its sailing tenors; and Markus ("Tehhääkö laskareita vai ookko nää menos syömään?"), who has made the last two years in Helsinki so much richer and physics even more fun. Ja Hanna, kiitos.

Stefan Richter  
Geneva, 23.7.2013

GCCTACTTGACTTTACAACATCAACTCTGTGTACGGGTATACTTACTATCCCGTGTGGAAAT  
ATTGCTGTGGGTACTTCGGTTGAGGACCCCTCCAGTATTATGCTTACGCCGGTGTGTTTTGGT  
CACCGGGCTCAAAGTTGCCCTATGCTTAACATCAACTCACTGAAGTTCAGCTCCGCTTGCTAAC  
TAAAAAACTCACCTAGGAAGAACCTATCACCTCATGCTCACAGTACGTTAACACTCAGGATCAAAT  
CCGTTTACATACTTGCCAAGGAGCGTACCTCAGAACTCCGTGCGTTGTGTCAAAGTTGCACCCTA  
ACACCTT

# Contents

<b>Abstract</b>	<b>iii</b>
<b>Acknowledgements</b>	<b>iv</b>
<b>Some opening remarks</b>	<b>viii</b>
Summaries for non-physicists in several languages . . . . .	viii
General remarks on notation, conventions, and plots . . . . .	viii
List of notations . . . . .	ix
Table of masses of selected particles . . . . .	x
<b>I Introduction</b>	<b>1</b>
<b>1 Introduction</b>	<b>2</b>
1.1 Previous results of charged Higgs boson searches . . . . .	5
<b>2 General kinematics of hadron collisions</b>	<b>6</b>
2.1 Coordinate system, angles, and pseudorapidity . . . . .	6
2.2 Angular distance . . . . .	6
2.3 Transverse momentum . . . . .	7
2.4 Undetected particles and missing transverse energy . . . . .	7
2.5 Mass variables . . . . .	8
2.5.1 General remarks and role in new physics searches . . . . .	8
2.5.2 Transverse mass . . . . .	9
2.5.3 Invariant mass . . . . .	9
<b>3 Theory behind charged Higgs bosons and search channel</b>	<b>10</b>
3.1 Higgs–Brout–Englert–Guralnik–Hagen–Kibble mechanism and mass generation in the standard model . . . . .	11
3.2 Beyond the minimal model: extended Higgs sectors and charged Higgs bosons	14
3.2.1 Two-Higgs-doublet model . . . . .	15
3.2.2 Higgs sector of the MSSM . . . . .	16
3.3 Studied $H^\pm$ search channel . . . . .	17
3.3.1 $H^\pm$ production in top quark decays in $t\bar{t}$ events . . . . .	17
3.3.2 $H^\pm$ decays to a tau lepton and neutrino . . . . .	18
3.3.3 Tau lepton decays . . . . .	19
3.3.4 Detector fingerprint of the investigated channel . . . . .	19
3.3.5 Background processes . . . . .	20
3.4 Separating signal from background . . . . .	22
3.4.1 Boson mass . . . . .	22
3.4.2 Relative coupling strengths to leptons . . . . .	22
3.4.3 Helicity correlations . . . . .	22
<b>4 Large Hadron Collider and CMS experiment</b>	<b>26</b>
4.1 Large Hadron Collider . . . . .	26
4.2 CMS experiment . . . . .	26
4.2.1 Anatomy of the CMS detector . . . . .	27
4.3 Experimental conditions . . . . .	29
4.3.1 Center-of-mass energy . . . . .	29

4.3.2	Instantaneous and integrated luminosity . . . . .	30
4.3.3	Pile-up . . . . .	30
<b>5</b>	<b>Event reconstruction</b>	<b>31</b>
5.1	Tracking . . . . .	31
5.2	Primary vertices . . . . .	31
5.3	Muons . . . . .	32
5.4	Electrons . . . . .	33
5.5	Photons . . . . .	33
5.6	Particle-flow event reconstruction . . . . .	34
5.7	Jets . . . . .	34
5.7.1	Types of reconstructed jets . . . . .	34
5.7.2	Jet clustering algorithms . . . . .	35
5.7.3	Jet momentum assignment . . . . .	36
5.8	Identification of b-jets . . . . .	36
5.9	Identification of $\tau$ -jets . . . . .	36
5.10	Missing transverse energy . . . . .	38
5.10.1	Missing transverse energy corrections . . . . .	38
<b>II</b>	<b>Data Analysis</b>	<b>39</b>
<b>6</b>	<b>Event simulation</b>	<b>40</b>
<b>7</b>	<b>Event selection</b>	<b>41</b>
7.1	Online event selection: trigger . . . . .	41
7.2	Offline event selection . . . . .	41
7.2.1	Data quality selection steps . . . . .	41
7.2.2	Main selection steps . . . . .	41
7.2.3	Collinear and back-to-back cuts for jets and missing transverse energy	42
7.2.4	Top quark invariant mass selection . . . . .	42
<b>8</b>	<b>Data-driven background determination</b>	<b>44</b>
8.1	Measurement of background with genuine $\tau$ leptons . . . . .	44
8.2	Measurement of QCD multijet background . . . . .	45
8.2.1	Number of QCD multijet events . . . . .	45
8.2.2	Transverse mass distribution of QCD multijet events . . . . .	46
8.2.3	Invariant mass distribution of QCD multijet events . . . . .	46
8.3	Electroweak and $t\bar{t}$ background without a genuine $\tau$ . . . . .	47
<b>9</b>	<b>Invariant mass reconstruction</b>	<b>48</b>
9.1	The idea behind the invariant mass reconstruction . . . . .	49
9.1.1	Invariant mass of the top quark . . . . .	49
9.1.2	Longitudinal momentum of the neutrino pair . . . . .	49
9.1.3	A tale of two solutions . . . . .	50
9.2	Invariant mass reconstruction algorithm . . . . .	51
9.3	Conditions for reliable invariant mass reconstruction . . . . .	52
9.3.1	Validity of using the top mass as a kinematical constraint . . . . .	52
9.3.2	Experimental requirements . . . . .	52
9.4	Selecting the better $p_\nu^z$ solution . . . . .	53

9.5	Negative discriminants: the problem and its solution . . . . .	55
9.5.1	What causes a negative discriminant? . . . . .	56
9.5.2	Recovering events with negative discriminants . . . . .	57
9.5.3	Top quark invariant mass selection . . . . .	58
9.6	Invariant mass distributions . . . . .	58
<b>III</b>	<b>Results and discussion</b>	<b>72</b>
<b>10</b>	<b>Results</b>	<b>73</b>
10.1	Expected limits for the signal branching ratio . . . . .	73
10.2	Systematic uncertainties . . . . .	76
10.3	Correspondence between invariant mass and rest mass . . . . .	77
10.4	Distribution of events in the transverse mass–invariant mass plane . . . . .	78
<b>11</b>	<b>Conclusions</b>	<b>84</b>
<b>References</b>		<b>91</b>
<b>IV</b>	<b>Appendix</b>	<b>92</b>
<b>A</b>	<b>Signal trigger specifications</b>	<b>93</b>
<b>B</b>	<b>Invariant mass distributions using different selection methods</b>	<b>94</b>
<b>C</b>	<b>Transverse mass distributions</b>	<b>101</b>
<b>D</b>	<b>Invariant mass fits</b>	<b>103</b>
<b>E</b>	<b>Summary for non-physicists</b>	<b>106</b>
<b>F</b>	<b>Yhteenvetö ei-fyysikoiille</b>	<b>108</b>
<b>G</b>	<b>Zusammenfassung für Nichtphysiker innen</b>	<b>110</b>

## Summaries for non-physicists in several languages

A non-technical summary of the work presented in this thesis aimed at readers who are not particle physicists can be found in Appendix E.

Suomenkielinen yleistajuinen yhteenveto tässä työssä esitetystä tutkimuksesta lukijoille, jotka eivät ole hiukkasfyysikoita, löytyy Liitteestä F.

Eine deutschsprachige allgemeinverständliche Zusammenfassung der hier präsentierten Forschung für Leser|innen, die keine Teilchenphysiker|innen sind, ist in Anhang G zu finden.

## General remarks on notation, conventions, and plots

The following is a list of notations and conventions that are used throughout this thesis. Some of the concepts appearing here are only explained later, so that the list is meant to be used as a reference when questions arise.

**Rest mass and invariant mass** All physical rest masses of particles are denoted using a majuscule letter,  $M$ . All invariant masses of single particles or multiparticle systems are denoted using a minuscule letter,  $m$ . A definition of the invariant mass is given in Section 2.5.3.

**Charge-conjugated processes** Whenever particle processes are expressed, it is implied that the charge-conjugated process is equally considered. For instance, when something related to the process  $H^+ \rightarrow \tau^+ \nu_\tau$  is stated, it applies to the process  $H^- \rightarrow \tau^- \bar{\nu}_\tau$  as well. All cross sections, branching fractions, and decay widths are assumed to be equal for charge-conjugated processes, which is equivalent to assuming that there is no strong violation of CP symmetry.

**Signal branching ratio** Many plots contain a line such as “ $\mathcal{B}(t \rightarrow H^\pm b) = 0.02$ ” in their legend. Whenever something of that kind is written, it is assumed that  $\mathcal{B}(H^\pm \rightarrow \tau^\pm \nu_\tau) = 1$ . The numeric value of the branching ratio given in the plot can equally well be interpreted as the signal branching ratio  $\mathcal{B}(t \rightarrow H^\pm b) \times \mathcal{B}(H^\pm \rightarrow \tau^\pm \nu_\tau)$ .

**Plots showing simulated data** All plots showing results from samples simulated using the Monte Carlo method have their numbers of events normalized to an integrated luminosity of  $5 \text{ fb}^{-1}$ . This corresponds approximately to the amount of data recorded for the analysis in the year 2011.

In many cases, plots are shown for six different  $H^\pm$  masses: 80, 100, 120, 140, 150, and 160 GeV.

In addition, whenever a simulated  $H^\pm$  signal is shown, it is assumed that  $\mathcal{B}(t \rightarrow H^\pm b) = 0.02$  and  $\mathcal{B}(H^\pm \rightarrow \tau^\pm \nu_\tau) = 1$ . The background of standard model top quark pair decays  $t\bar{t} \rightarrow W^+ b W^- \bar{b}$  is scaled correspondingly, i.e. 0.02 is subtracted from its branching ratio.

Furthermore, natural units in which  $\hbar = c = 1$  are used throughout this thesis.

## List of notations

A	neutral CP-odd (pseudoscalar) Higgs boson
$\mathcal{B}$	branching ratio
b	beauty quark
c	speed of light in vacuum
$\Delta R$	angular distance, $\Delta R = \sqrt{(\Delta\eta)^2 + (\Delta\phi)^2}$
e	electron
$e$	elementary charge
$E_T^{\text{miss}}$	missing transverse energy (magnitude)
$\vec{E}_T^{\text{miss}}$	missing transverse energy vector
$\varepsilon$	efficiency, $\varepsilon = (\text{number selected or identified } X)/(\text{number of all } X)$ ,
$\eta$	pseudorapidity, $\eta = -\ln[\tan(\theta/2)]$
$\gamma$	photon
$\gamma^*$	virtual (off-shell) photon
	where X could be e.g. processes or particles
h	lightest neutral CP-even Higgs boson
H	neutral CP-even Higgs boson
$H^\pm$	charged Higgs boson
$\hbar$	reduced Planck constant
$\mathcal{L}$	Lagrangian density <i>or</i> instantanenous luminosity
L	Integrated luminosity
$m$	invariant mass
$m_T$	transverse mass
M	rest mass
$\mu$	muon
N	number of events
$\nu$	neutrino
$\nu_\tau$	tau neutrino
$p^\mu, p$	four-momentum vector
$\mathbf{p}$	three-momentum vector
$\vec{p}_T$	transverse momentum vector in the $x$ - $y$ plane
$p_T$	transverse momentum (magnitude)
$\phi$	azimuthal angle, measured in the $x$ - $y$ plane
$R_\tau$	tau lepton polarization variable, $R_\tau = p^{\text{leading track}}/p^{\tau\text{-jet}}$
$\rho$	distance from the $z$ axis (and hence the beam), $\rho = \sqrt{x^2 + y^2}$
t	top quark
$\tau$	tau lepton
$\tau_h$	hadronically decaying tau lepton
$\theta$	polar angle, measured from the positive $z$ axis
W	charged weak boson
Z	neutral weak boson

## Table of masses of selected particles

Since the work presented in this thesis is revolving around the concept of mass, the approximate masses of the particles that are most central to the analysis are listed here for quick reference. All values are taken from Ref. [1] and are rounded to the nearest 0.1 GeV. The particles are sorted in the order of descending mass.

Particle	$M$ (GeV)
t	173.5
Z	91.2
W	80.4
b	4.2
$\tau$	1.8
$\mu$	0.1
e	$\approx 0.0$
$\nu_\tau$	$\approx 0.0$

**Part I**

# **Introduction**

# 1 Introduction

If the Higgs boson is the God Particle,  
we are trying to find out if the Universe  
is monotheistic or polytheistic.

---

Particle physics is a branch of natural science concerned with the study of elementary particles and their interactions. Intensive research in the field over more than the past hundred years has led to the development of a theoretical framework now called the *standard model* of particle physics [2–4], whose predictions agree astonishingly well with a vast number of experimental results. One peculiar feature of the standard model is that the property of elementary particles to have a (non-zero) *mass* cannot be put into the theory ‘by hand’ but has to be generated by some mechanism in order to ensure the consistency of the theory. Arguably the most simple way of achieving this is the Higgs–Brout–Englert–Guralnik–Hagen–Kibble mechanism [5–10], which has the interesting feature that it also predicts the existence of an additional particle: the Higgs boson. For decades, physicists have tried to find experimental evidence for the existence or the non-existence of this particle. On July 4th of 2012, scientists from the ATLAS and CMS experiments at the Large Hadron Collider (LHC) announced the discovery of a new particle with properties consistent with those of the standard model Higgs boson [11, 12]. Further study is required to confirm or rule out that it truly is the Higgs boson. Even if it is confirmed, the chapter on Higgs physics will by no means be closed. Very little is known about what the Higgs structure of the Universe is like. This takes us to the domain explored in the presented study.

Possible theories extending the standard model are constantly being developed. The motivation behind this is to remove the few known inconsistencies of the standard model and to extend it to provide a description of other observed phenomena. While there is only one kind of Higgs boson (which is electrically neutral) in the standard model, there are no known theoretical arguments ruling out the possibility to have a more complex Higgs structure with additional bosons. Some theories extending the standard model require the existence of additional Higgs bosons in order to be consistent. An example of this are the much-studied supersymmetry theories [13–15]. Many possible Higgs sectors, including the minimally extended one in which a second Higgs field described by a doublet is added [16, 17], contain electrically charged Higgs bosons ( $H^\pm$ ). The presented analysis constitutes an experimental search for these hypothetical particles. It aims to provide evidence for their existence or their non-existence.

If charged Higgs bosons exist, they are almost certainly very short-lived (like most known and hypothetical elementary particles) and thus have to be produced where they want to be studied. As is expressed in the famous formula  $E = mc^2$ , producing massive particles requires energy. This can be provided by accelerating particles such as electrons or protons to high energies and colliding them. The collisions are probabilistic quantum mechanical processes. This means that their analysis must be done statistically, implying the need to observe many collisions in order to reach conclusions. Very short-lived particles, such as the hypothetical  $H^\pm$  would be, decay to other particles before being detected. Their existence must be inferred from the decay products.

The theories predicting the existence of charged Higgs bosons do not predict the value of their mass, which is why the search for them must be performed over a wider mass range. The presented search is for charged Higgs bosons having a mass in the range 80–160 GeV,

i.e. lighter than the top quark (*light*  $H^\pm$ ). They can be produced in the decays of top quarks. The search is sensitive to charged Higgs bosons produced in the decays of pairs of top quarks via the decay  $t \rightarrow H^\pm b$  and decaying to a tau lepton and neutrino,  $H^\pm \rightarrow \tau\nu_\tau$ . Only all-hadronic final states are considered. They are characterized by the presence of a hadronically decaying tau lepton ( $\tau \rightarrow \nu_\tau + \text{hadrons}$ ); missing transverse energy due to the presence of neutrinos; and additional jets, of which two originate from a beauty quark (b-jets).  $H^\pm$  candidate events possessing this *detector fingerprint* are selected for the analysis, though the candidate events are only required to have at least one b-jet, because of the limited b-jet identification efficiency.

Irreducible background comes from events possessing the same fingerprint as the signal events, either because they genuinely have a similar final state (such as standard model top-antitop quark events or events with a W boson and additional jets), or because misidentification and mismeasurement occurred (mostly QCD multijet events). Background with genuine tau leptons from the decays of W bosons can be partially suppressed by exploiting the fact that the W bosons and the hypothetical  $H^\pm$  bosons have a different spin. The tau leptons produced in their decays have opposite handedness, leading to different observable properties.

Neutrinos only interact via the weak interaction and are therefore not detected in the experiment. Their presence can still be deduced by applying the principle of conservation of momentum in the plane perpendicular to the beam, the *transverse* plane. The all-hadronic final state of the hypothetical charged Higgs boson events has the advantage that all neutrinos appearing in it stem from the  $H^\pm$  boson. This allows the reconstruction of the transverse mass of the  $H^\pm$  bosons. Experimentally, the transverse mass of the tau-and-neutrino system is reconstructed using the missing transverse energy vector as the total transverse momentum vector of the neutrinos. The transverse mass is used to extract a possible signal: the presence of charged Higgs bosons would appear as a peak above the background of known physical processes in the transverse mass distribution.

The author's work presented here is the development of a way to reconstruct the *invariant* mass of the tau-and-neutrino system and to investigate the prospects of using it for signal extraction, replacing or complementing the transverse mass. Using the invariant mass has both advantages and disadvantages compared to the transverse mass. The main advantage is that its calculation uses more of the information gathered by the experiment, which is expected to increase the signal sensitivity of the analysis. In addition, provided that the invariant mass can be reconstructed well, the peak a new particle would produce in its distribution is expected to be sharper, easier to separate from the peak in the background due to the W boson, and to allow a better estimation of the mass of a possible new particle if a signal is observed. The disadvantage of the invariant mass is that its reconstruction is far less straightforward than that of the transverse mass. The reason is that the calculation of the invariant mass requires the knowledge of the total momentum vector of the tau-and-neutrino system. However, only the transverse momentum vector of the neutrinos can be reconstructed in general, leaving the longitudinal momentum component undetermined. The invariant mass reconstruction presented here is based on the idea that the longitudinal momentum of the neutrinos can be calculated by making use of the fact that they are (indirectly) decay products of a top quark and that the momenta of all the other decay products of the same quark can be measured directly. The mass of the parent top quark is then used as a kinematical constraint to allow the calculation of the longitudinal momentum. The challenges in the invariant mass reconstruction are that configurations appear, where there are two possible solutions, of which the better one must be selected, or that there are

only unphysical solutions, which need to be either ignored or the method modified to give physical solutions. Solving these challenges may introduce new systematic uncertainties that need to be taken into account and might spoil the advantage gained by including more experimental information compared to the transverse mass, whose calculation is straightforward and unambiguous.

The target quantity to be determined in the analysis is a limit on the probability (called *branching ratio*,  $\mathcal{B}$ ) of a top quark decaying to a charged Higgs boson and a beauty quark and the charged Higgs boson in turn decaying to a tau lepton and a neutrino. This can be expressed more briefly as the product of branching ratios  $\mathcal{B}(t \rightarrow H^\pm b) \times \mathcal{B}(H^\pm \rightarrow \tau^\pm \nu_\tau)$ , which we refer to as the signal branching ratio for convenience. The sensitivity of the analysis is described by the limit on the signal branching ratio that is expected under the hypothesis that the data are described by the background. Quantitative statements about the existence or non-existence of charged Higgs bosons are based on the *observed* limit compared to the expected limit. The lower this expected limit can be set, the more sensitive the analysis.

The research presented in this thesis was guided by two main research questions related to the issues discussed above.

**Research question 1** Is it possible to reconstruct the invariant mass of the tau-and-neutrino system by first calculating the neutrinos' longitudinal momentum using the top quark mass as a kinematical constraint?

**Research question 2** What signal sensitivity can be achieved using the invariant mass distribution? In other words, how low is the upper expected limit that can be set on the signal branching ratio  $\mathcal{B}(t \rightarrow H^\pm b) \times \mathcal{B}(H^\pm \rightarrow \tau^\pm \nu_\tau)$ ? How does this compare to using the transverse mass distribution?

These questions are answered in Section 11.

A data analysis was performed to obtain the expected limits using the transverse mass and the invariant mass. It used proton-proton (pp) collision data recorded by the Compact Muon Solenoid (CMS) detector of the LHC during the year 2011, corresponding to an integrated luminosity of about  $5.1 \text{ fb}^{-1}$ . The energy available for producing new particles in these collisions was  $\sqrt{s} = 7 \text{ TeV}$ . While the full data sample recorded by the CMS detector is used to perform the actual search, only the 2011 data were used here to keep the analysis simple. The performance of the invariant mass reconstruction algorithm is expected to be qualitatively similar in the rest of the data, though it may have to be optimized in a different way due to the different experimental conditions.

The expected limits were calculated in several optimization scenarios. This way the scenario leading to the best signal sensitivity could be found. As the goal was only to study, what signal sensitivity can be achieved using different methods, no observed limits are shown. There is a reason for this: the presented  $H^\pm$  search is performed in such a way that the observed limits are only considered once all steps of the analysis are fully developed and well understood. This is called *blinding* of the data and aims to prevent the researchers from unconsciously optimizing the analysis to artificially enhance something that looks like a possible signal, which may be physical in origin, a random fluctuation, or an artefact of the experiment or the analysis. Since the development of the analysis is still ongoing, no observed limits may be shown at this stage.

The performance of the invariant mass reconstruction algorithm was mostly investigated

using *simulated* events resembling the ones recorded experimentally by the CMS detector. The use of simulated events has the advantage that the full information of the event is known. In recorded data events, only what can be reconstructed experimentally is known.

## 1.1 Previous results of charged Higgs boson searches

All limits given here are at the 95% confidence level.

The lower limit on the mass of charged Higgs bosons is approximately 79 GeV, as determined by the experiments at the LEP collider [18–21]. This lower limit is the reason why the mass range studied in the presented analysis begins at 80 GeV. Previous results of the presented analysis were published in May 2012 [22]. No statistically significant amount of signal was observed. Upper limits of 1% to 4%, depending on the  $H^\pm$  mass, were set on the signal branching ratio  $\mathcal{B}(t \rightarrow H^\pm b) \times \mathcal{B}(H^\pm \rightarrow \tau^\pm \nu_\tau)$  for  $H^\pm$  masses between 80 and 160 GeV. Searches for charged Higgs bosons have also been performed by the ATLAS Collaboration. These have led to setting an upper limit between 5% and 1% on  $\mathcal{B}(t \rightarrow H^\pm b)$  for  $H^\pm$  masses between 90 and 160 GeV [23], assuming  $\mathcal{B}(H^\pm \rightarrow \tau^\pm \nu_\tau) = 1$ .

## 2 General kinematics of hadron collisions

The fact that hadrons are not elementary particles but are composed of multiple elementary particles complicates the kinematics of hadron collisions. The elementary particles making up a hadron are quarks and gluons, collectively referred to as *partons*. Each parton carries some fraction  $x \in [0, 1]$  of the hadron's momentum  $P$ . The observed momentum fractions depend on the energy at which they are probed. For instance, when scattering relatively low-energy electrons off a proton, results will indicate that most of the proton's momentum is distributed evenly between its three valence quarks (one down and two up quarks). If the collision energy is increased, the observed momentum fraction carried by other partons—gluons and virtual quarks—will increase. The distributions of momentum fraction  $x$  for each type of parton as a function of the momentum transfer squared  $Q^2$  between the parton and the probing particle are called *parton density functions*.

At high energies, proton collisions do not in fact take place between protons as a whole, but between partons inside these protons. While the four-momentum of the colliding protons as a whole,  $P$ , is known, it is not known which partons participated in the hard collision and what their momenta were. The idea is illustrated in Figure 2.1. It follows that the true collision energy  $\sqrt{s_{\text{true}}} = |p_{\text{parton } 1} + p_{\text{parton } 2}| = (x_1 + x_2)P$  is unknown. What is more problematic is that the total momentum of the initial state in the direction of the beam axis is unknown, meaning that the concept of conservation of momentum is only useful in the  $x$ - $y$  plane perpendicular to the beam, where the total momentum of the initial state is known to be  $\vec{0}$ —after all, the beam particles do not move significantly in this plane. This explains the interest in *transverse variables*, i.e. variables depending only on the projections of the momenta onto the  $x$ - $y$  plane. The ones considered in this analysis are presented in Section 2.3 to 2.5 below.

### 2.1 Coordinate system, angles, and pseudorapidity

The CMS experiment uses a right handed coordinate system with the origin at the nominal interaction point. The  $x$  axis points towards the geometrical center of the LHC ring, the  $y$  axis points upwards perpendicular to the LHC plane, and the  $z$  axis points in the direction of the counterclockwise beam. The  $x$ - $y$  plane is called the *transverse* plane and the beams are perpendicular to it. The distance from the beam axis in the transverse plane is  $\rho \equiv \sqrt{x^2 + y^2}$ . The azimuthal angle  $\phi$  is measured from the  $x$  axis in the  $x$ - $y$  plane. The polar angle  $\theta$  is measured from the  $z$  axis. The pseudorapidity  $\eta$  is uniquely specified by the polar angle through the definition

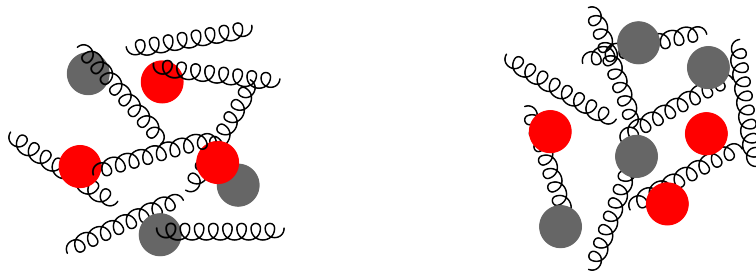
$$\eta = -\ln[\tan(\theta/2)]. \quad (2.1)$$

### 2.2 Angular distance

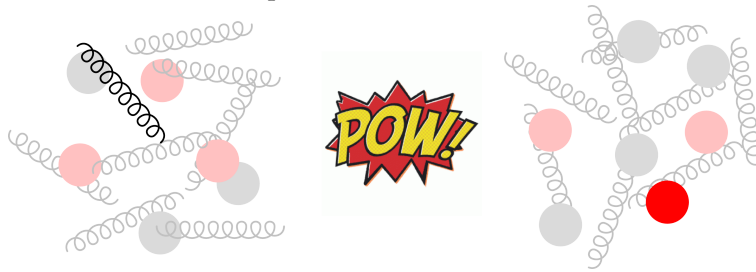
Angular distance refers to the distance between two momentum vectors or particle tracks in  $\eta$ - $\phi$  space, defined as

$$\Delta R = \sqrt{(\Delta\eta)^2 + (\Delta\phi)^2}. \quad (2.2)$$

The name is used in spite of the fact that the pseudorapidity is not an angle. It does, after all, depend monotonously on the polar angle  $\theta$  via the relation (2.1). The reason why  $\eta$  is



(a) Protons consist of partons: valence quarks (●), virtual or *sea* quarks (●), and gluons (~~~~~). Each parton carries an unknown fraction of the proton's momentum.



(b) When a collision happens, typically only two partons participate in hard scattering. It is not known, which partons participated and what their momentum fractions were. Hence, the initial state momentum is not known along the beam axis.

Figure 2.1: Very schematic illustration of what happens in a high-energy proton-proton collision.

used instead of  $\theta$  is that the distribution of particles recorded is approximately flat with respect to  $\eta$ , but not with respect to  $\theta$ . This means that after many collisions, the number of particles inside a fixed interval  $\delta\eta$  centered around any given  $\eta$  is the approximately same. The same is true for the azimuthal angle  $\phi$ .

### 2.3 Transverse momentum

The two-dimensional vector formed by the momentum components in the  $x$ - $y$  plane is referred to as the transverse momentum vector and denoted  $\vec{p}_T$ . Its absolute value is called the transverse momentum,  $p_T = |\vec{p}_T|$ .

### 2.4 Undetected particles and missing transverse energy

Of the known elementary particles, neutrinos only interact via the weak interaction. When they are produced in  $pp$  collisions, they fly off from the interaction point without being detected by the detector. Therefore, their momentum and energy cannot be measured and their presence has to be inferred from the kinematics of the collision. This is done by identifying all the detected particles belonging to the collision, taking the vector sum of their momenta, and applying the principle of conservation of momentum: the total momentum of the final state must be equal to that of the initial state. Whatever difference is observed must be due to undetected particles (neglecting experimental effects for now), so that the vector sum of all their momenta (though not their individual momenta) can be calculated.

However, as was explained above, the total momentum of the initial state along the beam axis (in the  $z$  direction) is unknown, so conservation of momentum cannot be used to calculate the momentum carried by undetected particles in that direction. The described method still works in the  $x$  and  $y$  directions, i.e. in the transverse plane. The negative vector sum of the transverse momenta of all visible particles pertaining to a collision is called the *missing transverse energy*,

$$\vec{E}_T^{\text{miss}} = - \sum_i^{\text{all visible particles}} \vec{p}_{T,i}. \quad (2.3)$$

The term is also used to refer to its norm,  $E_T^{\text{miss}} \equiv |\vec{E}_T^{\text{miss}}|$ . (The terms *momentum* and *energy* are often used interchangeably here, since for many purposes it is sufficient to treat most particles as massless, in which case  $E \approx |\mathbf{p}|$ .) The minus sign in the definition of  $\vec{E}_T^{\text{miss}}$  is included so that the total transverse momentum of all observed particles plus the  $\vec{E}_T^{\text{miss}}$  is zero.

A precise measurement of  $\vec{E}_T^{\text{miss}}$  is difficult, since it depends not only on what happens locally in some part of the detector but is a global variable of an entire collision. It cannot be calculated from a single reconstructed track and cluster of energy deposited in a calorimeter as is the case for a particle, but rather requires good reconstruction of *all* the observable particles in the event. Therefore it is essential for  $\vec{E}_T^{\text{miss}}$  reconstruction that the detector be as hermetic as possible, allowing no high- $p_T$  particles to escape undetected. At CMS, one ingredient for achieving this is having a hadronic calorimeter coverage of  $|\eta| < 5$ .

The missing transverse energy is sometimes treated like just another particle's transverse momentum. This viewpoint gives good results in some situations if care is taken, but in general,  $\vec{E}_T^{\text{miss}}$  is to be thought of more like a kinematical variable pertaining to the entire collision. Single contributions to it from neutrinos, mismeasurement, and perhaps even yet unknown particles, cannot be distinguished.

## 2.5 Mass variables

### 2.5.1 General remarks and role in new physics searches

A group of any number of particles that are distant enough from each other not to interact significantly—not, for instance, forming a bound state or scattering off each other—is referred to as a *system* in this thesis.

Quantities having the character of a *mass* can be calculated for a system, based on the reconstructed momenta of its particles, where a mass is understood to be a quantity that describes the difference between the system's total energy and momentum. As such, the mass variables are measures of the 'internal energy' of the system, as opposed to the momentum of its center of mass. They satisfy all the expected properties of a mass, justifying their name:

- They are scalars.
- They are non-negative.
- They have the correct dimension.

The reason why we are interested in the mass of a system is that unstable particles appear as peaks in the mass spectrum of their decay products. The shapes and positions of these

peaks depend on how the mass variable is constructed. By finding new peaks that are not explained by the background of known physics processes we can find new particles.

The mass variables considered in this analysis are the transverse mass and the invariant mass of the tau-and-neutrino system.

### 2.5.2 Transverse mass

As its name suggests, the *transverse mass* only takes into account transverse momenta and energies. This has the advantage of allowing to calculate a meaningful mass variable in the presence of undetected particles, such as neutrinos, by approximating their total transverse momentum with the  $\vec{E}_T^{\text{miss}}$ . The disadvantage is that any possibly available longitudinal momentum information is ignored. The transverse mass of a system of two *massless* particles is given by

$$m_T = \sqrt{2E_{T,1}E_{T,2}(1 - \cos\phi)}, \quad (2.4)$$

where  $\phi$  is the angle between the momenta of the two particles in the transverse plane. The cosine has a minimum when this angle is  $\pi$  ( $\cos(\pi) = -1$ ), i.e. when the particles move back-to-back in the transverse plane. In this limiting case, their transverse mass is maximal and equal to the invariant mass of the system,  $m_T(\phi = \pi) = m$ . The transverse mass distribution of a two-particle system has the shape of a Jacobian peak.

In this analysis, the transverse mass of the tau-and-neutrino system is calculated using the  $\vec{E}_T^{\text{miss}}$  as the total transverse momentum of the tau neutrinos,

$$m_T(\tau, \nu_\tau) = \sqrt{2E_T^{\text{miss}}E_T^{\tau, \text{jet}}(1 - \cos\phi_{\tau, \nu_\tau})}. \quad (2.5)$$

The mass of the tau lepton is neglected, which is expected to be a good approximation, since it is less than 2 GeV and thus small compared to the experimental resolution and uncertainty.

### 2.5.3 Invariant mass

The invariant mass of a system consisting of  $N$  particles is defined as the norm of its total momentum four-vector:

$$m = \left| \sum_{i=1}^N p_i \right|, \quad (2.6)$$

where  $p_i$  is the momentum four-vector of the  $i$ th particle in the system. For a system consisting of a single on-shell particle or the decay products of an on-shell particle, the invariant mass is equal to the rest mass of the particle. If the parent particle was off-shell, the invariant mass differs in general from the rest mass, following a relativistic Breit-Wigner distribution [1].

The reconstruction of the invariant mass of the tau-and-neutrino system is the main object of investigation in this thesis and is presented in detail in Section 9.

### 3 Theory behind charged Higgs bosons and search channel

I'd take the awe of understanding over  
the awe of ignorance any day.

---

Douglas Adams

The standard model (SM) of particle physics [2–4] is a theory that describes the electromagnetic, weak, and strong interactions of elementary particles. These are the quarks and leptons, which are fermions; the gauge bosons; and the SM Higgs boson. Formally, the SM is a quantum field theory, in which interactions are introduced by requiring the Lagrangian density to be invariant under local phase transformations of the fields, so-called *gauge transformations*. These gauge invariances are mathematically described by symmetry groups. The electromagnetic and weak interaction are unified into the electroweak (EWK) theory, while the strong interaction is described by quantum chromodynamics (QCD). A peculiar feature of the SM is the origin of the particle masses. These cannot be put into the theory ‘by hand’, as this would break the theory’s gauge invariance, but have to be generated by some mechanism. In the SM, this is the breaking of electroweak symmetry by the *Higgs–Brout–Englert–Guralnik–Hagen–Kibble mechanism*, which has the added feature of predicting the existence of a massive spinless boson, called the Higgs boson.

The predictions of the SM have been compared with experimental observations from a wide range of experiments and found to be in astonishingly good agreement. However, until very recently there was no experimental evidence for one ingredient of the SM: the Higgs boson. This last missing piece has now probably been discovered, as a new boson with properties consistent with those of the SM Higgs boson has been observed at the LHC [11, 12].

Nevertheless, the SM continues to have some shortcomings, which have motivated the development of theories that go beyond it. In the SM, neutrinos are required to be massless, which contradicts the experimentally observed neutrino oscillations, i.e. the changing of a neutrino’s flavour with time. The SM does not explain the observed matter/antimatter asymmetry in the Universe, nor does it provide a candidate for the observed dark matter. It also contains no explicit reference to gravity or dark energy, though it does raise the question of what the vacuum energy is (an unsolved problem, since it is not known how to renormalize it), which could be related to both. But perhaps the most serious problem of the SM is the so-called *hierarchy problem*, since it challenges the consistency of the theory itself.

In quantum field theory, masses of particles receive quantum corrections. When these are calculated perturbatively, corresponding to Feynman diagrams with loops, they depend on some energy scale and in many cases diverge as this energy scale becomes very large. In the case of fermions and gauge bosons, the correction terms are proportional to the bare mass of the particle and to the logarithm of the energy scale. New phenomena not described by the SM, which is a low-energy theory, are thought to become important at higher energy scales, which could remove the divergences. Because the divergence is logarithmic for spin-1/2 and spin-1 particles, the mass corrections diverge very slowly and do not become extremely large even at scales, at which new physics is expected to become important. The problem is that this is not true for the SM Higgs boson. Owing to the fact that it is spinless, it receives qualitatively different correction terms: they are not proportional to its bare mass—in fact they are independent of it—and depend on the square and higher powers of

the energy scale. Therefore, they diverge very quickly and are already huge at scales much lower than those at which new physics is expected. Since the corrections are independent of the Higgs boson's bare mass, requiring it to be zero does not change the situation at all: the corrected mass still becomes huge. On the other hand, it is experimentally known to be only of the order of the W boson mass, i.e.  $\mathcal{O}(100 \text{ GeV})$ . This is called the hierarchy problem, where ‘hierarchy’ refers to the difference of many orders of magnitude between the W mass and the scale at which the SM is not expected to hold anymore. One possible solution is to fine-tune the parameters of the theory, but since the new physics scale is thought to be at around at least  $10^{15} \text{ GeV}$ ,  $10^{13}$  orders of magnitude larger than the Higgs boson mass, fine-tuning has to cause correction terms to cancel to an incredible precision of one part in  $10^{26}$ . As a more ‘natural’ alternative to fine-tuning, the hierarchy problem could be solved by extending the SM in some way. One much studied extension is supersymmetry (SUSY) [13–15]. In SUSY theories, a new symmetry relating bosons and fermions is proposed. This leads to a prediction of the existence of additional particles. They give rise to new Higgs boson mass correction terms that could cancel others, removing the quadratic divergence. Another proposed extension is technicolor [24–26], in which the Higgs boson is a composite particle made of fermions, thus removing the hierarchy problem altogether by not having fundamental spinless particles at all.

SUSY theories are of additional relevance to the present subject: the minimal supersymmetric standard model (MSSM) has an extended Higgs sector containing five bosons, of which two are electrically charged. The Higgs sector of the MSSM will be presented in Section 3.2.2.

### 3.1 Higgs–Brout–Englert–Guralnik–Hagen–Kibble mechanism and mass generation in the standard model

The electroweak part of the SM is governed by the gauge symmetry group  $SU(2)_L \times U(1)_Y$ . The generators of the two constituent groups are the weak isospin times the Pauli spin matrices,  $\vec{I} \cdot \vec{\tau}$  (with third component  $I_3\tau_3$ ), and the weak hypercharge  $Y$ , respectively. These are related to the electric charge by the equality

$$Q = I_3 + \frac{Y}{2}. \quad (3.1)$$

The weak isospin gauge fields of the  $SU(2)_L$  group couple only to left-handed fermions, hence the subscript  $L$ .

Including arbitrary mass terms for the gauge bosons (described by fields  $A_\mu$ ) in the SM Lagrangian density is not possible, as they would cause the Lagrangian to loose its gauge invariance ( $M^2 A_\mu A^\mu$  is not invariant if  $A_\mu \rightarrow A_\mu - \partial_\mu \chi(x)$ , so  $M^2$  must be zero). On the other hand, it is known experimentally that the  $W^\pm$  and Z bosons have masses, so they must be generated somehow. Arguably the simplest known way of achieving this is the Higgs–Brout–Englert–Guralnik–Hagen–Kibble mechanism [5–10].

The idea is the following. One adds to the Lagrangian of the field theory a new complex scalar field  $\phi = \phi(x)$  with the usual free propagation term for such a field,

$$(D_\mu \phi)^\dagger (D^\mu \phi), \quad (3.2)$$

where

$$D_\mu = \partial_\mu - \frac{ig}{2} \tau_a W_\mu^a - \frac{ig'}{2} Y B_\mu \quad (3.3)$$

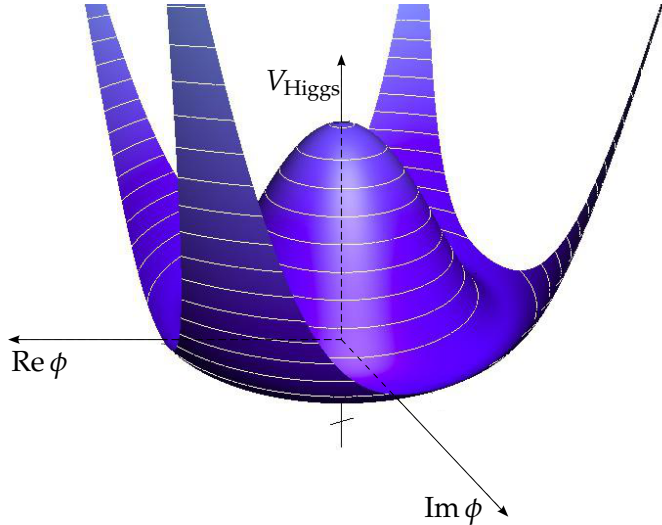


Figure 3.1: Shape of the Higgs potential.

is the covariant derivative containing the electroweak coupling constants ( $g, g'$ ), the  $SU(2)_L$  generator  $\tau_a$  and gauge field  $W_\mu^a$ , and the  $U(1)$  generator  $Y$  and gauge field  $B_\mu$ . One also adds a potential involving  $\phi$ , of the form

$$V_{\text{Higgs}}(\phi) = \mu^2 \phi^\dagger \phi + \lambda (\phi^\dagger \phi)^2, \quad (3.4)$$

where  $\mu$  is a complex and  $\lambda$  a real constant parameter, chosen such that  $\mu^2 < 0$  and  $\lambda > 0$ , so that the potential is bounded from below. With these choices, the Higgs potential qualitatively has the shape shown in Fig. 3.1.

The contribution of the Higgs field to the Lagrangian of the theory is

$$\mathcal{L}_{\text{Higgs}} = (D_\mu \phi)^\dagger (D^\mu \phi) - \mu^2 \phi^\dagger \phi - \lambda (\phi^\dagger \phi)^2. \quad (3.5)$$

The field  $\phi$  is taken to be an  $SU(2)$  doublet and denoted

$$\phi = \begin{pmatrix} \phi^+ \\ \phi^0 \end{pmatrix} = \frac{1}{\sqrt{2}} \begin{pmatrix} \phi_1 + i\phi_2 \\ \phi_3 + i\phi_4 \end{pmatrix}. \quad (3.6)$$

As can be seen from Eq. (3.4), the Higgs potential only depends on the product  $\phi^\dagger \phi$ , which is an  $SU(2)$  scalar. The minima of the potential can be found by setting the partial derivative with respect to  $\phi^\dagger \phi$  equal to zero. The way the signs of  $\mu^2$  and  $\lambda$  were chosen, the Higgs potential has minima at

$$\phi^\dagger \phi = \frac{1}{2} (\phi_1^2 + \phi_2^2 + \phi_3^2 + \phi_4^2) = -\frac{\mu^2}{2\lambda} \equiv \frac{v}{2}. \quad (3.7)$$

The minimum of the potential is by definition the *vacuum*, the configuration with the lowest energy. The crucial point is that the minimum of the potential is *not* at the origin (i.e. at  $\phi^\dagger \phi = 0$ ) and that the potential is independent of the *phase* of the complex field  $\phi$ . The parameters  $\mu^2$  and  $\lambda$  were chosen to that effect. This means that there are *infinitely many* values of  $\phi$ —one for each phase—that minimize the potential, lying on a circle of radius  $v$

(see Fig. 3.1). It follows that the Higgs field has a nonzero vacuum expectation value  $v$  and that any set of  $\phi_i$  ( $i = 1, 2, 3, 4$ ) can be chosen, but once chosen, both the  $SU(2)_L$  and  $U(1)_Y$  symmetries are spontaneously broken. A conventional choice is  $\phi_1 = \phi_2 = \phi_4 = 0$  and  $\phi_3 = v$ , so that

$$\phi_0 = \frac{1}{\sqrt{2}} \begin{pmatrix} 0 \\ v \end{pmatrix} \quad (3.8)$$

is the vacuum expectation value of the doublet. We expand  $\phi$  around the vacuum value to find the particle spectrum of the theory:

$$\phi(x) = \frac{1}{\sqrt{2}} \begin{pmatrix} 0 \\ v + h(x) \end{pmatrix} \quad (3.9)$$

and consequently  $\phi^\dagger \phi = (v + h)^2 / 2$ . Inserting this into the Lagrangian (3.5) yields

$$\begin{aligned} \mathcal{L}_{\text{Higgs}} = & \frac{1}{2} (\partial_\mu h)(\partial^\mu h) + \mu^2 h^2 + \frac{g^2 v^2}{8} ((W_1)_\mu (W_1)^\mu + (W_2)_\mu (W_2)^\mu) \\ & + \frac{v^2}{8} (g' B_\mu - g (W_3)_\mu) (g' B^\mu - g (W_3)^\mu) + \text{interaction terms} \end{aligned} \quad (3.10)$$

The interaction terms are of no interest in the present discussion. The terms containing squares of the gauge fields,  $A_\mu A^\mu$ , have the form of mass terms. Note, however, that the weak isospin and hypercharge gauge fields  $W_3$  and  $B$  mix in the last mass term of the Lagrangian (3.10). They do therefore not describe physical particles, which are mass eigenstates. The electrically neutral physical fields corresponding to the photon ( $A_\mu$ ) and the Z boson ( $Z_\mu$ ) are given by

$$\begin{pmatrix} A_\mu \\ Z_\mu \end{pmatrix} = \begin{pmatrix} \cos \theta_W & \sin \theta_W \\ -\sin \theta_W & \cos \theta_W \end{pmatrix} \begin{pmatrix} B_\mu \\ (W_3)_\mu \end{pmatrix}, \quad (3.11)$$

where  $\theta_W$  is the weak mixing angle defined by

$$g \sin \theta_W = g' \cos \theta_W \equiv e, \quad (3.12)$$

( $e$  is the elementary charge), while the physical charged boson fields are

$$W_\mu^\pm = \frac{1}{\sqrt{2}} [(W_1)_\mu \mp i(W_2)_\mu]. \quad (3.13)$$

Using these expressions, the Lagrangian becomes

$$\begin{aligned} \mathcal{L}_{\text{Higgs}} = & \frac{1}{2} (\partial_\mu h)(\partial^\mu h) + \mu^2 h^2 + \left(\frac{gv}{2}\right)^2 (W^+)_\mu (W^-)^\mu \\ & + \frac{1}{2} \left(\frac{gv}{2 \cos \theta_W}\right)^2 Z_\mu Z^\mu + 0 \times A_\mu A^\mu + \text{interaction terms} \end{aligned} \quad (3.14)$$

from which it can be seen that the  $W^\pm$  bosons have acquired the mass  $M_{W^\pm} = gv/2$  and the Z boson the mass  $M_Z = gv/(2 \cos \theta_W)$ , whereas the photon remains massless. The last fact can be understood by considering the generators of the gauge group. The  $SU(2)_L \times U(1)_Y$  gauge symmetry is broken, but since the vacuum remains invariant under a *combined*  $SU(2)$   $I_3$  rotation by an angle  $\theta$  and  $U(1)$  rotation by the angle  $\theta/2$ , the subgroup of gauge transformations with the generator  $I_3 + Y/2$  corresponding to such a combined transformation

remains unbroken. Comparing to Eq. (3.1), it is seen that this generator is none other than the electric charge  $Q$ , meaning that the unbroken gauge subgroup is that of the electromagnetic interaction,  $U(1)_Q$ . As a consequence, the photon remains massless while the weak interaction bosons acquire mass.

The Higgs field, being described by a complex doublet, has  $2 \times 2 = 4$  degrees of freedom. After the spontaneous symmetry breaking, 3 of these are ‘absorbed’ by the gauge boson fields as the  $W^\pm$  and  $Z$  bosons acquire mass. A massive particle with spin has a longitudinal polarization degree of freedom, while a massless particle does not. Therefore, the massive weak bosons have three degrees of freedom each, while the massless photon only has two. In the process,  $4 - 3 = 1$  degree of freedom remains. This corresponds to a new physical, scalar particle: the standard model Higgs boson.

Since the masses of the weak bosons have been measured experimentally, the vacuum expectation value of the Higgs potential is known to be  $v \approx 246$  GeV [1]. The Higgs boson has mass  $M_h = -2\mu^2 > 0$ , but this is a free parameter of the theory whose value has to be determined experimentally.

The Higgs mechanism also provides an explanation for the masses of the fermions. If Yukawa interactions between the fermion and Higgs fields are included, these give rise to mass terms for the fermions when the electroweak symmetry is spontaneously broken. However, the fermion masses again remain free parameters of the theory and are not predicted.

### 3.2 Beyond the minimal model: extended Higgs sectors and charged Higgs bosons

Even as data collected by the ATLAS and CMS experiments suggest that a Higgs boson with properties compatible with that of the SM exists, little is known about the Higgs sector. It is therefore certainly worthwhile to consider models beyond the minimal one. There are few known constraints on the structure of such extended Higgs sectors. First, it is known experimentally that the  $\rho$  parameter, defined as

$$\rho = \frac{M_W^2}{M_Z^2 \cos^2 \theta_W}, \quad (3.15)$$

is very close to 1. The  $\rho$  parameter is determined by the Higgs structure of the theory and is automatically equal to 1 at tree level [27, 28] if the theory only contains Higgs doublets and singlets, as is the case in the SM (one doublet). Loop corrections may cause deviations from this value. Second, there are severe limits on the existence of flavor-changing neutral currents (FCNCs). In the minimal Higgs model, these are automatically absent, but this is not generally true in non-minimal models. However, a theorem of Glashow and Weinberg [29] states that in the case of multiple Higgs doublets, tree-level FCNCs will be absent if all fermions of a given electric charge couple to no more than one Higgs doublet.

Even with these constraints, there are still infinitely many different models that are possible. Extended Higgs sectors could include any number of Higgs multiplets, as long as the couplings are such that the above constraints are satisfied. We will discuss one important case of an extended Higgs sector, in which a second complex Higgs doublet is added to the theory. Such a model is particularly attractive because:

1. It is a minimal extension in that it adds the smallest number of new arbitrary parameters.
2. It predicts new physical phenomena, which should be directly observable by experiment. In particular, it predicts the existence of charged Higgs bosons.
3. It satisfies the constraints  $\rho \approx 1$  and, if the Higgs-fermion couplings are chosen appropriately, the absence of FCNCs (by virtue of the Glashow–Weinberg theorem).

In addition, the minimal supersymmetric standard model requires such a Higgs structure.

### 3.2.1 Two-Higgs-doublet model

In a two-Higgs-doublet model, there are two complex  $SU(2)_L$  doublet scalar fields,  $\phi_1$  and  $\phi_2$ . As in the one-doublet case of the SM, a Higgs potential is added to the Lagrangian, which spontaneously breaks the  $SU(2)_L \times U(1)_Y$  symmetry down to  $U(1)_Q$ . The potential is [17]

$$\begin{aligned} V_{\text{Higgs}}(\phi_1, \phi_2) = & \lambda_1 (\phi_1^\dagger \phi_1 - v_1^2)^2 + \lambda_2 (\phi_2^\dagger \phi_2 - v_2^2)^2 \\ & + \lambda_3 \left[ (\phi_1^\dagger \phi_1 - v_1^2) + (\phi_2^\dagger \phi_2 - v_2^2) \right]^2 \\ & + \lambda_4 \left[ (\phi_1^\dagger \phi_1)(\phi_2^\dagger \phi_2) - (\phi_1^\dagger \phi_2)(\phi_2^\dagger \phi_1) \right] \\ & + \lambda_5 \left[ \text{Re}(\phi_1^\dagger \phi_2) - v_1 v_2 \cos \xi \right]^2 \\ & + \lambda_6 \left[ \text{Im}(\phi_1^\dagger \phi_2) - v_1 v_2 \sin \xi \right]^2, \end{aligned} \quad (3.16)$$

where the  $\lambda_i \geq 0$  are real parameters (as required by hermiticity of the Lagrangian). This is the most general potential that is subject to gauge invariance and a discrete symmetry,  $\phi_1 \rightarrow -\phi_1$ , which is only violated softly by dimension-two terms. The latter constraint ensures that FCNCs are not too large [16]. The symmetry-breaking choice of ground state is

$$\phi_1 = \frac{1}{\sqrt{2}} \begin{pmatrix} 0 \\ v_1 \end{pmatrix}, \quad \phi_2 = \frac{1}{\sqrt{2}} \begin{pmatrix} 0 \\ v_2 e^{i\xi} \end{pmatrix}. \quad (3.17)$$

If  $\sin \xi \neq 0$ , there is CP violation in the Higgs sector. Note that if  $\lambda_5 = \lambda_6$ , the last two terms in Eq. (3.16) can be combined into a term proportional to  $|\phi_1^\dagger \phi_2 - v_1 v_2 e^{i\xi}|^2$  and the phase  $\xi$  can be absorbed into the fields by redefinition. We will set  $\xi = 0$  for the rest of the discussion, in which case Eq. (3.16) is the most general CP-invariant potential satisfying the constraints given above. An important parameter of the model is the ratio of the vacuum expectation values of the two scalar fields,

$$\tan \beta \equiv \frac{v_2}{v_1}. \quad (3.18)$$

The  $\tan \beta$  parameter determines much of the phenomenology of the model.

As the two complex Higgs doublets have a total of 8 degrees of freedom, of which 3 are absorbed into the weak bosons as they become massive, there are 5 remaining degrees of freedom that manifest themselves as Higgs bosons. The field combinations describing the physical Higgs bosons (i.e. mass eigenstates) are as follows. There are two charged Higgs bosons ( $H^\pm$ ), described by the fields

$$H^\pm = -\phi_1^\pm \cos \beta + \phi_2^\pm \sin \beta. \quad (3.19)$$

The square of their mass is  $M_{H^\pm}^2 = \lambda_4(v_1^2 + v_2^2)$ , so  $H^+$  and  $H^-$  have the same mass. Then there is a neutral CP-odd Higgs boson ( $A^0$ ), corresponding to the field

$$A^0 = \sqrt{2}(-\text{Im}\phi_1^0 \sin \beta + \text{Im}\phi_2^0 \cos \beta), \quad (3.20)$$

with mass squared  $M_{A^0}^2 = \lambda_6(v_1^2 + v_2^2)$ . The CP-oddness is due to the fact that  $A^0$  depends on the imaginary parts of  $\phi_{1,2}$ . Finally, there are two neutral CP-even bosons,  $H^0$  and  $h^0$ , whose description is a bit more tricky since they mix through the mass-squared matrix

$$\mathcal{M} = \begin{pmatrix} 4(\lambda_1 + \lambda_3)v_1^2 + \lambda_5v_2^2 & (4\lambda_3 + \lambda_5)v_1v_2 \\ (4\lambda_3 + \lambda_5)v_1v_2 & 4(\lambda_1 + \lambda_3)v_2^2 + \lambda_5v_1^2 \end{pmatrix}. \quad (3.21)$$

The mass eigenstates are

$$H^0 = \sqrt{2}[(\text{Re}\phi_1^0 - v_1) \cos \alpha + (\text{Re}\phi_2^0 - v_2) \sin \alpha], \quad (3.22)$$

$$h^0 = \sqrt{2}[-(\text{Re}\phi_1^0 - v_1) \sin \alpha + (\text{Re}\phi_2^0 - v_2) \cos \alpha], \quad (3.23)$$

where  $\alpha$  is a mixing angle. It can be obtained from

$$\sin 2\alpha = \frac{2\mathcal{M}_{12}}{\sqrt{(\mathcal{M}_{11} - \mathcal{M}_{22})^2 + 4\mathcal{M}_{12}^2}}, \quad (3.24)$$

$$\cos 2\alpha = \frac{\mathcal{M}_{11} - \mathcal{M}_{22}}{\sqrt{(\mathcal{M}_{11} - \mathcal{M}_{22})^2 + 4\mathcal{M}_{12}^2}}. \quad (3.25)$$

The corresponding squared masses of  $H^0$  and  $h^0$  are

$$M_{H^0, h^0}^2 = \frac{1}{2} \left[ \mathcal{M}_{11} + \mathcal{M}_{22} \pm \sqrt{(\mathcal{M}_{11} - \mathcal{M}_{22})^2 + 4\mathcal{M}_{12}^2} \right], \quad (3.26)$$

from which it can be seen that  $H^0$  more massive as  $h^0$  (unless their masses are equal).

The two-doublet model has six free parameters, whereas the minimal model had one ( $M_h$ ). These can be chosen to be the four different Higgs boson masses,  $\tan \beta$ , and the neutral Higgs mixing angle  $\alpha$ . The mass of the W boson is given by  $M_W^2 = g^2(v_1^2 + v_2^2)^2/2$ , so the quantity  $v_1^2 + v_2^2$  is fixed.

### 3.2.2 Higgs sector of the MSSM

The minimal supersymmetric standard model (MSSM) [30–36] is the minimal low-energy globally supersymmetric extension of the SM. Its gauge group and particle content are the same as those of the SM, with the addition of a superpartner for each SM particle, differing in spin by 1/2. In addition, it contains two complex Higgs doublets to break the electroweak symmetry,

$$\phi_1 = \begin{pmatrix} \phi_1^0 \\ \phi_1^+ \end{pmatrix}, \quad \phi_2 = \begin{pmatrix} \phi_2^- \\ \phi_2^0 \end{pmatrix}, \quad (3.27)$$

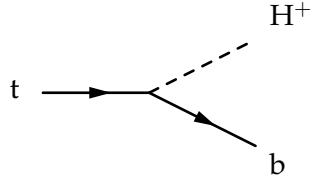
with hypercharge  $-1$  and  $+1$ , respectively. Two doublets with opposite hypercharges are required to generate the masses of all particles in the MSSM. The reason is that the superpotential of the theory only involves the fields, not their conjugate fields. As a consequence,

one doublet can only give mass to particles of a given isospin. (In the case of the SM, one scalar field and its conjugate field are used to generate the masses of the fermions of opposite isospin.) Another reason for the necessity of the two doublets is the fact that chiral anomalies originating from triangular fermion loops involving axial-vector current couplings would not cancel in the MSSM if there was only one Higgs doublet. This non-cancellation would make the theory unrenormalizable. As was described in Section 3.2.1, the two-Higgs doublet-structure gives rise to charged Higgs bosons. These are thus an essential part of the MSSM.

### 3.3 Studied $H^\pm$ search channel

#### 3.3.1 $H^\pm$ production in top quark decays in $t\bar{t}$ events

The search presented here is for light charged Higgs bosons, whose mass is  $m_{H^\pm} < m_t - m_b$ , so that they can be produced in the decays of top quarks in association with a beauty quark:



Since the mass of the beauty quark is much smaller ( $\sim 2\%$ ) than that of the top quark, charged Higgs bosons are usually referred to as light if  $m_{H^\pm} < m_t$  for simplicity.

The top quarks themselves are mostly produced as top-antitop ( $t\bar{t}$ ) pairs in the proton-proton collisions. At LHC energies, the dominant production is via gluon fusion, with a smaller contribution from quark-antiquark annihilation. Relevant Feynman diagrams are shown in Fig. 3.2. The total  $t\bar{t}$  production cross section at the CMS experiment was recently measured to be around 150 pb at  $\sqrt{s} = 7$  TeV [37–39]. Single top quarks are also produced, but because of the event selection criteria applied in the presented search, it is only sensitive to the decays of  $t\bar{t}$  pairs and the decays of single top quarks produced in association with a W boson. The production cross section of the latter has recently been measured by the CMS experiment to be approximately 15 pb at  $\sqrt{s} = 7$  TeV [40], or about 10% of the  $t\bar{t}$  production cross section. Using simulated signal samples, it was found that the contribution from single top + W events is even smaller due to a lower fraction of events passing the event selection compared to  $t\bar{t}$  events.

In the SM, top quarks almost exclusively decay to a W boson and a beauty quark, so  $\mathcal{B}(t \rightarrow Wb) \approx 1$  [1]. Since the top quarks whose decays are studied are produced in pairs, there are two top quarks in most events of interest that could each decay producing either a W or a  $H^\pm$ . (Other possible decays have a small branching ratio and are neglected.) Therefore there could be signal events with two  $H^\pm$  or with one  $H^\pm$  and one W. We refer to these signal channels as HH and HW, respectively. As the branching ratio  $\mathcal{B}(t \rightarrow H^\pm b)$  is known to be at most of the order of a few percent from previous search results (Section 1.1), the rate of HH events is expected to be at most a few percent of the HW rate.

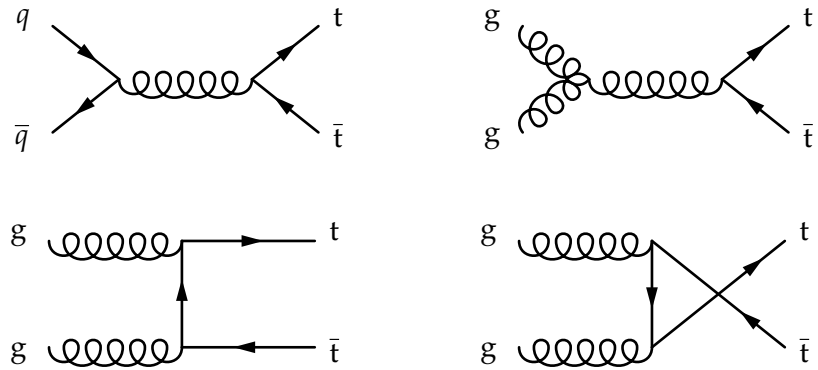
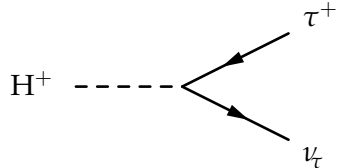


Figure 3.2: The simplest possible Feynman diagrams for  $t\bar{t}$  production via quark-antiquark annihilation in the  $s$ -channel and gluon fusion in the  $s$ -,  $t$ -, and  $u$ -channels (in the order: left to right, top to bottom).

### 3.3.2 $H^\pm$ decays to a tau lepton and neutrino

Since the coupling strength of Higgs bosons to fermions is proportional to the fermion mass, light charged Higgs bosons are expected to preferably decay to a tau lepton and a tau neutrino:



The reason is that this is the most massive pair that can be produced (while respecting conservation of electric charge and lepton number) without mixing quark flavours. Mixing of quark flavours is weak, which is why the branching ratio of light  $H^\pm$  bosons decaying to quark pairs is very small.

Examples of lowest-order Feynman diagrams for the HH and HW signal processes at parton level are shown in Figures 3.3 and 3.4.

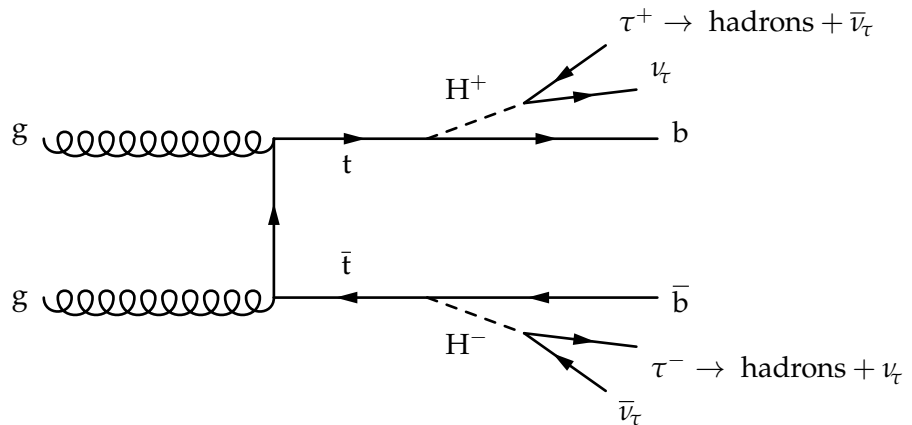


Figure 3.3: Example diagram for the the HH channel with an all-hadronic final state.

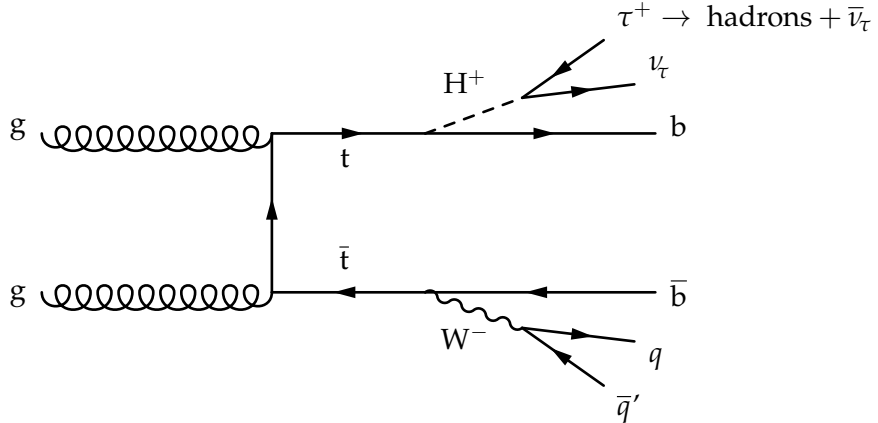


Figure 3.4: Example diagram for the the HW channel with an all-hadronic final state.

### 3.3.3 Tau lepton decays

The presented analysis only considers events with an all-hadronic final state, meaning that it contains no charged leptons. This means that the search is only sensitive to events in which the tau leptons decay to hadrons and the W bosons decay to quark-antiquark pairs. About two thirds of both tau leptons and W bosons decay hadronically. The main decay modes of tau leptons can be found in Table 3.1. The most common hadronic decay modes produce charged pions or kaons, which are sufficiently long-lived to reach the outer subdetectors of the CMS experiment and thus be treated as stable particles. Hadronically decaying tau leptons are also referred to as a  $\tau$ -jets because of their resemblance to hadronic jets. A  $\tau$ -jet is classified according to the number of charged-particle tracks associated with it in the detector. This is also called the number of *prongs*, and the jets are classified as 1-prong, 3-prong, etc. accordingly. If all tracks are reconstructed properly and only all the correct ones identified as belonging to the  $\tau$ -jet, the number of prongs is equal to the number of charged hadrons produced in the hadronic tau decay.

Despite its name, the all-hadronic final state contains at least two neutral leptons: the tau neutrino produced in association with the charged tau lepton and the tau neutrino produced in the decay of the charged tau lepton. This final state still has the experimental advantage compared to (semi-)leptonic states that it contains only two neutrinos. In signal events, these would both be decay products of the  $H^\pm$ . Assuming that the total transverse momentum of the neutrino pair can be approximated by the  $E_T^{\text{miss}}$ , this means that the transverse mass of the tau-and-neutrino system can be reconstructed. In addition, the reconstruction of the invariant mass of the system is only reliably possible because there are no other neutrinos.

### 3.3.4 Detector fingerprint of the investigated channel

The all-hadronic final state is characterized by a  $\tau$  jet; four quark jets, of which two originate from b quarks; and missing energy due to the tau neutrino pair. The identification of this fingerprint forms the theoretical foundation of the selection of signal candidate events for the analysis, which will be described in Section 7. As the efficiency of reconstructing the number of jets and of identifying a jet as originating from a beauty quark (*b-tagging*) is limited, only three reconstructed jets in total and one b-tagged jet are required. An example



$\tau$ decay channel	Branching fraction (%)	Total fraction (%)
leptonic modes		35.7
$\tau^- \rightarrow e^- \bar{\nu}_e \nu_\tau$	17.9	
$\tau^- \rightarrow \pm \mu^- \bar{\nu}_\mu \nu_\tau$	17.4	
hadronic modes		
1-prong (excl. $K^0$ )		48.1
$\tau^- \rightarrow h^- \nu_\tau$	11.6	
$\tau^- \rightarrow \rho^- \nu_\tau \rightarrow h^- \pi^0 \nu_\tau$	25.9	
$\tau^- \rightarrow a_1^- \nu_\tau \rightarrow h^- \pi^0 \pi^0 \nu_\tau$	9.4	
$\tau^- \rightarrow h^- \nu_\tau + \geq 3\pi^0$	1.3	
3-prong (excl. $K^0$ )		14.6
$\tau^- \rightarrow a_1^- \nu_\tau \rightarrow h^- h^- h^+ \nu_\tau$	9.5	
$\tau^- \rightarrow h^- h^- h^+ \nu_\tau + \geq 1\pi^0$	5.1	
5-prong (excl. $K^0$ )		0.1
$\tau^- \rightarrow 3h^- 2h^+ \nu_\tau + \geq 0\pi^0$	0.1	
hadronic modes with $K^0$		2.0
$\tau^- \rightarrow K_S^0 + X^-$	0.9	
$\tau^- \rightarrow K_L^0 + X^-$	1.1	

Table 3.1: Table of the most important tau lepton decay modes. The uncertainty of the branching ratios is 0.1 percent point or smaller. The symbol  $h$  stands for a charged pion or a charged kaon. All data are taken from Ref. [1]. Table adapted from Ref. [41].

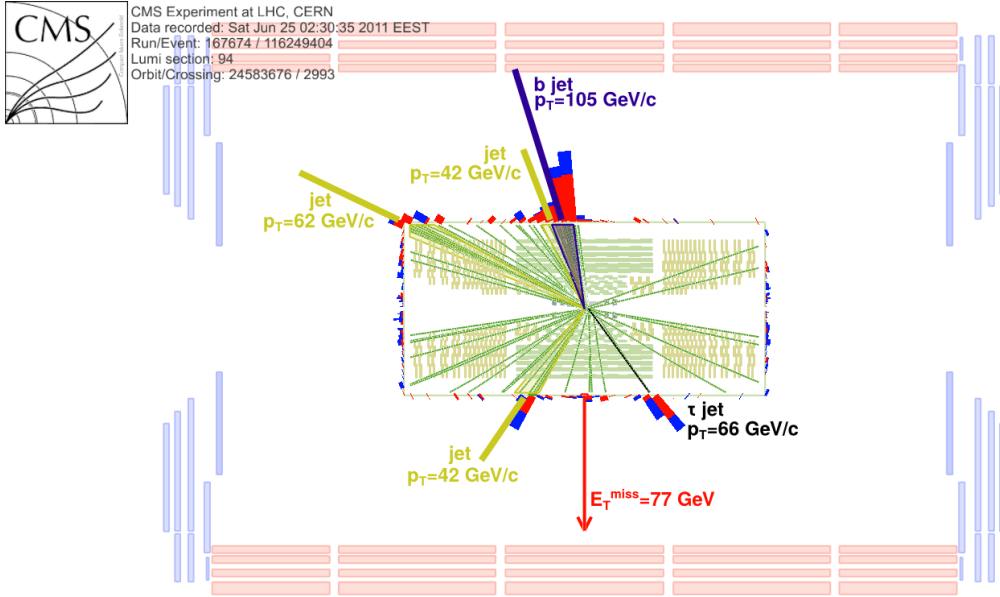
of a recorded signal candidate event compatible with the described fingerprint is shown in Figure 3.5.

### 3.3.5 Background processes

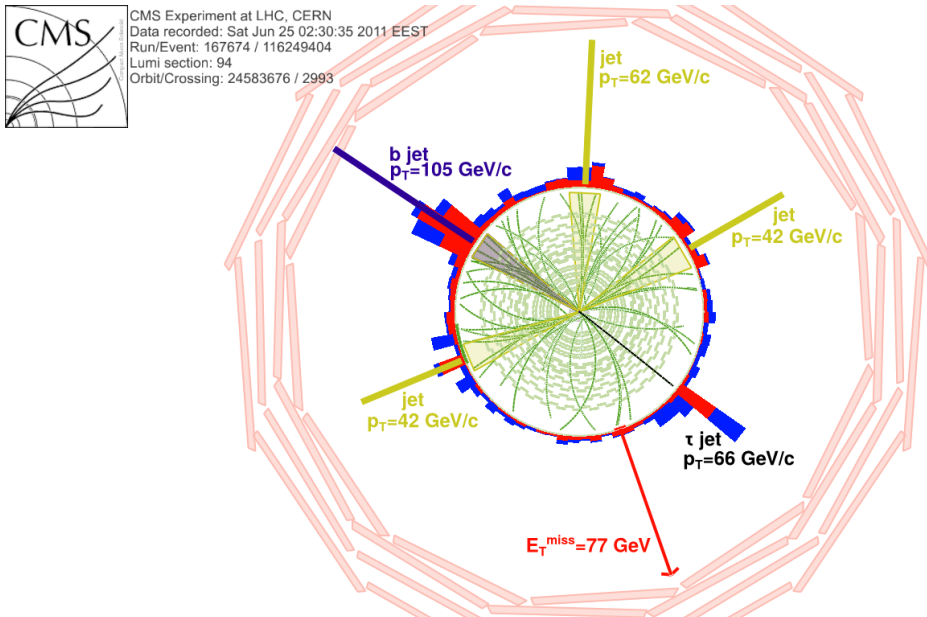
The background contributions of the all-hadronic final state search can be divided into two classes: those with a genuine tau lepton and those without one.

Of the main backgrounds, the following may contain a genuine tau lepton: SM top-antitop events ( $t\bar{t}$ ), in which both top quarks decay to a  $W$  boson; events with a single  $W$  boson and additional jets ( $W+jets$ ); diboson events with two weak bosons ( $WW, WZ, ZZ$ ); events with a Drell-Yan process ( $Z/\gamma^*+jets$ ); and events in which a single top quark is produced (single top). These background contributions are collectively called the *electroweak (EWK) background*, since they all contain EWK processes. This is the reason why they can contain genuine tau leptons. However, it is also possible that they pass the event selection because of misidentification of a hadronic jet, an electron, or a muon as a  $\tau_h$ .

In addition the above, there is a background contribution from events with multiple jets produced only via the strong interaction, called *QCD multijet* events. These rarely contain a genuine tau and, due to the absence of neutrinos in most cases, they often do not contain  $E_T^{\text{miss}}$  either. They may still pass the event selection because of misidentification and mis-measurement, leading to a ‘fake’ tau and  $E_T^{\text{miss}}$ . The probability of this happening is small,



(a) Projection onto the  $p_z$  plane.



(b) Projection onto the  $x-y$  (transverse) plane.

Figure 3.5: A recorded signal candidate event. Charged particle tracks are shown as green lines. The amounts of energy deposited in the electromagnetic and hadronic calorimeters are represented by red and blue bars, respectively. The transverse mass of the  $\tau$ -jet and  $E_T^{\text{miss}}$  is  $m_T(\tau\text{-jet}, E_T^{\text{miss}}) \approx 40 GeV. The invariant mass of the two jets in the upper half-plane is  $m_{jj} \approx 81$  GeV and the invariant mass of these and the b-jet is  $m_{jjb} \approx 196$  GeV, both compatible with a  $t \rightarrow Wb \rightarrow q\bar{q}b$  decay. Images produced by Alexandros Attikis and Matti Kortelainen. Taken from Ref. [42].$

but since there are so many QCD events, there is still a considerable number of events in which it occurs.

The contribution of all other processes to the background is sufficiently small to be neglected.

### 3.4 Separating signal from background

Much of the irreducible background to the transverse and invariant mass distributions comes from decaying W bosons, which can decay to a tau lepton and neutrino, just like the hypothetical  $H^\pm$  bosons. However, due to the different properties of the two bosons, the two kinds of events have different properties that can be exploited to suppress the background or to separate signal from background. They are explained below.

#### 3.4.1 Boson mass

The possibly different mass of the  $H^\pm$  and W bosons leads to different shapes of the mass distributions of their decay products. Charged Higgs bosons heavier than the W bosons would produce a mass peak that is shifted towards higher masses with respect to the W background peak.

#### 3.4.2 Relative coupling strengths to leptons

The probability of a W boson to decay to  $\tau\nu$  is about 11%, and approximately equal to its probability to decay to a muon or an electron (and a neutrino).<sup>1</sup> On the other hand, it is expected that a charged Higgs boson would much more probably decay to a  $\tau$  than to a muon or an electron, since the corresponding coupling strength grows with the mass of the fermion and  $M_\tau \gg M_\mu \gg M_e$ . Therefore an excess of events with tau leptons over other leptons could be an indication of the existence of  $H^\pm$ .

#### 3.4.3 Helicity correlations

The W boson has spin 1, the  $H^\pm$  spin 0. In combination with the fact that neutrinos (antineutrinos) are always left-handed (right-handed), this means that the tau leptons coming from the decays of the two different bosons have opposite helicities. This in turn influences how the tau lepton's momentum is distributed among its decay products and opens up an interesting possibility for distinguishing between the two decays and thus reducing the background stemming from W bosons. Figure 3.6 shows the helicity configurations in the rest frame of the decaying boson and the laboratory frame. The helicity of a massive particle is dependent on the frame of reference, as a Lorentz transformation can always be found between two frames in which the direction of the momentum of the particle is opposite.

---

<sup>1</sup>This fact is referred to as lepton universality. Small differences of the order of < 10% in the probabilities of W to decay to different leptons are due to their different masses.

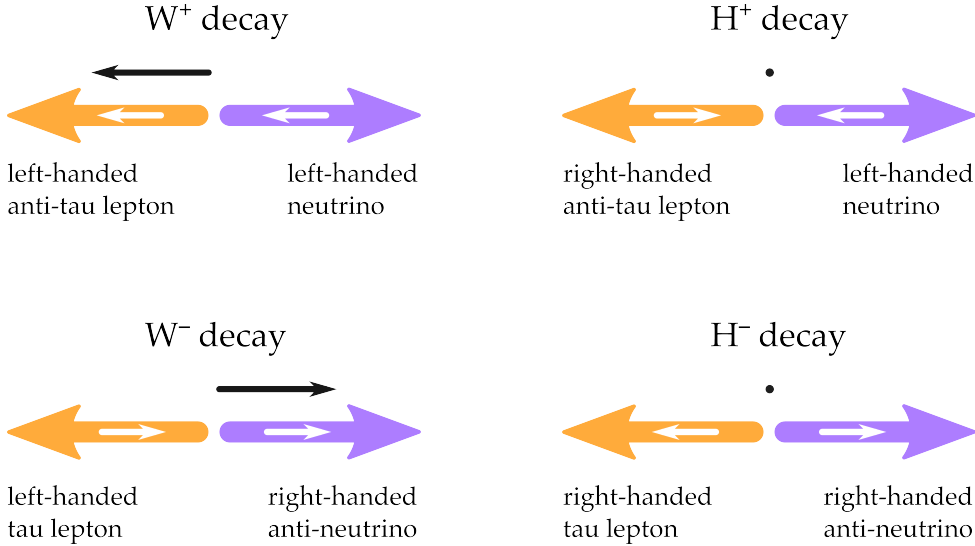


Figure 3.6: Momentum, spin direction, and handedness configurations of the tau leptons and neutrinos stemming from  $W$  and  $H^\pm$  boson decays. The situations are shown in the rest frame of the decaying boson. The violet arrows ( $\rightarrow$ ) represent neutrino momenta and the orange arrows ( $\rightarrow$ ) tau momenta. The smaller white and black arrows ( $\curvearrowright$ ,  $\curvearrowleft$ ,  $\longrightarrow$ ) indicate the direction of spin of the particle. The black dot ( $\bullet$ ) in the case of  $H^\pm$  indicates that its spin is 0.

In the present analysis,  $\tau$  leptons decaying to 1-prong jets are selected, because they are best suited for  $\tau$  identification. 1-prong decays account for 75% of hadronic all  $\tau$  decays and about 50% of all  $\tau$  decays. The main contributions to 1-prong hadronic  $\tau$  decays are

$$\begin{aligned}\tau^\pm &\rightarrow \pi^\pm \nu_\tau \quad (24.1\%), \\ \tau^\pm &\rightarrow \rho^\pm \nu_\tau \rightarrow \pi^\pm \pi^0 \nu_\tau \quad (53.8\%), \\ \tau^\pm &\rightarrow a_1^\pm \nu_\tau \rightarrow \pi^\pm \pi^0 \pi^0 \nu_\tau \quad (19.5\%),\end{aligned}$$

where the percentages represent the fraction of all hadronic 1-prong decays neglecting modes with neutral kaons. The above decay modes thus account for 97.4% of 1-prong  $\tau$  decays excluding  $K^0$ . All remaining modes, such as modes with more than two neutral pions, are considered negligible in the present discussion.

The differential decay width corresponding to the process  $\tau^\pm \rightarrow \pi^\pm \nu_\tau$  is

$$\frac{1}{\Gamma_\pi} \frac{d\Gamma_\pi}{d \cos \theta} = \frac{1}{2} (1 + P_\tau \cos \theta), \quad (3.28)$$

where  $P_\tau$  is  $+1$  ( $-1$ ) when the  $\tau$  is coming from a  $H^\pm$  ( $W^\pm$ ) decay and  $\theta$  is the angle between the charged pion's flight direction and the  $\tau$  lepton's spin quantization axis in the  $\tau$  rest frame, when the spin quantization axis is chosen to correspond to the  $\tau$  lepton's flight direction in the laboratory frame [43, 44]. The opposite sign of  $P_\tau$  for  $\tau$  leptons stemming from  $H^\pm$  and  $W$  decays is due to the fact that the  $\tau$  leptons coming from decays of the two different bosons have opposite helicity. This has an effect on the kinematics of the decay. If the  $\tau$  is coming from a charged Higgs boson, the charged pion will preferably be produced in the direction of the  $\tau$  lepton. On the other hand, if the  $\tau$  is coming from a  $W$  boson, the

charged pion will preferably be produced in the direction opposite to that of the  $\tau$  lepton. As the  $\tau$  neutrino goes undetected, the result is that the  $\tau$ -jets are typically *more energetic* when coming from a  $H^\pm$  than when coming from a  $W$ .

In the case of the  $\tau^\pm \rightarrow \rho^\pm \nu_\tau \rightarrow \pi^\pm \pi^0 \nu_\tau$  and  $\tau^\pm \rightarrow a_1^\pm \nu_\tau \rightarrow \pi^\pm \pi^0 \pi^0 \nu_\tau$  decays, the situation is more complicated, since the  $\rho^\pm$  and  $a_1^\pm$  mesons are massive spin-1 particles (vector mesons,<sup>2</sup> v) and thus can have both longitudinal ( $L$ ) and transverse ( $T$ ) polarization modes. The differential decay widths corresponding to the two polarizations are

$$\frac{1}{\Gamma_v} \frac{d\Gamma_{v,L}}{d \cos \theta} = \frac{1}{2} \frac{M_\tau^2}{M_\tau^2 + 2M_v^2} (1 + P_\tau \cos \theta), \quad (3.29)$$

$$\frac{1}{\Gamma_v} \frac{d\Gamma_{v,T}}{d \cos \theta} = \frac{M_v^2}{M_\tau^2 + 2M_v^2} (1 - P_\tau \cos \theta), \quad (3.30)$$

where  $\theta$  is the angle between the vector meson's and the  $\tau$  lepton's flight direction in the  $\tau$  rest frame.

The angle  $\theta$  in Eqs. (3.28) to (3.30) is given by

$$\cos \theta = \frac{2M_\tau^2}{M_\tau^2 - M_{\pi,v}^2} \times \frac{p_{\pi^\pm}}{p_{\tau\text{-jet}}} - 1, \quad (3.31)$$

Eqs. (3.28) to (3.31) show that the (visible)  $\tau$ -jets are more energetic when coming from  $H^\pm$  than from  $W$  if the  $\tau$  lepton decays directly to a charged pion or to a vector meson with longitudinal polarization. If the  $\tau$  lepton decays to a vector meson with transverse polarization, the opposite is true: here  $\tau$  leptons from  $W$  decays tend to produce more energetic jets than those from  $H^\pm$  decays.

It can also be shown that *longitudinal* vector meson polarization states tend to lead to jets in which the fraction of the jet's energy carried by the charged pion is either very large or very small, while *transverse* states favour a more even distribution between the energy of the charged pion and the neutral pions. The distributions of the differential decay widths for the different states is shown in Fig. 3.7. In the decay  $\tau^\pm \rightarrow \pi^\pm \nu_\tau$ , the charged pion is the only particle in the jet and thus carries all of its energy ( $X = X' = 1$ ).

The two above properties combined provide an opportunity to distinguish between  $\tau$ -jets coming from  $H^\pm$  and  $W^\pm$  decays. The situation is visualized in Table 3.2. Events with an energetic  $\tau$ -jet are selected and the charged pion is required to carry most of the momentum of the jet,  $X > 0.7$ . In practice, the charged pion is assumed to be the particle producing *leading track* of the jet, i.e. the charged-particle track that has the highest  $p_T$  of the tracks associated with the jet. The corresponding discriminating variable is

$$R_\tau \equiv \frac{p_{\text{leading track}}}{p_{\tau\text{-jet}}} \quad (3.32)$$

and the used selection requirement is  $R_\tau > 0.7$ .

---

<sup>2</sup>To be precise, the  $a_1^\pm$  is actually an *axial* vector meson, since it has parity  $+1$ , not  $-1$ . This is of no direct importance to the present discussion, which is why we simply refer to it as a vector meson.

	$\tau \rightarrow \pi$ or $\rho_L$ or $a_{1,L}$	$\tau \rightarrow \rho_T$ or $a_{1,T}$
$\tau$ from $H^\pm$	$\tau$ -jet more energetic X large or small	$\tau$ -jet less energetic X medium
$\tau$ from $W^\pm$	$\tau$ -jet less energetic X large or small	$\tau$ -jet more energetic X medium

Table 3.2: Properties of  $\tau$ -jets having different origins. A selection of more energetic jets will enhance the contribution of events lying on the diagonal, while a selection of jets in which the leading charged particle carries most of the energy will enhance the contribution of events in the first column. Applying both selections enhances the contribution of  $H^\pm$  events compared to background with decaying  $W$  bosons. These events have the properties shown in the highlighted cell.

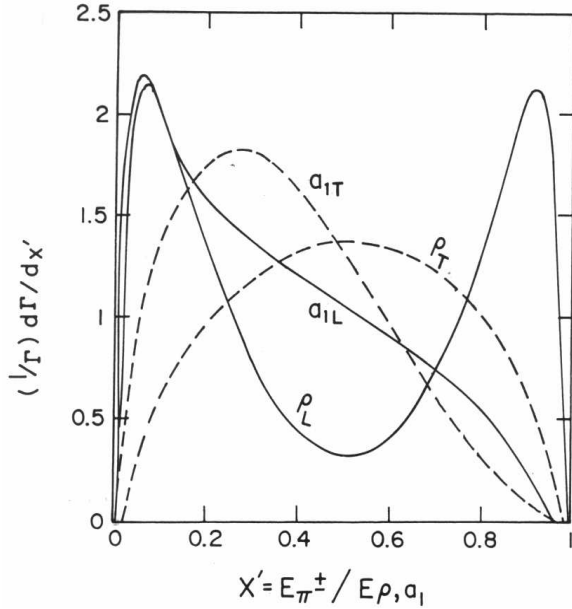


Figure 3.7: Distributions of the differential decay widths  $\tau^\pm \rightarrow \rho_{L,T}^\pm \nu_\tau \rightarrow \pi^\pm \pi^0 \nu_\tau$  and  $\tau^\pm \rightarrow a_{1,L,T}^\pm \nu_\tau \rightarrow \pi^\pm \pi^0 \pi^0 \nu_\tau$  as a function of the energy fraction carried by the charged pion. The distributions are calculated in the  $\tau$  lepton's rest frame but are similar in the laboratory frame. Taken from [44].

## 4 Large Hadron Collider and CMS experiment

Any sufficiently advanced technology  
is indistinguishable from magic.

---

Arthur C. Clarke

### 4.1 Large Hadron Collider

The Large Hadron Collider (LHC) is a particle accelerator set in a ca. 28-km-long ring-shaped tunnel west of the Swiss city of Geneva. It was built for the purpose of accelerating protons and heavy ions in two beams running in opposite directions and colliding them at four different *interaction points*, at each of which a detector system observes the collisions.

The main features of the LHC machine are superconducting radio frequency cavities that accelerate the particles as they pass through them; superconducting dipole magnets, which produce the homogeneous magnetic field necessary to bend the trajectories of the accelerated particles to keep them inside the accelerator; and quadrupole magnets for focussing the beams. There are also higher multipole magnets in place to control and shape the beam. The particles in the beams are grouped into bunches, of which there are 2808 per beam when running at design properties. In the case of protons being accelerated, there are about  $10^{11}$  protons in each bunch. The bunches pass through each other at the interaction points (*bunch crossing*), causing some of the protons to collide.

The proton energies of 4 TeV in the laboratory system that the LHC has achieved so far are the highest energies any human-made collider has reached to date, as of the preparation of this thesis. After the first long shutdown from February 2013 to somewhere in 2015, it will be tried to achieve the even higher design energies of 7 TeV.

Beside some smaller ones, four large experiments are in operation at the LHC, one at each of the four interaction points. They are the ALICE, ATLAS, CMS, and LHCb experiment. ATLAS and CMS are multi-purpose detectors designed to be able to study a wide range of phenomena, ALICE is optimized for studying heavy-ion collisions, and LHCb for studying the origins of the observed difference of the relative amounts of matter and antimatter in the Universe.

### 4.2 CMS experiment

The Compact Muon Solenoid (CMS) detector [45–47] of the LHC is situated in an underground cavern approximately 100 meters below ground at geographical coordinates  $46^{\circ}18'34''$  N,  $6^{\circ}4'37''$  E. CMS has the shape of a cylinder lying on its side, is 21.6 m long, has a diameter of 14.6 m, and weighs 12 500 metric tons. Its name-giving feature is a superconducting solenoid magnet, whose role is to produce a homogeneous magnetic field in which the trajectories of the charged particles are bent. Enclosed in the volume of the magnet is a tracking system, an electromagnetic calorimeter (ECAL), and a hadronic calorimeter (HCAL). Outside the main coil of the magnet is the iron return yoke, into which muon detectors are embedded. A sketched overview of the CMS detector is shown in Figure 4.1.

The nominal interaction point is at the geometric center of the detector. CMS is designed to be an multi-purpose detector and covers almost the full solid angle around the interaction point in order to detect and measure as many of the particles produced in the collisions as possible. A brief description of each of its subdetector systems is given in Section 4.2.1; detailed descriptions can be found in Refs. [45, 47].

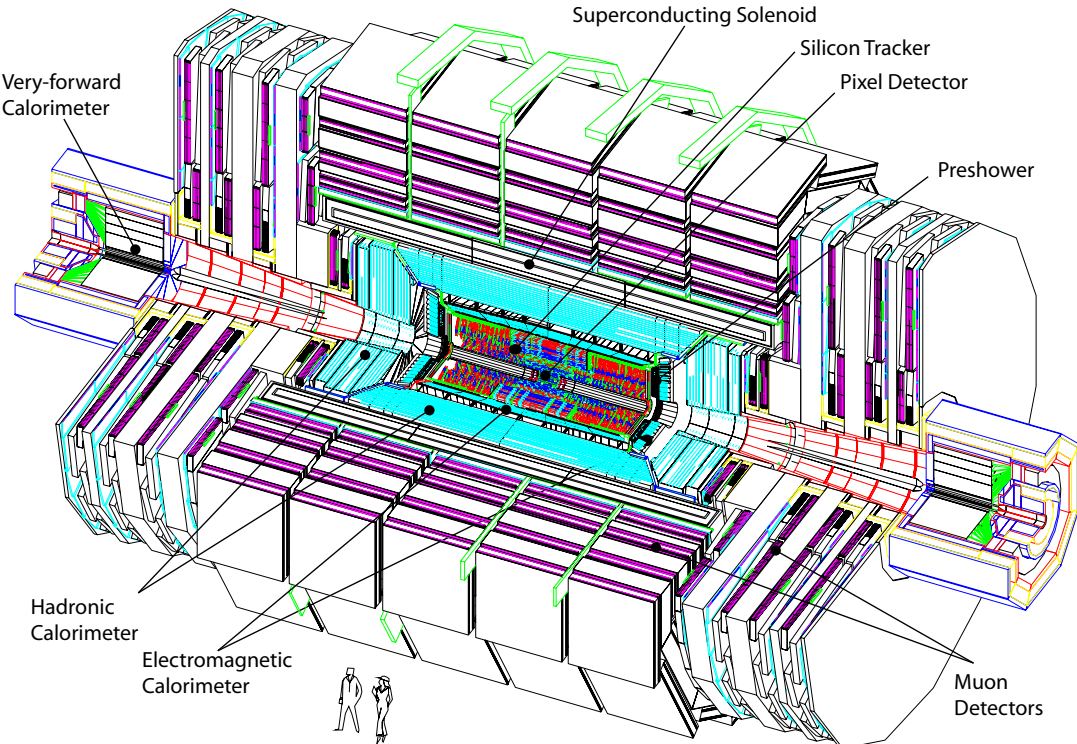


Figure 4.1: Schematic layout of the CMS detector with labeled subdetector systems. Two persons are depicted next to it for size comparison. Image by CMS Collaboration, CERN, March 2012.

#### 4.2.1 Anatomy of the CMS detector

The subdetectors are presented in the order starting from the center of the detector (the beam pipe) going outwards. This is the order in which they are encountered by stable particles produced at or near the interaction point. The detector consists of two types of regions, the barrel and the endcap. The barrel and endcap detectors are complemented by an extensive system of forward calorimeters very close to the beam. These are used for measuring jets (Section 5.7) in the forward direction, to improve the  $\vec{E}_T^{\text{miss}}$  measurement, and for monitoring the instantaneous luminosity (Section 4.3.2).

**Central tracker** The central tracker has inner layers of silicon pixels followed by outer layers of silicon strips. As the name suggests, it measures the tracks of charged particles. These are used to reconstruct the exact position of each collision (*primary vertex*) and the position of the decays of unstable particles that travel for a short distance, e.g. a few millimeters, before decaying (*secondary vertex*). The pixel detector measures the position of a

particle with a resolution of about 15  $\mu\text{m}$ .

The tracks are also used to determine the momenta of charged particles. This is possible because of the presence of the magnetic field created by the solenoid magnet. In this field, the trajectories of charged particles are bent due to the Lorentz force acting on them. The amount of bending—the radius of curvature—depends on their momentum, which can therefore be calculated if the trajectory is known. The direction of bending depends on the sign of the particle’s charge.

**Electromagnetic calorimeter** The electromagnetic calorimeter (ECAL) uses scintillating lead tungstate ( $\text{PbWO}_4$ ) crystals connected to photodetectors. The scintillation light created by the passage of energetic particles is detected by attached photomultiplier tubes. The electromagnetic calorimeter provides an energy measurement for all charged particles and photons, with the exception of muons, which usually pass through it without depositing much energy. Charged hadrons only deposit a part of their energy in the electromagnetic calorimeter.

**Hadronic calorimeter** The hadronic calorimeter (HCAL) measures the energy of neutral and charged hadrons. It plays a prominent role in the physics analyses because of the abundance of jets of hadrons (explained in Section 5.7) in the LHC experiments. The granularity of the hadronic calorimeter is about 25 coarser than that of the electromagnetic calorimeter.

The largest part of the hadronic calorimeter is made of alternating passive layers of brass and active layers of scintillating plastic with attached photodetectors for detecting the scintillation light. The role of the brass is to cause showering and absorb some of the particles’ energy to allow for a more compact design. This type of design is referred to as sampling calorimetry, because the presence of an absorber means that not all of the particles’ energy is deposited in the active medium and detected directly. The correct energy is calculated based on the amount observed directly.

**Solenoid magnet** The superconducting solenoid magnet produces a highly homogeneous magnetic field of about 3.8 Tesla, high enough to bend the trajectories even of very energetic particles sufficiently to be measured by the tracker. This allows the determination of the sign of their electric charge (at energies of up to about 1 TeV for muons) and their momentum. A large iron structure called the *magnetic return yoke* shapes the magnetic field outside the volume of the magnet.

**Muon system** The muon system is the furthest away from the beam and the only sub-detector in the barrel that is installed outside of the solenoid magnet’s volume. It consists of three different types of detectors using gas as an active medium. These are arranged in layers called *muon stations*, which are interleaved with the thick iron plates of the magnetic return yoke. The used detector types are aluminium drift tubes in the barrel of the detector and cathode strip chambers in the endcaps. These are complemented by resistive plate chambers in both regions. The latter give a less good position resolution than the drift tubes and cathode strip chambers, but provide a fast response and good time resolution. They can

therefore be used to identify the bunch crossing in which the muon was produced.

Figure 4.2 shows a cross section through the barrel of the CMS detector, along with example paths of different kinds of particles.

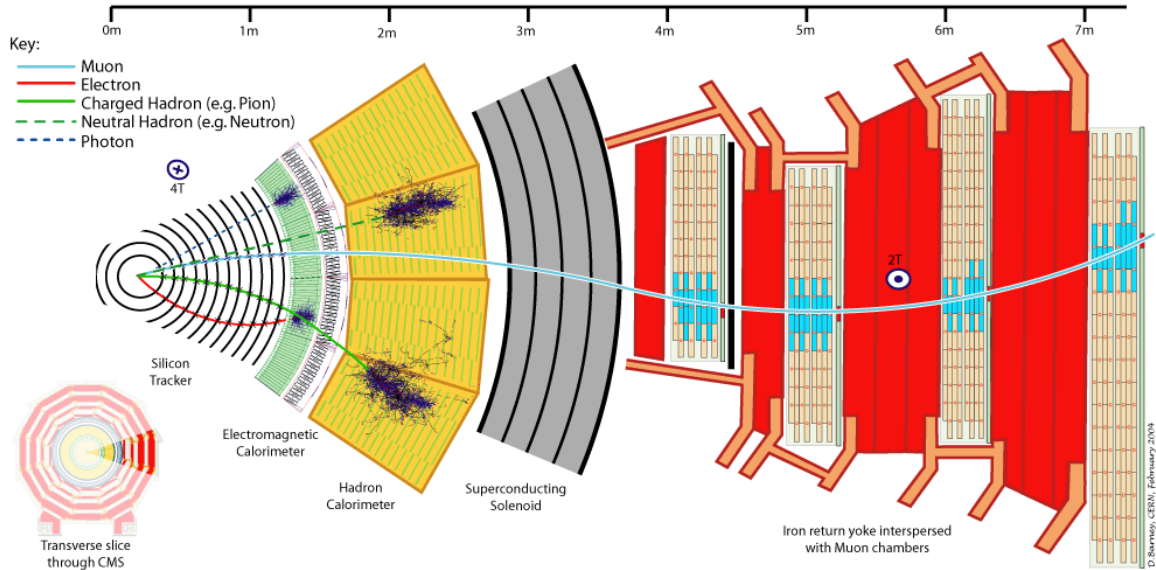


Figure 4.2: Cross section through CMS with example particle paths. Image by David Barney, CERN, February 2004.

### 4.3 Experimental conditions

At the LHC, data are not produced “continuously”, but in periods called *runs*. A run typically consists of producing stable, well-focussed beams; producing collisions and recording data; and finally dumping the beams by directing them into an absorber. The parameters characterizing each run that are most the important ones from the point of view of data analysis are described below.

#### 4.3.1 Center-of-mass energy

The center-of-mass (CM) proton collision energy is commonly expressed as  $\sqrt{s}$ , using the Mandelstam variable  $s = (p_{\text{beam } 1} + p_{\text{beam } 2})^2$ . As was explained in Section 2, the true CM energy of a hard collision depends on the momentum fractions of the colliding partons and is therefore generally not known. However, the energy of the proton-proton collisions is known and influences the probabilities—i.e. the cross sections—of the different particles processes that can occur in the collisions.

The design CM energy achieved by the LHC is 14 TeV, which is scheduled to be attained approximately in the year 2015. In 2011, the LHC produced collisions with a CM energy of  $\sqrt{s} = 7$  TeV. The data gathered during this time are the ones used for the presented analysis.

### 4.3.2 Instantaneous and integrated luminosity

The rate of collisions at a given interaction point of the LHC is expressed as the instantaneous luminosity  $\mathcal{L}$ . Multiplying  $\mathcal{L}$  by the probability of a given process ‘X’ to happen—expressed as a *cross section*  $\sigma_X$  in particle physics—gives the expected number of collision events in which this process X happens per unit of time. Integrating the luminosity over the time during which events were recorded yields the integrated luminosity

$$L = \int_{\text{data recording}} \mathcal{L}(t) dt. \quad (4.1)$$

Using the integrated luminosity, the expected total number of recorded events with the process X can be calculated as

$$N_X = L \times \sigma_X. \quad (4.2)$$

Therefore, the integrated luminosity is a convenient measure of the amount of collected data. It has dimension length<sup>-2</sup> and is expressed in fb<sup>-1</sup> in this analysis. For instance, an integrated luminosity of 5 fb<sup>-1</sup> means that 5 (5000) events of a process whose cross section is 1 fb (1 pb) are expected to have occurred.

During the runs in 2011, the peak luminosity was about  $40 \times 10^{32} \text{ cm}^{-2}\text{s}^{-1}$  and data corresponding to a total integrated luminosity of approximately 5.1 fb<sup>-1</sup> were collected.

### 4.3.3 Pile-up

Due to the high instantaneous luminosity achieved by the LHC, multiple collisions per bunch crossing are expected, referred to as *pile-up* of events. The expected number of collisions per bunch crossing in the 2011 runs was about six.

Pile-up can affect some event selection efficiencies and needs to be modelled in the MC-simulated event samples. A discrepancy between the distribution of number of pile-up events per bunch crossing between data and simulation is observed. This is corrected by applying weighting factors to the simulated events such that the resulting distribution matches that in data.

## 5 Event reconstruction

The CMS detector’s primary output is essentially a collection of voltage readouts of all the different subdetectors. However, the physics analyses are done in terms of the particles that caused these signals. Event reconstruction is the attempt to reconstruct the particles from the raw output of the detector. The reconstruction proceeds from considering individual sensors to subdetectors and combinations of subdetectors in order to reconstruct complex objects like charged-particle tracks or jets. The description of the reconstruction below follows the much more detailed discussion in Ref. [42] and has been updated to the current status of the presented analysis. The reconstruction of electrons and photons is only outlined very briefly, as they only play a small role in this analysis.

### 5.1 Tracking

All charged particles leave small depositions of energy, called *hits*, in the pixel and strip sensors of the track detector as they traverse it. Their trajectories are bent by the 3.8 T magnetic field into the shape of a helix. Deviations from a perfect helical shape are caused by small inhomogeneities in the magnetic field and energy loss of the particles to the sensors.

Charged-particle track reconstruction starts by finding pairs of pixel sensor hits compatible with a track hypothesis in the first two pixel detector layers, adding another hit from the third layer if one is found. The combination of three pixel hits—or two pixel hits plus a constraint from the position of the nominal interaction point in the transverse plane—form the track *seed*. The seed provides an initial estimate of the trajectory. The *combinatorial track finder* [48] uses a pattern recognition routine to add compatible hits in the subsequent sensor layers to the seeded track. This is done in six iterations, between which hits unambiguously assigned to some track are removed from the list of hits. This reduces the number of possible combinations and hence the computational load of the pattern recognition algorithm. After each iteration step, only tracks fulfilling the *high purity* criterion [49] are kept. Finally, a helix is fitted to the hits associated with the trajectory to obtain the best estimate of the track parameters. The efficiency of charged-particle track reconstruction has been measured to be  $\sim 99\%$  for isolated muons [50].

The track parameters are used to calculate the momentum of the charged particles. The momentum scale of the tracks has been studied using muons from cosmic rays and the decays of low-mass resonances:  $J/\psi$  decaying to two muons,  $K_S^0$  decaying to two charged pions, and  $\phi$  decaying to two charged kaons. The  $J/\psi$  mass peak positions extracted from the data and simulation were found to agree to within 1 MeV after calibration [51].

### 5.2 Primary vertices

A proton-proton interaction at LHC energies will typically produce at least some charged particles. Their reconstructed tracks can be used to find the position in space, where the interaction took place, called the *primary vertex*. In the presence of pile-up, events may contain several primary vertices.

Vertices are found by clustering the reconstructed charged particles with the *deterministic annealing algorithm* [52–54]. This algorithm has proven to perform well in a high-pile-up environment. The best estimate of the spatial position of each vertex is determined by

fitting with the *adaptive vertex fitter* [47, 55–58]. The position resolution of the vertex fit depends strongly on the number of tracks available for the fit as well as the momenta of the associated charged particles. For primary vertices with more than 30 tracks in minimum-bias events<sup>3</sup> the resolution was found to be  $\sim 25 \mu\text{m}$  in  $x$  and  $y$ , and  $\sim 20 \mu\text{m}$  in  $z$  [59].

### 5.3 Muons

Muons have the distinctive property of passing through large amounts of material that absorbs most other particles without depositing much energy. As such, they are typically the only particles that are not absorbed in the calorimeters and reach the muon detectors. An exception to this are neutrinos, which also reach the muon detectors, but the probability of a neutrino to interact with any of the detectors is extremely small. Other particles pass the calorimeters and reach the muon stations only rarely, in an effect called *punch-through*.

Because of their small amount of interaction, muons have a distinct detector signature: hits in the inner tracker forming a track, only a small amount of energy deposited in the calorimeters, and energy deposits in the muon detectors forming a track. Muon reconstruction starts with the separate reconstruction of tracks in the inner tracker and in the muon detector, after which two approaches are used to reconstruct muon candidates.

1. Global muon reconstruction. An inner tracker track matching the muon detector track is searched and a *global muon track* fitted to the combined hits in both subdetectors to give a global muon candidate. An example of what a global muon track might look like can be seen in Fig. 4.2. At large transverse momentum ( $p_T > 200 \text{ GeV}$ ), the global fit can improve the momentum resolution compared to the inner tracker fit alone [47, 60].
2. Tracker muon reconstruction. If an inner tracker track (with  $p_T > 0.5 \text{ GeV}$  and  $p > 2.5 \text{ GeV}$ ) that is extrapolated to the muon system matches at least one short track of muon detector hits (called a *muon segment*), it is classified as belonging to a tracker muon candidate. At low momenta ( $p < 5 \text{ GeV}$ ), tracker muon reconstruction is more efficient than global muon reconstruction, because only one muon segment is required in the muon system.

Muon identification is done based on the muon candidates with a *tight muon selection* [61]. Identified muons are required to be reconstructed both as a global and a tracker muon candidate. The muon trajectory has to have at least 1 hit in the pixel tracker, at least 11 hits in the strip tracker, at least 1 hit in the muon stations, and a transverse impact parameter with respect to the nominal interaction spot in the transverse plane of less than  $0.02 \text{ cm}$ . The fit to the trajectory has to have  $\chi^2/N_{\text{d.o.f.}} < 10$ , where  $N_{\text{d.o.f.}}$  is the number of degrees of freedom of the fit. Muon segments in at least two muon stations have to match the global muon track.

In many physics analyses, a distinction is made between muons from hard interactions and those being produced within hadronic jets. To separate the former from the latter, isolation criteria are defined. The idea is that a muon in a jet will generally have more additional particles and much larger energy deposits in the calorimeters near its flight direction. The

---

<sup>3</sup>*Minimum bias* means that the events have not been subjected to any kind of event selection. Whatever has happened in the collisions has simply been recorded. The reason why they are still not called *no-bias* events is that a genuinely unbiased detection of events is not possible due to limited detector coverage, sensitivity, etc.

*subdetector-based relative isolation* is defined as

$$I_{\text{rel}} = \frac{\sum p_T^{\text{track}} + \sum E_T^{\text{ECAL}} + \sum E_T^{\text{HCAL}}}{p_T^\mu}, \quad (5.1)$$

where the transverse momentum of tracks with  $p_T > 1$  GeV and the transverse energy deposits of the ECAL and HCAL cells in an isolation cone of  $\Delta R < 0.3$  around the muon track are summed. With the particle-flow reconstruction (Section 5.6) it is also possible to use *particle-based relative isolation*

$$I_{\text{rel}}^{\text{PF}} = \frac{\sum p_T^{\text{charged hadron}} + \sum E_T^{\text{photon}} + \sum E_T^{\text{neutral hadron}}}{p_T^\mu}, \quad (5.2)$$

where the transverse momenta or energies of reconstructed charged hadrons, photons, and neutral hadrons are summed in an isolation cone of  $\Delta R < 0.4$  around the muon track.

## 5.4 Electrons

Because of their low mass, electrons emit Bremsstrahlung photons when travelling in the tracker material, causing ECAL energy deposits that are spread out in the  $\phi$  direction because of the bending of the electron trajectory in the magnetic field. The emission of photons also causes energy loss to the electrons, affecting the curvature of the trajectory.

Electron reconstruction [62–64] is based on exploiting the above features. The clusters of energy deposit in the ECAL from the Bremsstrahlung photons with their characteristic spread in  $\phi$  are clustered into superclusters (clusters of clusters). The energy-weighted mean positions of the superclusters are used to find electron candidate track seeds by propagating backwards to the pixel detector. The electron candidate tracks are reconstructed using a modified algorithm that takes into account the significant energy losses that they exhibit due to emission of Bremsstrahlung photons.

## 5.5 Photons

Photons, being neutral particles, are not detected by the tracker. They do, however deposit their energy in the electromagnetic calorimeter. The simplest photon signature is thus an energy deposit in the ECAL with no track to match its direction. However, an additional effect needs to be taken into account: high-energy photons have a high probability ( $\sim 70\%$ ) of interacting with the material of the tracker, producing electron-positron pairs, in an effect called *photon conversion* [65].

Photon reconstruction [66] starts with the constructing of ECAL superclusters. An observable is constructed to determine if the photon was converted or not,

$$r_9 = \frac{E_{3 \times 3}}{E_{\text{supercluster}}}, \quad (5.3)$$

where  $E_{3 \times 3}$  is the energy within the  $3 \times 3$  array of ECAL crystals centered on the seed crystal of the supercluster and  $E_{\text{supercluster}}$  is the total energy associated with the supercluster. If  $r_9$  of a photon candidate is above 0.94 (0.95) in the ECAL barrel (endcap), the photon candidate is considered unconverted energy of the  $5 \times 5$  crystals around the crystal with the highest energy deposit is used. Otherwise, the photon candidate is considered converted and the energy of the supercluster is used.

## 5.6 Particle-flow event reconstruction

The particle-flow (PF) event reconstruction [67–70] uses the full information of all CMS subdetectors to reconstruct and identify all stable particles in the event. It distinguishes between the following types of stable particles: photon, charged hadron, neutral hadron, muon, and electron.

The operating principle of the PF reconstruction is to combine the information of several subdetectors in an optimal way to extract information that could not have been obtained by considering each subdetector separately. For instance, neutral hadrons can be spatially separated from charged ones by combining the information from the ECAL and HCAL. Neutral hadrons deposit an excess of energy in the HCAL with respect to what would have been expected based on information from the ECAL (which has 25 times finer granularity than the HCAL) and can thus be reconstructed separately with good resolution, even if they have deposited their energy in the same calorimeter cells as charged hadrons.

The particles reconstructed using the PF method can be used to cluster jets, to calculate the missing transverse energy, and to reconstruct hadronic  $\tau$  lepton decays [68].

## 5.7 Jets

A jet is a collimated spray of particles, mostly hadrons. Jets form when quarks and gluons are produced outside of hadrons. As these cannot exist freely, they *fragment* into multiple quark-antiquark pairs and gluons, which then quickly form bound states in a process called *hadronization*. The resulting hadrons make up the jet. The energy and direction of the jet are close to those of the original parton. This means that it is possible to relate parton-level calculations directly to experimental observables if the jets can be reconstructed. The steps required for reconstruction are grouping the energy deposits, tracks, or reconstructed particles into a jet (*jet clustering*) and calculating the momentum of the resulting jet. This can be (and is) done in different ways.

Jets produced as the result of a parton shower described above are called *hadronic jets*. There are also objects of a different origin appearing in the presented analysis, namely  $\tau$ -*jets*. These are produced when a  $\tau$  lepton decays hadronically. The  $\tau$ -jets considered in this analysis typically consist of only one or three charged and at most a few neutral pions (which quickly decay mostly to photons), and thus only leave one or three charged-particle tracks and energy deposits in the calorimeters as their signature. They are discussed in Section 5.9.

### 5.7.1 Types of reconstructed jets

In the CMS experiment, jets are reconstructed using four different kinds of inputs. Calorimeter jets [71] use the energy deposits in the electromagnetic and hadronic calorimeters. The *Jet-plus-Tracks* algorithm [72] takes a calorimeter jet and the momenta of charged particle tracks with it as input. It adds the momenta of the tracks to the jet and subtracts their expected energy deposition in the calorimeters. Particle-flow jets take the list of particles provided by the particle-flow event reconstruction as the input. Track jets [73] only use charged particle track information, providing a reconstruction method that is completely independent of the calorimetry and can be used for cross-checks.

### 5.7.2 Jet clustering algorithms

A good jet clustering algorithm should have the following properties [74].

1. It should be infrared and collinear safe, i.e. the associated observables should not change if a parton in it emits a soft parton (*infrared safety*), or if it splits into two partons travelling in the same direction (*collinear safety*).

An example of a (moronic) jet clustering algorithm that is clearly *not* infrared or collinear safe is this: “Take the 5 highest- $p_T$  tracks within a cone of opening  $\Delta R$  centered around the leading track as the jet.” If, for instance, each of the partons produced during fragmentation splits into two collinear partons, there could be twice as many tracks, while the total momentum is the same. If only the five leading tracks are counted, the momentum of the resulting jet would be smaller, so the algorithm is not collinear safe. Some infrared and collinear safe algorithms are presented below.

2. The jet direction and energy should correspond closely to those of the original parton, since the association of jets with energetic partons is a basic assumption when theoretical predictions are compared to data.
3. Soft processes related to the beam remnants (what is left of the colliding protons after the hard interaction) should not influence it.
4. Experimental uncertainties should be small.
5. It should have small systematic uncertainties and corrections associated with the theoretical description of hadronization as well as the QCD factorization and renormalization scales.
6. The same jet definition should be simple to use in experiments, simulations, and theoretical calculations without any modifications in order to provide a common description.

The different jet clustering algorithms relevant to the presented analysis are listed below.

**Iterative cone algorithm (with progressive removal)** [47,74,75] This algorithm is not collinear safe, since jets are seeded by first identifying the most energetic particle in them. If this particle, say  $P_1$ , would split into a (nearly) collinear pair of particles,  $P_{1a}$  and  $P_{1b}$ , another particle  $P_2$  might become the most energetic particle. Since  $P_2$  will in general have a different direction than  $P_1$ , this would change the resulting jet.

The collinear unsafety makes the algorithm unsuitable for comparing data to theoretical predictions. In the presented analysis, it is nevertheless used in the high-level trigger for fast calorimeter-based  $\tau$ -jet reconstruction.

**Inclusive  $k_T$  algorithm** [47, 75–79] This collinear and infrared safe algorithm is used in the calculation of the average energy density in the events as well as the jet energy corrections.

**Anti- $k_T$  algorithm** [80] The jets clustered with this collinear and infrared safe algorithm are the ones used for the analysis of the selected events.

### 5.7.3 Jet momentum assignment

If the four-vectors of the jet constituents are simply added together to give the resulting momentum  $p$  of the jet, this will in general produce a massive jet, i.e. one for which  $m_{\text{jet}} = p_\mu p^\mu \neq 0$ . Massless jets are produced using the  $E_T$  scheme, which consists of setting the transverse momentum of the jet equal to sum of the transverse energies of the jet constituents and subsequently fixing the direction of the jet depending on the used clustering algorithm [47]:

$$\sin \theta = \frac{\sum E_T}{E_{\text{jet}}} \quad (\text{iterative cone algorithm}), \quad (5.4)$$

$$\eta = \frac{\sum E_{T,i} \eta_i}{\sum E_T}, \quad \phi = \frac{\sum E_{T,i} \phi_i}{\sum E_T} \quad (k_T \text{ algorithms}), \quad (5.5)$$

where the sums are over jet constituents. In both cases  $m_{\text{jet}} = p_\mu p^\mu = 0$ .

## 5.8 Identification of b-jets

Beauty quarks ( $b$ ) appear in many particle physics processes of interest. Therefore, dedicated algorithms have been developed for identifying jets originating from the hadronization of a beauty quark, referred to as *b-jets*. These make use of distinct features of hadrons containing a beauty quark, such as their relatively high masses, long lifetimes, hard fragmentation, and relatively high fraction of semileptonic decays to distinguish *b-jets* from those originating from gluons and other quarks, collectively called *light jets*.<sup>4</sup> The identification of *b-jets* is referred to as *b-tagging*.

Each algorithm produces a numerical *discriminator* for each jet, which quantifies the probability that the jet originates from a beauty quark. A working point in the efficiency-versus-purity space is chosen by selecting a threshold value for the discriminator.

The presented analysis uses the *combined secondary vertex* method [81] at the *tight* working point for *b*-tagging. The *tight* working point has been chosen such that the mistagging rate of light jets as *b-jets* is about 0.1% for jets with  $p_T \approx 80$  GeV, estimated based on Monte Carlo simulation.

## 5.9 Identification of $\tau$ -jets

Produced  $\tau$  leptons quickly decay to hadrons, to an electron, or to a muon, as discussed in Section 3.3.3. Because of the short lifetime of the  $\tau$  an electron or a muon produced in a  $\tau$  decay is hard to distinguish from one produced promptly in a hard interaction. The presented analysis selects hadronically decaying  $\tau$  leptons producing  $\tau$ -jets. The  $\tau$ -jets are characterized by a low track multiplicity, typically featuring only one or three charged particle tracks. In addition, they may contain neutral hadrons. These are mostly neutral pions, which quickly decay, each producing a pair of photons ( $\mathcal{B}(\pi^0 \rightarrow \gamma\gamma) \approx 99\%$  [1]).

The  $\tau$ -jets used in the presented analysis are identified using the *Hadrons-plus-Strips* (HPS) algorithm [82, 83]. The HPS algorithm makes use of the list of particles obtained with the

---

<sup>4</sup>In the literature, jets originating from a charm quark are often not considered *light* because the charm quark is relatively massive and in some respects similar to the beauty quark. Here, however, they are included in the definition for convenience.

particle-flow (PF) event reconstruction. It starts from a PF-jet and searches the constituent particles for possible  $\tau$  lepton decay products. The considered  $\tau$  decay modes are

$$\begin{aligned}\tau^\pm &\rightarrow h^\pm \nu_\tau, \\ \tau^\pm &\rightarrow h^\pm \pi^0 \nu_\tau, \\ \tau^\pm &\rightarrow h^\pm h^\pm h^\mp \nu_\tau.\end{aligned}$$

The photon pair from the neutral pion decay can be converted further to an electron-positron pair by interacting with the material of the tracker (see Section 5.5). Photon conversion typically leads to energy deposits in the ECAL that are spread out in the azimuthal ( $\phi$ ) direction because of the bending of the  $e^\pm$  trajectories in the magnetic field. This was taken into account by combining the PF-reconstructed photons in *strips* in the  $\phi$  direction.

All reconstructed charged hadrons and strips have to be contained within a narrow cone of opening  $\Delta R < 2.8/p_T^\tau$ , where  $p_T^\tau$  is calculated by summing the momenta of the charged hadrons and strips in the transverse plane. In the case that the observed signature is consistent with more than one considered  $\tau$  decay signature, the decay mode with the smallest  $\sum E_T$  of those jet constituents *not* associated with the  $\tau$  decay is selected.

At this point in the reconstruction, most of the reconstructed  $\tau$ -jet candidates are hadronic jets that happen to have a signature compatible with a  $\tau$  decay hypothesis. To identify the genuine  $\tau$  decays, one makes use of the fact that  $\tau$ -jets tend to be significantly narrower than hadronic jets. This is implemented by imposing an isolation requirement. An isolation cone of opening  $0.3 < \Delta R < 0.5$  centered around the leading track of the  $\tau$ -jet is defined. All particle-flow photons with  $E_T > 0.5$  GeV inside the isolation cone are considered. All charged hadrons inside the isolation cone satisfying the following requirements are considered: transverse impact parameter (closest approach of linearly extrapolated track to beam axis)  $< 300$   $\mu\text{m}$ , at least 2 hits in the pixel detector, a total of at least 3 hits in the central tracker, and a transverse momentum above a certain threshold depending on the chosen isolation scenario:

**Loose**  $p_T > 1.0$  GeV

**Medium**  $p_T > 0.8$  GeV

**Tight**  $p_T > 0.5$  GeV

The considered particles are used to calculate the quantity

$$E_T^{\text{isolation}} = \sum_{IP_z < 2 \text{ mm}} p_T^{\text{charged hadrons}} + \min(0, \sum E_T^{\text{photons}} - k \times \sum_{IP_z > 2 \text{ mm}} p_T^{\text{charged hadrons}}), \quad (5.6)$$

where the sums include the considered particles in the isolation cone and  $IP_z$  is the longitudinal impact parameter, i.e. the distance along the  $z$  direction of the point of closest approach of the linearly extrapolated track to the beam axis. The second term contains a correction for particles that are likely to come from a pile-up vertex ( $IP_z > 2$  mm). The isolation requirement depends on the isolation scenario:

**Loose**  $E_T^{\text{isolation}} < 2.0$  GeV

**Medium**  $E_T^{\text{isolation}} < 1.0$  GeV

**Tight**  $E_T^{\text{isolation}} < 0.8$  GeV

In the presented analysis, the *medium* scenario was chosen.

## 5.10 Missing transverse energy

Three algorithms have been developed in CMS to reconstruct the missing transverse energy,  $E_T^{\text{miss}}$ .

*Particle-flow*  $E_T^{\text{miss}}$  is calculated using all particles reconstructed with the PF method (see Section 5.6). Since these objects already incorporate all detector information, the PF- $\vec{E}_T^{\text{miss}}$  is simply the negative vector sum of the transverse momenta of all the PF-particles. The PF- $\vec{E}_T^{\text{miss}}$  is used in the presented analysis.

*Calorimeter*  $E_T^{\text{miss}}$  [84] is calculated using the energy deposits in the calorimeters and their directions relative to the geometrical center of the detector. Energy deposits below a noise threshold are excluded from the calculation. In this method, the momentum contribution from muons must be taken into account separately, since they only deposit a small fraction of their energy in the calorimeters. Moreover, this deposited energy is largely independent of the muon momenta. Therefore, the momenta of the muons are included in the calorimeter  $E_T^{\text{miss}}$  calculation, while the small calorimetric energy deposits associated with the muon tracks are excluded.

*Track-corrected*  $E_T^{\text{miss}}$  [85] is similar on the calorimeter  $E_T^{\text{miss}}$ , but includes the momenta associated with all reconstructed charged particle tracks while removing the expected calorimetric energy deposits associated with them. The expected calorimetric energy deposits of the tracks are estimated treating all tracks not identified as belonging to an electron or a muon as belonging to charged pions.

### 5.10.1 Missing transverse energy corrections

The  $\vec{E}_T^{\text{miss}}$  can be mismeasured for a variety of reasons: non-linear response of the calorimeters, different calorimeter response to electromagnetic and non-electromagnetic components of the hadron shower [86], minimum energy thresholds of the calorimeters, and momentum thresholds and inefficiencies in the tracker cause bias. The calorimeter  $\vec{E}_T^{\text{miss}}$  suffers from additional bias because the direction of a calorimeter deposit can be significantly different from the original direction of the particle causing it due to the bending of the track in the magnetic field.

In the following, the corrections applied to the particle-flow  $\vec{E}_T^{\text{miss}}$  are discussed, because this type of missing transverse energy was used in the presented analysis. In order to remove the bias described above in the PF- $\vec{E}_T^{\text{miss}}$  reconstruction, a two step correction system has been devised [87]. To apply the correction, the contributions to the missing energy coming from hadronic jets,  $\tau$ -jets, isolated high- $p_T$  photons, isolated high- $p_T$  electrons, isolated muons, and unclustered energy deposits are considered separately. Isolated photons, electrons, muons, and  $\tau$ -jets are assumed to require no energy scale corrections. *Type-I*  $\vec{E}_T^{\text{miss}}$  corrections of the  $\vec{E}_T^{\text{miss}}$  consist of applying energy scale corrections to all jets with corrected  $p_T > 10$  GeV before calculating the  $\vec{E}_T^{\text{miss}}$ . *Type-II*  $\vec{E}_T^{\text{miss}}$  corrections are done by applying corrections to jets falling below this  $p_T$  threshold as well as unclustered energy deposits. The corrections were obtained using  $Z \rightarrow ee$  events [87].

Further sources of mismeasurement of the  $\vec{E}_T^{\text{miss}}$  include underlying event activity, pile-up, detector noise, and limited detector acceptance.

## **Part II**

# **Data Analysis**

## 6 Event simulation

As most background contributions are estimated from data, the simulated samples are mainly used for testing of algorithms and validation. However, the background contribution from electroweak and  $t\bar{t}$  events without a genuine  $\tau$  lepton is estimated from simulation. In addition, the QCD multijet background measurement uses a sample that is the difference of experimental data events and simulated EWK and  $t\bar{t}$  events. The simulated  $H^\pm$  samples are used to assess what a possible signal might look like.  $H^\pm$  samples were simulated for  $M_{H^\pm} = 80, 90, 100, 120, 140, 150, 155$ , and  $160$  GeV. To save space and keep readability at a reasonable level, many distributions appearing later in this thesis are only shown for  $M_{H^\pm} = 80, 100, 120, 140, 150$ , and  $160$  GeV. These values have been chosen to spread the entire studied mass range and ensure that all the essential information is conveyed. The final results in Section 10 are shown for all  $H^\pm$  mass values.

Simulation of QCD multijet background is difficult to do, since unfeasably large amounts of simulated events would be required for an adequate description. In addition, the uncertainty related to QCD simulations is large and it is not known, whether the simulated background corresponds to the true situation at all. In the analysis, the multijet background is measured experimentally instead of simulated, circumventing the problem. On the other hand, many of the figures presented later in this thesis show a background based on simulation. In such figures, the QCD multijet background is always omitted, which is indicated by the text *QCD background not shown*.

TAUOLA [88–90] was used to simulate all tau decays. It incorporates proper treatment of the tau polarization effects. This was essential to our analysis, as the polarization effects were exploited to suppress the background of genuine taus from W decays.

Type of simulation	Events/process	Monte Carlo program
Background events	$t\bar{t}$	MADGRAPH 5 [91,92]
	W+jets	MADGRAPH 5
	$Z/\gamma^*+jets$	MADGRAPH 5
	Diboson (WW, WZ, ZZ)	PYTHIA 6 [93]
Signal events	Single top	POWHEG [94–96]
	$HH (t\bar{t} \rightarrow H^+ b H^- \bar{b})$	PYTHIA 6
	$HW (t\bar{t} \rightarrow H^+ b W^- \bar{b})$	PYTHIA 6
Particle process	All $\tau$ decays	TAUOLA
	Fragmentation and hadronization	PYTHIA 6
Detector simulation	All	GEANT4 [97,98]

Table 6.1: Overview over the different simulated background contributions.

All signal and background parton-level samples are processed with PYTHIA 6 [93] to simulate parton fragmentation and hadronization processes.

The final step is to simulate the response of the CMS detector. This is done using the GEANT44 [97,98] toolkit and a centrally maintained implementation of the CMS detector's specifications.

## 7 Event selection

Data! Data! Data! I can't make bricks without clay!

---

Sherlock Holmes

### 7.1 Online event selection: trigger

The online event selection is done with a trigger requiring a single tau with  $p_T > 35$  GeV decaying hadronically and missing transverse energy  $E_T^{\text{miss}} > 45, 60$  GeV in the calorimeters, depending on the run era. The use of a combined  $\tau$ -and- $E_T^{\text{miss}}$  trigger has the advantage of allowing a low tau  $p_T$  trigger threshold while still having a sufficiently high event rate suppression. The leading track of the  $\tau_h$  is required to have  $p_T > 20$  GeV. The precise trigger thresholds at all the different levels are listed in Appendix A.

The events passing the trigger are still mostly QCD multijet events. This fact is exploited by the data-driven multijet background measurement methods described in Section 8. Further selection criteria are applied to the triggered events at the offline selection stage to reject more background.

### 7.2 Offline event selection

#### 7.2.1 Data quality selection steps

In the offline selection, the primary vertex is selected as the one whose associated tracks' transverse momenta squared add up to the highest value. It is required to lie within 2 cm of the  $z$ -axis and less than 24 cm away from the nominal collision point along the  $z$ -axis. In events with more than 10 charged-particle tracks, at least 25% of the tracks are required to fulfill the *high-purity* requirement presented in Ref. [49]. Events are rejected if they coincide with significant noise in the hadron calorimeters [99].

#### 7.2.2 Main selection steps

One reconstructed  $\tau$  *candidate* within  $\Delta R < 0.4$  of the high-level trigger  $\tau_h$  object that triggered the online selection is required. A  $\tau$  candidate is an object that was reconstructed using the Hadron-Plus-Strips algorithm [82] having  $p_T > 41$  GeV,  $|\eta| < 2.1$ , as well as a leading track with  $p_T > 20$  GeV. In addition, it has to pass selections relying on boosted decision trees (see e.g. Ref. [100] and references therein) designed to reject objects that appear as tau jets but are really electrons or muons.

The  $\tau_h$  candidate is subjected to further selection criteria. An isolation cone of opening  $\Delta R = 0.5$  around the leading track of the  $\tau$ -jet is defined, inside which there may only be a small amount of energy deposits from charged hadrons or photons not belonging to the  $\tau$ -jet (Section 5.9). [82] To achieve a further reduction of the QCD multijet background, only  $\tau$ -jets with one charged particle track (called *1-prong*) are accepted. The fraction of  $\tau$ -jets coming from the decay  $W \rightarrow \tau_h \nu$  is suppressed using the method explained in Section 3.4.3, by requiring  $R_\tau > 0.7$ . This threshold value for the polarization variable  $R_\tau$  was chosen

because it was found to give the most stringent expected exclusion limit. A tau candidate passing these requirements (isolation, number of tracks, polarization) are referred to as an *identified tau*. Only a negligible amount of events contained more than one identified tau.

In addition to the identified  $\tau$ -jet, events are required to have at least three more jets with  $p_T > 30 \text{ GeV}$ ,  $|\eta| < 2.4$ , of which at least one is identified as originating from a b-quark. Furthermore, selected events must have  $E_T^{\text{miss}} > 60 \text{ GeV}$ , with the missing energy direction and the transverse direction of the  $\tau$ -jet satisfying  $\Delta\phi(\tau\text{-jet}, E_T^{\text{miss}}) < 160^\circ$ .

Events with an isolated electron (muon) with  $p_T > 15 \text{ GeV}$  ( $p_T > 10 \text{ GeV}$ ) were rejected.

The selection steps described up to this point are applied to all signal candidate events. In addition, there are selections that are being tested as of the preparation of this thesis. They are described in the following sections. Results will be shown and compared for all the scenarios presented here.

### 7.2.3 Collinear and back-to-back cuts for jets and missing transverse energy

In order to suppress the QCD multijet background in the transverse mass region where a possible signal might appear, additional selections are applied. *Cut areas* were defined in the  $\Delta\phi(\tau\text{-jet}, E_T^{\text{miss}})$ - $\Delta\phi(\text{jet}_n, E_T^{\text{miss}})$  plane, where  $n = 1, 2, 3$  is the reconstructed PF jet with the highest, second highest, third highest  $p_T$ , respectively. Events falling inside these cut areas are rejected ('cut away', hence the name). This improves the signal-to-background ratio in the signal region.

There are two disconnected cut areas. The first is in the area where  $\Delta\phi(\tau\text{-jet}, E_T^{\text{miss}})$  is close to  $0^\circ$ , meaning that the  $\tau$ -jet and the  $\vec{E}_T^{\text{miss}}$  are collinear. The second is in the area where  $\Delta\phi(\tau\text{-jet}, E_T^{\text{miss}})$  approaches  $180^\circ$ , meaning that  $\tau$ -jet and the  $\vec{E}_T^{\text{miss}}$  are back-to-back. Because of this, the two areas are referred to as the *collinear* and *back-to-back* area. The collinear area is a triangle with short sides of length  $40^\circ$ . For the back-to-back cut, four different scenarios were defined. The definitions are given in Table 7.1. The cut areas are shown in Figure 7.1.

Scenario name	Back-to-back cut
None	No cut
Loose	Circular, $40^\circ$
Medium	Circular, $60^\circ$
Tight	Circular, $80^\circ$

Table 7.1: Back-to-back cut scenarios.

### 7.2.4 Top quark invariant mass selection

During the reconstruction of the invariant mass of the tau-and-neutrino system, the invariant mass of the parent top quark of the system,  $m_t$ , may also be reconstructed. Different scenarios for rejecting events in which  $m_t$  falls outside a certain range centered around the top quark rest mass are tested. These are described in Section 9.5.3. Results are shown for each scenario.

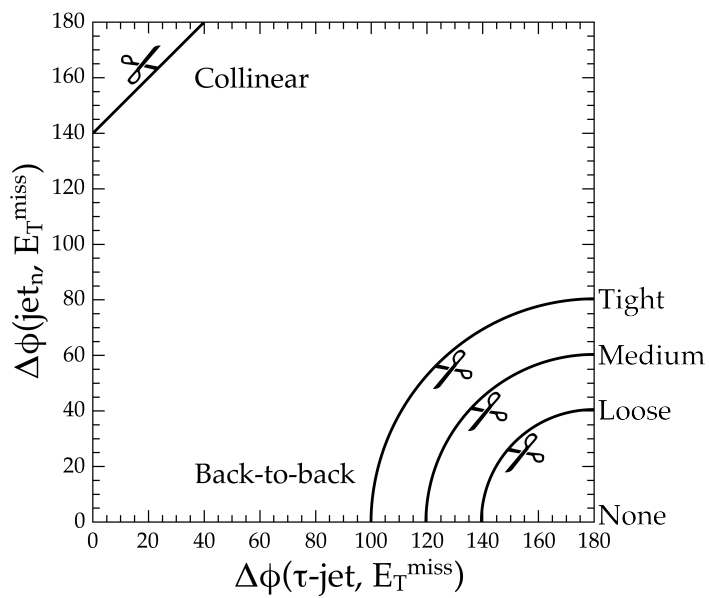


Figure 7.1: The collinear and back-to-back cut areas. Events lying on the same side of the cut line as the scissors are rejected.

## 8 Data-driven background determination

In order to reduce the systematic uncertainty of the background event yields and to increase the overall soundness of the analysis, it is aspired to measure most of the backgrounds experimentally instead of simulating them. Two different methods are used simultaneously, one for background with a genuine  $\tau$  lepton (electroweak) and one for background without one (QCD multijets).

### 8.1 Measurement of background with genuine $\tau$ leptons

The guiding idea for measuring the background with a genuine  $\tau$  is based on lepton universality: since the gauge bosons and photons couple to all three lepton flavours with the same strength, there should be as many electroweak events of a given kinematical configuration with a  $\tau$  lepton as there are with a muon or an electron. This statement would be exactly true if all charged leptons had the same mass. In fact, there are small corrections due to their different masses, but the statement still holds approximately. For instance,  $\mathcal{B}(W \rightarrow \tau\nu_\tau) = (11.25 \pm 0.20)\%$  is approximately equal to  $\mathcal{B}(W \rightarrow \mu\nu_\mu) = (10.57 \pm 0.15)\%$  [1]. On the other hand, the coupling of possible charged Higgs bosons to muons is thought to be much weaker than to tau leptons precisely because of their different mass, i.e.  $\mathcal{B}(H^+ \rightarrow \tau\nu_\tau) \gg \mathcal{B}(H^+ \rightarrow \mu\nu_\mu)$ .

This means that by selecting events that are otherwise identical to the signal events but with a single muon instead of a single  $\tau_h$ , one can obtain an estimate of the distribution of background events with genuine  $\tau$  leptons. If charged Higgs bosons exist, there will still be very little signal contamination in the measured background since they are expected to decay to muons very rarely.

The muon events are triggered with a single muon trigger. Events with an isolated muon and at least three jets are selected offline. Events with additional isolated muons or electrons are rejected. The identified muon is then removed from the event and replaced with a hadronically decaying  $\tau$  that was *simulated* and reconstructed. This step is called *tau embedding* and leads to a *hybrid event*, in which there is a  $\tau$  decay from simulation while all other physics objects are from data. After embedding, the  $E_T^{\text{miss}}$  is recalculated and the remaining event selection steps described in Section 7.2 are applied.

The hybrid event sample is used as the genuine  $\tau$  background, i.e. as the sum of  $t\bar{t}$ ,  $W+\text{jets}$ ,  $Z/\gamma^*+\text{jets}$ , diboson, and single-top-quark events with genuine  $\tau$  leptons.

The final step is to normalize the background shape to take into account the different trigger and selection efficiencies in the signal and embedding samples. The normalization or total number of genuine  $\tau$  background events is calculated as

$$N^{\text{genuine } \tau \text{ background}} = (1 - f_{W \rightarrow \tau \rightarrow \mu}) \times \frac{1}{\varepsilon^\mu \text{ selection}} \times \sum_i^{\tau\text{-jet } p_T \text{ bins}} N_i^{\text{selected hybrid events}} \varepsilon_i^\tau \text{ trigger}, \quad (8.1)$$

which contains the following symbols:

$f_{W \rightarrow \tau \rightarrow \mu}$  denotes the fraction of  $W \rightarrow \tau\nu_\tau \rightarrow \mu\nu_\mu\nu_\tau$  events of all selected  $W \rightarrow \mu\nu_\mu$  events.  
As these events constitute an excess with respect to the  $W \rightarrow \tau\nu_\tau$  events, the normalization (8.1) is proportional to  $(1 - f_{W \rightarrow \tau \rightarrow \mu})$ .

$\varepsilon^{\mu}$  selection is the muon trigger and offline selection efficiency.

$N_i^{\text{selected hybrid events}}$  is the number of observed hybrid events in the  $i$ th  $\tau$ -jet  $p_T$  bin passing the event selection and a calorimeter  $E_T^{\text{miss}} > 60$  GeV requirement whose function is to emulate the  $E_T^{\text{miss}}$  part of the signal trigger. The calorimeter  $E_T^{\text{miss}}$  of the hybrid event is calculated by adding the calorimeter  $E_T^{\text{miss}}$  vectors of the original muon event and the  $\tau$  decay simulation and taking the norm of the resulting vector.

$\varepsilon^{\tau_i}$  trigger is the  $\tau$  trigger efficiency in the  $i$ th  $\tau$ -jet  $p_T$  bin.

This background measurement method makes use of the fact that CMS is able to reconstruct muons with a good efficiency and momentum resolution, and thus highlights the advantages of an extensive muon system. Electrons might have been used instead of muons, but this would yield less good results, as electrons are much harder to distinguish from other particles and their momentum measurement is less precise.

## 8.2 Measurement of QCD multijet background

QCD multijet events only rarely contain genuine  $\tau$  leptons, but can also pass the event selection due to misidentification of a hadronic jet as a  $\tau$ -jet and an imbalance in the energy measurement of the jets leading to ‘fake’ missing transverse energy that is an experimental artefact.

The starting point of the data-driven background estimation is the fact that the event sample is still heavily dominated by QCD multijet events after some selections. The situation changes when the  $\tau$  identification selections are applied, which lead to a great reduction of their fraction. The idea is then to *not* apply these final selections, but instead take the full data sample, subtract the simulated electroweak and  $t\bar{t}$  background and multiply the resulting data-minus-EWK& $t\bar{t}$  sample with the combined efficiency of the left-out selections.

All of the described steps are performed in bins of  $\tau$ -jet candidate  $p_T$ , for two reasons. First, the probability of a quark or a gluon jet to pass the isolation and  $R_\tau$  requirements of the  $\tau$ -jet identification was found to depend on the jet  $p_T$ . Second, a small correlation was found between the  $E_T^{\text{miss}}$  and  $\tau$ -jet identification selection requirements, which can be reduced to a negligible level by measuring the efficiency in  $\tau$ -jet candidate  $p_T$  bins. The bins were chosen such that each contained a sufficient number of events: 41–50, 50–60, 60–70, 70–80, 80–100, 100–120, 120–150, and 150– $\infty$  GeV.

The total number of QCD multijet events in the signal region and the shapes of their transverse and invariant mass distributions are measured separately. In the analysis, the mass distributions are normalized to the number of events.

### 8.2.1 Number of QCD multijet events

Events were required to pass the  $\tau$ -and- $E_T^{\text{miss}}$  signal trigger as well as the primary vertex,  $\tau$ -jet candidate, isolated muon or electron veto, and hadronic jet offline selections. These selections are hereafter called the *common selections*, since they are common to the signal and QCD multijet background sample selection. After the common selections, QCD multijet events constitute about 97–99% of the sample in 2011 data.

For the background measurement, the  $E_T^{\text{miss}}$ , b-tagging, and  $\Delta\phi(\tau_h, E_T^{\text{miss}})$  selections—collectively referred to as the *factorized selections*—were *not* applied to the events, but instead their combined efficiency was calculated as

$$\varepsilon_i^{E_T^{\text{miss}} + \text{b-tag} + \Delta\phi} = \frac{N_{\text{common+factorized}, i}^{\text{data}} - N_{\text{common+factorized}, i}^{\text{EWK+}\bar{t}\bar{t}}}{N_{\text{common}, i}^{\text{data}} - N_{\text{common}, i}^{\text{EWK+}\bar{t}\bar{t}}} \quad (8.2)$$

in the  $i$ th  $\tau$ -jet  $p_T$  bin, where the symbol  $N_X^{\text{data}}$  and  $N_X^{\text{EWK+}\bar{t}\bar{t}}$  are the numbers of events after selections  $X$  for experimental data and for EWK+ $\bar{t}\bar{t}$  simulation, respectively. The fraction of QCD events after the common and factorized selections is around 84–94% in 2011 data.

Finally the  $\tau$  identification selection is applied to the events and the total number of QCD multijet events calculated as

$$N^{\text{QCD events}} = \sum_i^{\tau\text{-jet candidate } p_T \text{ bins}} \left( N_{\text{common+}\tau \text{ ID}, i}^{\text{data}} - N_{\text{common+}\tau \text{ ID}, i}^{\text{EWK+}\bar{t}\bar{t}} \right) \varepsilon_i^{E_T^{\text{miss}} + \text{b-tag} + \Delta\phi} \quad (8.3)$$

### 8.2.2 Transverse mass distribution of QCD multijet events

For the measurement of the transverse mass distribution shape, the common selections are applied before calculating the efficiency of the  $\tau$  identification selections (isolation, 1-prong, and  $R_\tau$  requirements), defined as

$$\varepsilon_i^{\tau \text{ ID}} = \frac{N_{\text{common+}\tau \text{ ID}, i}^{\text{data}} - N_{\text{common+}\tau \text{ ID}, i}^{\text{EWK+}\bar{t}\bar{t}}}{N_{\text{common}, i}^{\text{data}} - N_{\text{common}, i}^{\text{EWK+}\bar{t}\bar{t}}} \quad (8.4)$$

in the  $i$ th  $\tau$ -jet candidate  $p_T$  bin.

The transverse mass of the  $\tau$ -jet candidate and the  $E_T^{\text{miss}}$  was calculated for events passing the common selections and two of the factorized selections, namely the  $E_T^{\text{miss}}$  and  $\Delta\phi(\tau\text{-jet candidate})$  requirements. No b-tagged jet is required, however, since this requirement was found to have very little effect on the shape of the transverse mass distribution, while it would have the negative effect of reducing the number of events in the sample and thus increasing the sensitivity to statistical fluctuations.

Since no  $\tau$  identification has been performed, the  $\tau$ -jet candidate is used in the transverse mass calculation. If there are several  $\tau$ -jet candidates in the event, the most isolated one is used. The number of events in the  $j$ th bin of the transverse mass distribution is given by

$$N_j^{m_T} = \sum_i^{\tau\text{-jet candidate } p_T \text{ bins}} \left( N_{\text{common+}E_T^{\text{miss}}+\Delta\phi, ij}^{\text{data}} - N_{\text{common+}E_T^{\text{miss}}+\Delta\phi, ij}^{\text{EWK+}\bar{t}\bar{t}} \right) \varepsilon_i^{\tau \text{ ID}}. \quad (8.5)$$

The entire transverse mass distribution is normalized to the number of QCD multijet events calculated in Eq. (8.3).

### 8.2.3 Invariant mass distribution of QCD multijet events

The shape measurement of the invariant mass distribution proceeds like the transverse mass shape measurement, except that the b-tagging selection is made, i.e. at least one b-tagged jet is required. This is necessary, because the invariant mass reconstruction uses the

momentum of the b-jet in connection with a kinematical constraint for solving the neutrinos' longitudinal momentum component (as explained in Section 9.1.2).

The number of events in the  $j$ th bin of invariant mass is given by

$$N_j^m = \sum_i^{\tau\text{-jet candidate } p_T \text{ bins}} \left( N_{\text{common} + E_T^{\text{miss}} + \text{b-tag} + \Delta\phi, ij}^{\text{data}} - N_{\text{common} + E_T^{\text{miss}} + \text{b-tag} + \Delta\phi, ij}^{\text{EWK+}\bar{t}\bar{t}} \right) \varepsilon_i^{\tau \text{ ID}}. \quad (8.6)$$

As with the transverse mass, the invariant mass distribution is normalized to the number of QCD multijet events calculated in Eq. (8.3).

### 8.3 Electroweak and $t\bar{t}$ background without a genuine $\tau$

The background contribution from electroweak and  $t\bar{t}$  events without a genuine  $\tau$  lepton within the  $p_T, \eta$  acceptance is not determined from data but simulated. It was found to be small compared to the other contributions. The simulated processes are well understood theoretically and the  $\tau$ -jet misidentification rates for electrons, muons and hadronic jets in simulation agree with those measured in data [82].

## 9 Invariant mass reconstruction

Science is what we understand well enough to explain to a computer. Art is everything else we do.

Donald E. Knuth

The following definitions are used in the description of the kinematics and the invariant mass reconstruction algorithm.

**Reconstructed tau** The analysis selects hadronically decaying tau leptons. However, due to lepton number conservation, the decay of a tau lepton always produces a tau neutrino, which escapes the detector undetected and with unknown momentum. The terms *reconstructed tau* and  $\tau$ -jet always refer to the tau object that is reconstructed from those of its decay products that are detected, i.e. everything except the neutrino. The reconstructed tau is often simply denoted  $\tau$  in this section, as there is no danger of confusion with the generic notation for any tau lepton.

**Neutrino pair** The term *neutrino pair* refers to the combination of the neutrino produced in association with the charged tau lepton and the neutrino produced in the decay of the tau lepton. In the invariant mass reconstruction, these two actually distinct particles are treated as a single particle for all intents and purposes. Most importantly, their momentum four-vectors are summed up to a single one, denoted  $p_\nu$ . This resultant momentum is used in the invariant mass calculation. It should be noted that this is *not* an approximation, since the invariant mass in fact only depends on the sum of the two tau neutrinos' momenta. Expressions such as “neutrino momentum (vector)” always refer to the neutrino pair, unless stated otherwise. In formulæ, the notation for the neutrino pair is simply  $\nu$ , as there is no danger of confusion with the generic notation for any neutrino.

The concepts of reconstructed tau (or  $\tau$ -jet) and neutrino pair are illustrated in Fig. 9.1

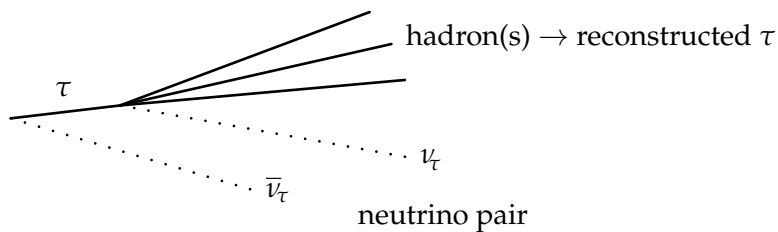


Figure 9.1: A sketch explaining the expressions *reconstructed tau* and *neutrino pair*. The neutrinos' paths are shown as dotted lines here to emphasize the fact that they go undetected.

**Associated b-jet** The term *associated b-jet* refers to the jet coming from the bottom quark produced in the decay of the same top quark as the tau lepton (the latter via an intermediate  $W$  or  $H^\pm$  boson). In other words, tau lepton and associated b-jet have the same parent top quark. The b-jet coming from the other top quark decay in the event will simply be referred to as the *other b-jet*.

This section contains several large tables, flowcharts, and collections of figures. For better organization, most of these are collected at the end of the section.

## 9.1 The idea behind the invariant mass reconstruction

The invariant mass of a system can be calculated if the resultant momentum vector of the center of mass of the system is known. This is possible if the momentum vectors of all the particles belonging to the system can be reconstructed. In the present case, where the system consists of a visible  $\tau$ -jet and two neutrinos, this is not the case, since the neutrinos go unobserved. In order to still reconstruct the invariant mass to some degree of accuracy, a method is applied that is based on two propositions.

**Proposition 1** The transverse momentum vector of the neutrino pair corresponds to the missing transverse energy vector of the event.

**Proposition 2** The longitudinal momentum of the neutrino pair, denoted  $p_{\nu}^z$ , can be calculated by using the mass of the parent top quark as a kinematical constraint. This is done by approximating the top quark's invariant mass by its known rest mass and using the conservation of four-momentum to solve for  $p_{\nu}^z$ .

Proposition 1 alone is enough to calculate the *transverse* mass of the tau-and-neutrino system, which has been used so far in the analysis to extract a possible signal. Proposition 2 is a new addition to this analysis.

### 9.1.1 Invariant mass of the top quark

Conservation of four-momentum gives the following equation for the invariant mass of the parent top quark of the tau-and-neutrino system:

$$m_t^2 = p_t^2 = (p_b + p_{\tau'} + p_{\nu'})^2, \quad (9.1)$$

where  $p_b$ ,  $p'_{\tau}$ , and  $p'_{\nu}$  are the four-momenta of the *associated* b-jet, the tau lepton, and the tau neutrino produced in the decay of the  $H^\pm$  or  $W$  boson, respectively. From an experimental point of view, it is useful to rewrite this equation replacing the sum of the momenta of the tau lepton and the tau neutrino with the sum of the momenta of the *reconstructed tau* and the *neutrino pair*,

$$p_{\tau'} + p_{\nu'} = p_{\tau}^{\text{visible}} + p_{\tau}^{\text{invisible}} + p_{\nu} = p^{\text{reconstructed } \tau} + p^{\text{neutrino pair}} \equiv p_{\tau} + p_{\nu}. \quad (9.2)$$

Using these, Eq. (9.1) becomes

$$m_t^2 = (p_b + p_{\tau} + p_{\nu})^2. \quad (9.3)$$

### 9.1.2 Longitudinal momentum of the neutrino pair

Assuming that the invariant mass of the top quark is very close to its rest mass in most events, i.e. setting  $m_t = M_t$ , the only unknown quantity in this equation is the longitudinal momentum of the neutrino pair,  $p_{\nu}^z$ . The assumption  $m_t = M_t$  is equivalent to assuming that the top quarks are on-shell. Using this assumption, expanding the right hand side

of Eq. (9.3), and simplifying the result yields a second-order equation for the longitudinal momentum of the neutrino pair,

$$(1 - B^2) (p_\nu^z)^2 - 2ABp_\nu^z + (p_\nu^T)^2 - A^2 = 0, \quad (9.4)$$

where

$$A = \frac{1}{E_b + E_\tau} \left[ \frac{1}{2} (M_t^2 - M_\tau^2 - M_b^2) - E_b E_\tau + \mathbf{p}_b \cdot \mathbf{p}_\tau + \vec{p}_\nu^T \cdot (\vec{p}_b^T + \vec{p}_\tau^T) \right], \quad (9.5)$$

$$B = \frac{p_b^z + p_\tau^z}{E_b + E_\tau}. \quad (9.6)$$

It has the solutions

$$p_\nu^z = \frac{1}{1 - B^2} \left[ AB \pm \sqrt{A^2 - (p_\nu^T)^2 (1 - B^2)} \right]. \quad (9.7)$$

For convenience, the quantity in the square root is denoted

$$D = A^2 - (p_\nu^T)^2 (1 - B^2). \quad (9.8)$$

$D$  is the *discriminant* of the second-order equation for  $k_z$ , Eq. (9.4). It determines what kind of solutions the equation has. The three distinct cases are:

- $D > 0$  : two real solutions,
- $D = 0$  : one real solution,
- $D < 0$  : two complex (unphysical) solutions.

Immediately we see that we will run into trouble if we encounter a negative discriminant in a calculation using the experimentally measured momenta. It will give rise to complex momenta which we do not know how to interpret and thus must consider unphysical. Because of this property, the discriminant will play a key role in the invariant mass reconstruction.

Using the discriminant defined above, the neutrino pair's longitudinal momentum can be expressed as

$$(p_\nu^z)^\pm = \frac{AB \pm \sqrt{D}}{1 - B^2}. \quad (9.9)$$

### 9.1.3 A tale of two solutions

If the discriminant  $D$  in Eq. (9.9) is positive, there will only be real solutions. The trouble is, however, that there will be *two* such solutions, unless the discriminant happens to be exactly zero within the numerical uncertainty. Only one solution is desired, and this solution should give the correct invariant mass of the tau-and-neutrino system,  $m(\tau, \nu)$ . The questions arise: *why are there two distinct solutions and do the two solutions give the same invariant mass  $m(\tau, \nu)$ ?* The answers are as follows. As a second-order equation of  $k_z$ , Eq. (9.1) is in general expected to have two possible solutions. Specifically, this is the case because the quantity  $E_t^2 - (p_t^z)^2$  entering the definition of the top quark invariant mass has the same value for two different  $p_\nu^z$  in general. The two possible solutions do not give the same tau-and-neutrino system invariant mass, because  $m(\tau, \nu)$  depends on  $p_\nu^z$  through the expression  $E_B^2 - (p_B^z)^2$ , where  $B$  stands for a  $H^\pm$  or  $W$  boson. This expression is not generally equal for the two solutions. So even if the top quark's invariant mass is independent of which one is chosen, the tau-and-neutrino invariant mass is *not*.

## 9.2 Invariant mass reconstruction algorithm

The structure of the invariant mass reconstruction algorithm is visualized in the flowchart in Fig. 9.4. The details of how the algorithm proceeds are described in the following text. The different assumptions and criteria for resolving ambiguities that arise in the calculation are presented without motivation or explanation at this point, they are discussed in the following sections.

The invariant mass reconstruction is performed for all events that pass the event selection described in Section 7. The algorithm's input are the momenta of the tau lepton and all b-tagged jets, as well as the  $\tilde{E}_T^{\text{miss}}$  in the event. The value  $M_t = 172.5 \text{ GeV}$  is used for the top quark rest mass, because it corresponds to the value used in the event simulation. It differs by less than 1% from current world average value ( $M_t^{\text{PDG2012}} = 173.5 \pm 0.6 \pm 0.8 \text{ GeV}$  [1]), which is a negligible deviation compared to the experimental uncertainties in the calculation.

If there are several b-tagged jets in the event, the first step is to select one as the associated b-jet. To do this, the b-jet that has the smaller distance  $\Delta R(\text{b-jet}, \tau\text{-jet})$  in  $\eta\text{-}\phi$  space from the reconstructed tau lepton is selected.

With the choice of associated b-jet made, all momenta required for the first calculation steps are specified unambiguously. The discriminant of the  $p_\nu^z$  solutions is calculated using Eq. (9.8).

If the discriminant is positive, there are two possible  $p_\nu^z$  solutions, which are both calculated. Using the two solutions, the two possible neutrino momentum vectors are constructed and the pseudorapidity difference between the reconstructed tau and the neutrino pair,  $\Delta\eta \equiv |\eta_\tau - \eta_\nu|$ , is calculated for each solution. The solution that maximizes  $\Delta\eta$  is selected. The corresponding invariant mass of the tau-neutrino system is calculated.

If the discriminant is negative, the invariant mass calculation becomes less straightforward and extra steps must be taken to handle the negative discriminant gracefully. First, the discriminant  $D$  is set equal to zero and the resulting single  $p_\nu^z$  solution is calculated. Then, to remedy the fact that the discriminant was forced to zero, the  $\tilde{E}_T^{\text{miss}}$  is modified in the following way. Its direction  $\phi$  is kept unchanged, but it is given a new norm  $E_T^{\text{miss}}$  calculated from the requirement  $D = 0$ , which leads to a quadratic equation for  $E_T^{\text{miss}}$  with two real solutions given in Eq. (9.12) below. The invariant mass of the top quark,  $m_t$ , is calculated using each of the  $E_T^{\text{miss}}$  solutions and the  $p_\nu^z$  solution. The two computed values are compared to its rest mass  $M_t = 172.5 \text{ GeV}$ . If neither of the top quark invariant mass solutions falls within a certain allowed range centered around  $M_t$ , the event is rejected. Different allowed ranges have been tried (Section 9.5.3).

If the event passes the  $m_t$  selection, the  $E_T^{\text{miss}}$  solution corresponding to whichever invariant mass  $m_t$  is closer to the rest mass  $M_t$  is selected. Finally, the invariant mass of the tau-neutrino system is calculated using the  $p_\nu^z$  solution and the selected  $E_T^{\text{miss}}$  solution.

The remaining possible case is the one where the discriminant is exactly zero within the numerical precision. Then the two possible  $p_\nu^z$  solutions coincide. This case has not been described above for the sole reason that it is extremely unlikely to occur. If it still does, the algorithm is capable of handling it, following the same procedure as for a positive non-zero discriminant. The only distinction is that it makes no difference, which of the two (equal)  $p_\nu^z$  solutions is selected.

## 9.3 Conditions for reliable invariant mass reconstruction

### 9.3.1 Validity of using the top mass as a kinematical constraint

The calculation of the longitudinal momentum of the neutrino pair is based on using the mass of their parent top quark as a kinematical constraint. This method relies on the assumption that the top quarks in  $t\bar{t}$  events are usually close to being on-shell, i.e.  $m_t \approx M_t$ . This assumption was verified by calculating the top quark invariant mass in simulated events. The distribution is shown for one signal sample in Fig. 9.2, it is similar for all background samples as well. The distribution was found to follow the shape of a Breit-Wigner function with width  $\Gamma_t \sim 2$  GeV, in accordance with the experimentally measured value of the natural width of the top quark [1]. The spread of the  $m_t$  distribution is thus small compared to the experimental uncertainties. While the effect of a finite width may need to be taken into account as a systematic uncertainty in a possible future analysis using the invariant mass distribution for signal extraction, the approximation of  $m_t \approx M_t$  is considered adequate.

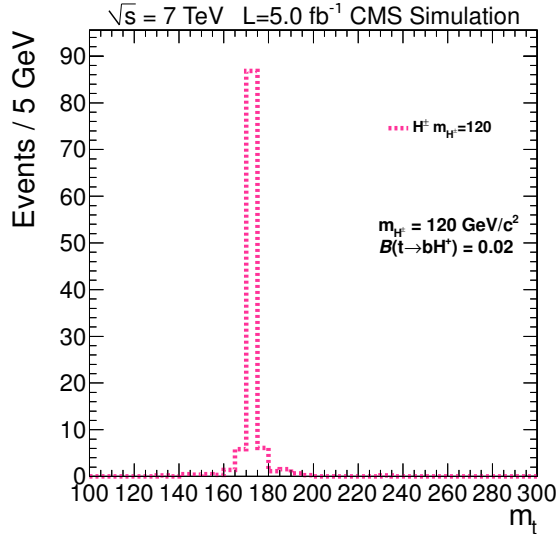


Figure 9.2: True top quark invariant mass in simulated events.

### 9.3.2 Experimental requirements

In order for the invariant mass reconstruction using the algorithm described above to yield physically sensible results, the selected events should satisfy the following requirements.

1. The tau lepton is genuine and its momentum vector measured accurately.
2. The identified associated b-jet is genuine (correctly identified as coming from a b quark) and its momentum vector measured accurately.
3. The correct b-tagged jet in the event is selected as the associated b-jet.
4. There is a good correspondence between the reconstructed  $\vec{E}_T^{\text{miss}}$  and the transverse momentum of the neutrino pair.

The word *accurate* above is meant to be understood in the sense that it conveys in statistics, namely *reflecting the true value well*.

It was studied quantitatively how well the above requirements are satisfied in the selected events. This was done using simulated events, for which not only the reconstructed information, but also the underlying truth is known. The following criteria were applied to find out in what fraction of selected events each of the requirements was satisfied. Their numbers (1–4) correspond to those in list of requirements above.

1. The tau lepton identification and measured momentum are considered good if a true  $\tau$  is found within  $\Delta R < 0.1$  of the reconstructed  $\tau$  and the magnitudes of their respective momenta do not differ by more than  $\pm 15$  GeV
2. The b-jet identification and measured momentum are considered good if a true b quark is found within  $\Delta R < 0.6$  of the reconstructed associated b-jet and the magnitudes of their respective momenta do not differ by more than  $\pm 15$  GeV
3. The selection of the associated b-jet is considered successful if the true b quark it corresponds to comes from the same top quark as the true  $\tau$  lepton. Note that we require these true particles to exist in the two above steps. If either of them is not found, i.e. the criteria in 1. and 2. are not met, it follows automatically that the selection of the associated b-jet failed. This means that while the first two tests are independent, this third one depends on both of them.
4. The correspondence between the  $\vec{E}_T^{\text{miss}}$  and  $\vec{p}_\nu^T$  is considered good if the direction  $\phi$  and absolute value  $E_T^{\text{miss}}$  of the former are within  $\pm 15^\circ$  and  $-40$  to  $+60$  GeV of the values for the true transverse momentum of the neutrino pair. The asymmetric range for the absolute value was chosen because a systematic shift of the  $\vec{E}_T^{\text{miss}}$  of about  $+10$  GeV with respect to  $\vec{p}_\nu^T$  was found. If an event has a negative discriminant and a new  $E_T^{\text{miss}}$  is therefore calculated, the old experimentally measured value is still used in the event classification.

The flowchart in Fig. 9.5 visualizes how the tests proceed and shows the possible negative outcomes, where something was misidentified or mismeasured. The positive outcomes (corresponding to good identification etc.) are referred to as *classes*, into which the events are classified. They are shown in Table 9.3, along with the fraction of events assigned to each class. The table shows that no single misidentification or mismeasurement occurs in such a large fraction of events that it will challenge the consistency of the invariant mass reconstruction. On the other hand, some misidentification or mismeasurement occurred in almost half of the events, so smearing of the invariant mass distribution is expected. Background events without genuine top quarks,  $\tau$  leptons, or b-jets can only pass the event selection because of misidentification and so have to be excluded from the previous statements, though their presence does not challenge the consistency of the invariant mass reconstruction more than it challenges the consistency of any other mass variable reconstruction. They simply are a nuisance that needs to be taken into account and studied in the analysis, regardless of whether the transverse or invariant mass is used for signal extraction.

## 9.4 Selecting the better $p_\nu^z$ solution

If the discriminant  $D$  in Eq. (9.9) is positive, there are two possible  $p_\nu^z$  solutions. The question arises, which one should be used to calculate the invariant mass of tau-and-neutrino

system. Whereas both lead exactly to the same top quark invariant mass (172.5 GeV) by construction, they do not lead to the same invariant mass of the tau-and-neutrino system.

In simulated events is it possible to say, which calculated solution was closer to the true value. We define the *better*  $p_\nu^z$  solution to mean either of the following two things, depending on whether the simulated event contains a  $H^\pm$  boson (signal) or not (background). For *signal* events, the better solution is the one giving the  $H^\pm$  invariant mass solution closer to the  $H^\pm$  rest mass. This is assessed simply by calculating the  $H^\pm$  invariant mass for each solution and comparing the obtained values to the rest mass. For *background* events, the better solution is the one that is closer to the true  $p_\nu^z$  of the neutrino pair.

Figs. 9.6 and 9.7 show the invariant mass distributions that are obtained when using the better and the worse  $p_\nu^z$  solution, respectively. Only events with a positive discriminant are included, as only they have two possible  $p_\nu^z$  solutions. The different plots in each figure correspond to different  $H^\pm$  masses, given in the legend and indicated by a dashed vertical line. The figures show that the distributions are quite different for the two cases. It can therefore be expected that the quality of the final results (signal significances, exclusion limits, ...) that can be obtained depends crucially on the ability to select the better solution at least in most of the events.

Since the author could not think of a way to identify the better  $p_\nu^z$  solution based on first principles and physical arguments, a method for finding it by trial and error was required. Selection methods using different observables (angles, momenta, ...) in the event were invented. The observables were chosen on the basis that they were thought to *possibly* provide some discriminating power in the  $p_\nu^z$  solution selection. To keep the methods simple, each uses only a single observable.

The investigated solution selection methods were the following (the expression in parentheses is a short, descriptive name). Select the  $p_\nu^z$  solution that...

1. ...has the **greater absolute value** ( $\max-|p_\nu^z|$ ),
2. ...has the **smaller absolute value** ( $\min-|p_\nu^z|$ ),
3. ...leads to the **greater angle**, which we call  $\xi$ , between the reconstructed tau lepton and the neutrino pair ( $\max-\xi$ ), where the  $\xi$  is calculated in three-dimensional space as

$$\xi = \arccos \left( \frac{\mathbf{p}_\tau \cdot \mathbf{p}_\nu}{|\mathbf{p}_\tau| |\mathbf{p}_\nu|} \right). \quad (9.10)$$

The smallest positive solution of is taken, so that  $\xi \in [0, \pi]$ .

4. ...leads to the **smaller angle**  $\xi$  (calculated as in 3.) between the reconstructed tau lepton and the neutrino pair ( $\min-\xi$ ),
5. ...leads to the **greater pseudorapidity difference**  $\Delta\eta \equiv |\eta_\tau - \eta_\nu|$  between the reconstructed tau lepton and the neutrino pair ( $\max-\Delta\eta$ ),
6. ...leads to the **smaller pseudorapidity difference** (calculated as in 5.) between the reconstructed tau lepton and the neutrino pair ( $\min-\Delta\eta$ ).

Criterion 1 (3, 5) is the complement of criterion 2 (4, 6), so that they are mutually exclusive and will always lead to choosing different solutions.

Simulated event samples were used to find out, which method gives the better solution most often. The results for the different signal and background samples are shown in Table

9.1. For a good overview, the same information is also shown Fig. 9.3.

Which selection method is the best for the signal depends on the  $H^\pm$  mass. For  $M_{H^\pm} \geq 120$  GeV, the max- $\Delta\eta$  method is most likely to give the better solution. On the other hand, for  $M_{H^\pm} \leq 100$  GeV, it is the min- $\Delta\eta$  method that gives the better solution most often. So interestingly, the behaviour is opposite for the light and heavy ends of the studied  $H^\pm$  mass range! For the background, the smaller  $p_\nu^z$  solution is always the one that is closer to the true  $p_\nu^z$  value. This means that the min- $|p_\nu^z|$  selection method is ideal for the background events.

In the presented analysis, the  $p_\nu^z$  solution was selected using the max- $\Delta\eta$  method, because it identifies the better solution in simulated  $H^\pm$  signal samples over most of the  $H^\pm$  mass range. Invariant mass distributions obtained using each of the different methods are shown in Appendix B.

$M_{H^\pm}$ (GeV) or background sample	Selection method					
	max- $ p_\nu^z $	min- $ p_\nu^z $	max- $\xi$	min- $\xi$	max- $\Delta\eta$	min- $\Delta\eta$
80	46	54	42	58	29	71
90	51	49	47	53	33	67
100	49	51	57	43	42	58
120	58	42	64	36	67	33
140	52	48	65	35	82	18
150	52	48	62	38	95	5
155	47	53	73	27	96	4
160	47	53	70	30	100	0
W+jets	0	100	70	30	53	47
t̄t	0	100	65	35	46	54
Z/γ*	0	100	78	22	25	75
Single top	0	100	63	37	49	51
Diboson	0	100	70	30	44	56

Table 9.1: Fractions of better  $p_\nu^z$  solution selections for each of the simulated datasets and methods. All fractions are in percent and rounded to the nearest integer percentage. The largest achieved fraction for each dataset is highlighted.

## 9.5 Negative discriminants: the problem and its solution

In addition to the problem of selecting the better  $p_\nu^z$  solution, the greatest challenge in the algorithm development is the handling of events in which the discriminant is negative. There are no real and therefore no physical  $p_\nu^z$  solutions in such a case.

If a negative discriminant only occurred in a small fraction of events, such events might simply be discarded without much loss of information. Or, if the discriminant only ever were slightly negative, very close to zero, it could perhaps be set to zero and the negativity be regarded as a minor effect due to measurement uncertainty. Unfortunately, neither of the two is true. As can be seen in Fig. 9.8 showing the distributions of discriminants, negative discriminants occur in a large fraction (roughly half) of events and can have a large absolute

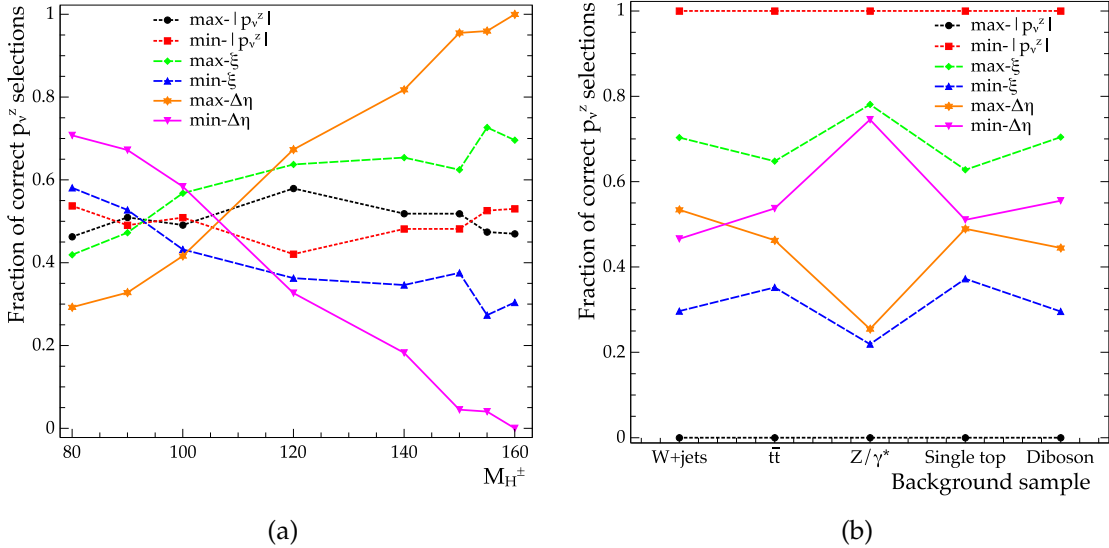


Figure 9.3: The fraction of background events in which the better  $p_v^z$  solution was selected using each of the different methods for each  $M_{H^\pm}$  value (a) and each simulated background sample (b).

value. It follows that discarding all events with a negative discriminant means losing a lot of data and setting the discriminant to zero constitutes a hardly justifiable unphysical manipulation of the data. A better way of handling such events is required. While a negative discriminant might be the consequence of mismeasurement or misidentification, rejecting events with a negative discriminant does not greatly improve the signal-to-background ratio.

Fig. 9.9 shows the distribution of discriminants obtained using the true momenta of all particles. This corresponds to observing the event with a hypothetical ideal detector. Even in such a case there is a small fraction of negative discriminants, which are caused by the approximation of the top quark invariant mass by its rest mass in the calculation of  $p_v^z$ . If the actual invariant mass of the top quark were used, the discriminant would never be negative.

### 9.5.1 What causes a negative discriminant?

It was just stated that the on-shellness assumption for the top quark can cause a negative discriminant, but it is clear from Figure 9.9 that this effect is very small and can not account for the observed large fraction of negative discriminants. We can expect experimental limitations to play a much more important role.

From the definition of the discriminant, Eq. (9.8), the following condition for the discriminant to be positive can be derived:

$$\left[ \frac{1}{2}(M_t^2 - M_b^2 - M_\tau^2) - E_b E_\tau + \mathbf{p}_b \cdot \mathbf{p}_\tau + p_v^T (p_b^T \cos \phi_{bv} + p_\tau^T \cos \phi_{tv}) \right]^2 > (p_v^T)^2 \left( (E_b + E_\tau)^2 - (p_b^z + p_\tau^z)^2 \right). \quad (9.11)$$

Both sides of Eq. (9.11) are non-negative: the left hand side is the square of a real number,

while the right hand side is non-negative because (clearly)  $(p_\nu^T)^2 \geq 0$  and  $E_b > p_b^z; E_\tau > p_\tau^z$ , so the expression in parentheses is non-negative.

As  $\vec{p}_\nu^T$  cannot be measured experimentally, it is replaced by the missing transverse energy,  $\vec{p}_\nu^T \leftarrow \vec{E}_T^{\text{miss}}$ . So the right hand side of Eq. (9.11) is proportional to  $(E_T^{\text{miss}})^2$  and should be smaller than the left hand side, which only contains one term proportional to  $E_T^{\text{miss}}$ . The left hand side also contains the angles  $\phi_{bv}$  and  $\phi_{\tau v}$ , which are experimentally determined as the angle between the missing transverse momentum vector  $\vec{E}_T^{\text{miss}}$  and the  $\mathbf{p}_T$  of the b-jet and the reconstructed  $\tau$ , respectively. It becomes clear that the sign of the discriminant is sensitive to the  $\vec{E}_T^{\text{miss}}$ . Unfortunately, the missing energy measurement comes with a considerable experimental uncertainty, and approximating the neutrino pair's transverse momentum with the  $\vec{E}_T^{\text{miss}}$  cannot be considered a very reliable approximation. Fig. 9.10 shows the discriminant distribution calculated using the true momenta for the b-jet and the visible decay products of the tau, while the transverse momentum of the neutrino pair has been replaced with the true  $\vec{E}_T^{\text{miss}}$ , calculated from all the neutrinos in the event. It can be seen that even this slight modification to the missing transverse momentum causes the fraction of negative discriminants to grow noticeably, especially for lower  $H^\pm$  masses. And experimental imperfections influencing the  $\vec{E}_T^{\text{miss}}$  measurement have not even been included. In conclusion, we consider the deviation of the measured transverse momentum vector from the true transverse momentum of the neutrino pair to be the most likely cause of most negative discriminants.

### 9.5.2 Recovering events with negative discriminants

The approach we have taken to handle events with negative discriminants has been adapted from Ref. [101], where it is used in a similar context in searches for new heavy gauge bosons ( $W'$ ). It has been slightly modified here to be applicable to the different kinematical configuration in our analysis.

The idea is to set a negative discriminant to zero in the calculation of the  $p_\nu^z$  solution, which is compensated for by giving the  $E_T^{\text{miss}}$  a new absolute value that is calculated from the requirement that the discriminant be zero. The latter step is to remedy the unphysical forcing to zero of the discriminant by finding a physically possible configuration that would give such a result. Modifying the  $E_T^{\text{miss}}$  derives justification from the fact that the poor correspondence between the measured  $\vec{E}_T^{\text{miss}}$  and the transverse momentum of the neutrino pair has been identified as probably being the frequent cause for a negative discriminant, as was discussed in Section 9.5.1.

The new  $E_T^{\text{miss}}$  solutions are obtained by setting  $D = 0$  in Eq. (9.8) and solving for  $E_T^{\text{miss}}$ . Since the equation is quadratic in  $E_T^{\text{miss}}$ , there are two solutions,

$$\text{new } E_T^{\text{miss}} = \frac{-\frac{1}{2}(M_t^2 - M_b^2 - M_\tau^2) + E_b E_\tau - \mathbf{p}_b \cdot \mathbf{p}_\tau}{p_b^T \cos \phi_{bv} + p_\tau^T \cos \phi_{\tau v} \pm \sqrt{(E_b + E_\tau)^2 - (p_b^z + p_\tau^z)^2}}. \quad (9.12)$$

The solutions are always real, since  $(E_b + E_\tau)^2 - (p_b^z + p_\tau^z)^2 \geq 0$ , as was shown in Section 9.5.1. The top quark invariant mass  $m_t$  is calculated using each of the  $E_T^{\text{miss}}$  solutions and the one giving a value closer to  $M_t = 172.5$  GeV is selected.

We acknowledge that this way of handling events with negative discriminants has the major flaw that it replaces a previously reconstructed quantity with a calculated one and that

it is not based on the application of fundamental physical principles (such as conservation laws). However, to the extent that it has been tested, it *works*, in the sense that it leads to physically sensible invariant mass distributions. Nevertheless, it is the weakest point of the presented invariant mass reconstruction method.

### 9.5.3 Top quark invariant mass selection

If the discriminant is positive, the invariant mass of the top quark will always be  $m_t = 172.5 \text{ GeV}$  by construction, since this is the original assumption used to solve  $p_\nu^z$ . However, if the discriminant is negative and the event recovered as described in Section 9.5.2, this is *not* the case. In general,  $m_t$  will differ from 172.5 GeV in such a case.

In order to keep the results physically meaningful, only events with  $m_t$  within a certain range centered around the top quark's rest mass are selected. The rationale behind this is that events in which the top quark is very much off-shell occur only with very small probability. In addition to this physical motivation, the selection might improve signal sensitivity by leading to sharper invariant mass peaks.

Different allowed ranges for  $m_t$  are tested and final results calculated for each. This way, the range giving the greatest signal sensitivity can be determined. The definitions of the different  $m_t$  selection scenarios are shown in Table 9.2.

Scenario name	Allowed $m_t$ range (GeV)	Allowed deviation from $M_t$ (GeV, approximate)
None	$0\text{--}\infty$	$-170 \text{ to } +\infty$
Loose	$100\text{--}240$	$\pm 70$
Medium	$140\text{--}200$	$\pm 30$
Tight	$157\text{--}187$	$\pm 15$

Table 9.2: Top quark invariant mass selection scenarios. The *tight* range is centered around an invariant mass value of 172 GeV, the *medium* and *loose* ranges around 170 GeV. This is to improve readability of the numbers; at masses noticeably different from the top quark rest mass, differences of a few GeV are not important.

The fractions of events with positive and negative discriminants as well as the total fraction of accepted events for each different  $m_t$  selection scenario are shown in Table 9.4.

## 9.6 Invariant mass distributions

The distributions of the invariant mass of the tau-and-neutrino system obtained using the algorithm described above are shown here. Events originally having a negative discriminant that were recovered using the method presented in Section 9.5.2 are included. The resulting distributions using the max- $\Delta\eta$  method for selecting the  $p_\nu^z$  solution (Section 9.4) in the case of ambiguity are shown in Figures 9.11 to 9.14 for the different top quark invariant mass ( $m_t$ ) selection scenarios. These are the final distributions used to obtain the limits on the signal branching ratio.

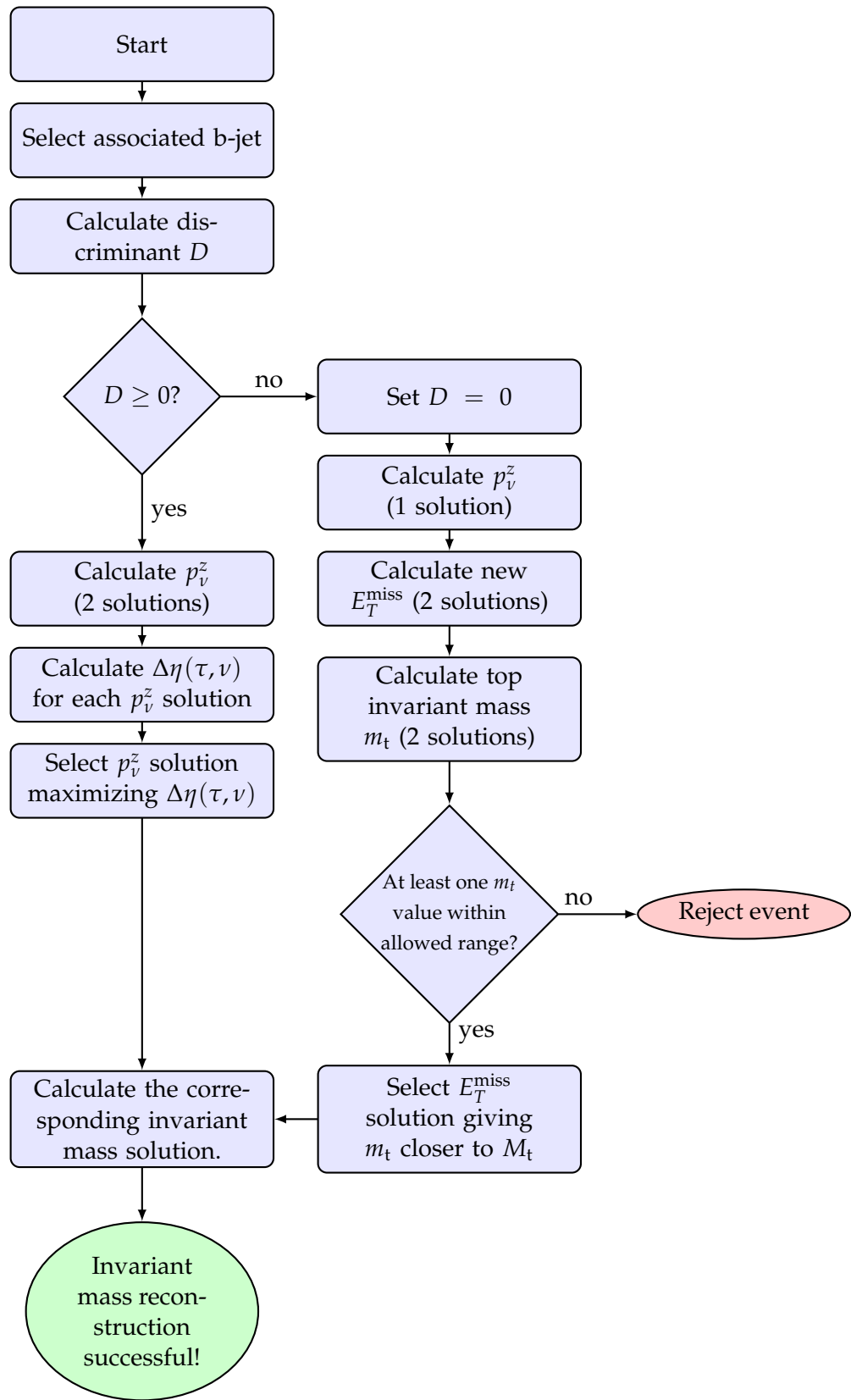


Figure 9.4: Flowchart of the invariant mass reconstruction algorithm.

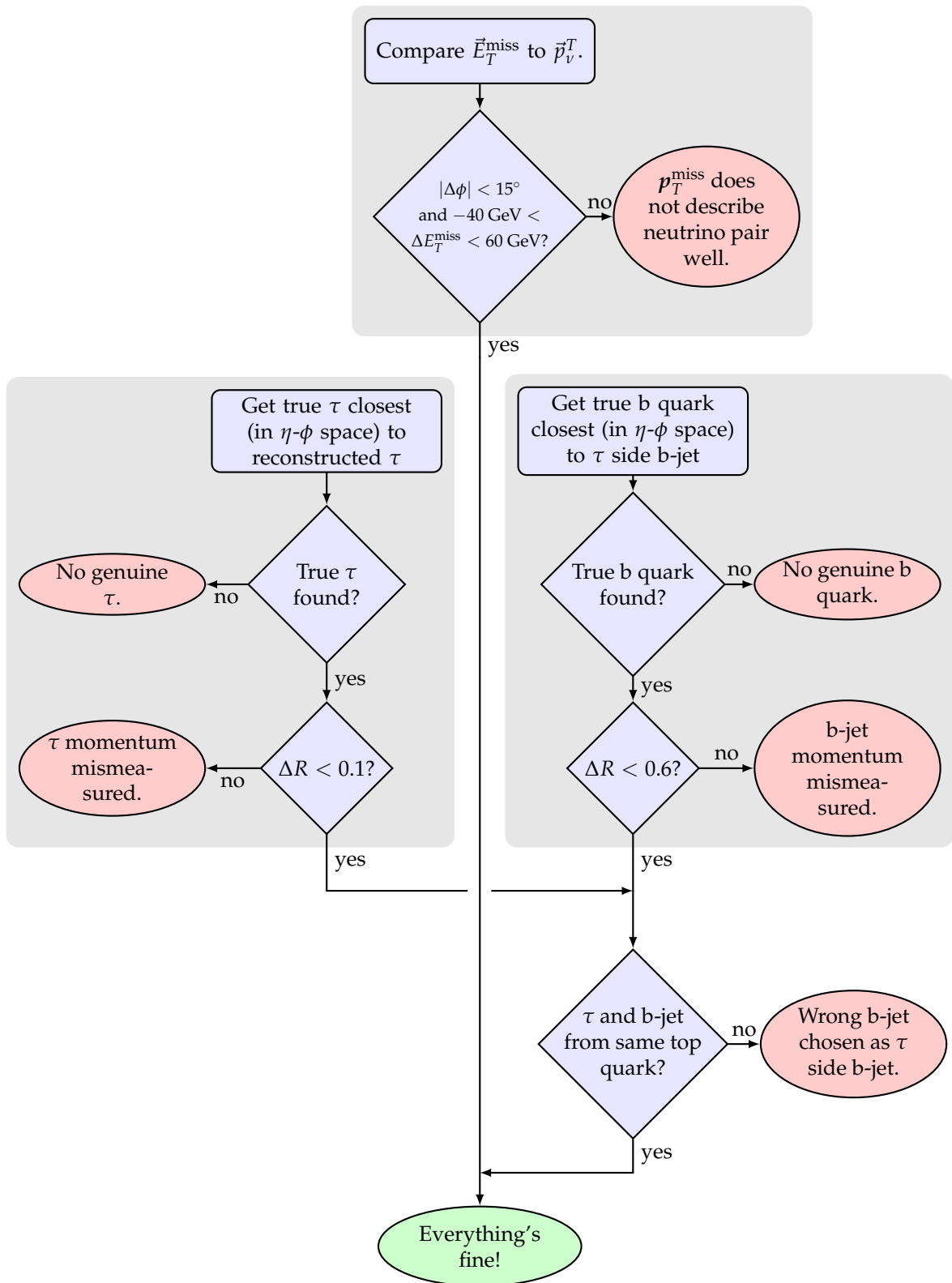


Figure 9.5: A graphic representation of the event classification steps. Where an arrowhead touches another arrow, it means that the conditions for both arrows have to be fulfilled to move on. (One can imagine a logic AND gate at such points.)

Event class	Signal dataset $M_{H^\pm}$ (GeV)						Background dataset						
	80	90	100	120	140	150	155	160	W+jets	t\bar{t}	Z/\gamma^*	Single top	Diboson
$\tau$ genuine	100	100	100	100	100	100	100	100	97	96	100	96	100
$\tau$ momentum good	100	100	99	99	100	100	100	100	96	91	100	94	96
Associated b-jet from genuine b quark	100	100	100	100	100	100	100	100	56	100	60	100	53
Associated b-jet momentum good	97	97	97	97	95	95	96	94	49	96	42	96	49
Associated b-jet chosen correctly	72	68	73	73	72	73	73	74	0	72	0	35	0
$\vec{E}_T^{\text{miss}} \approx \vec{p}_\nu^T$	82	82	84	79	82	81	85	83	86	85	80	83	89
Pure	55	53	59	56	57	55	62	57	0	59	0	26	0
Some misidentification	45	47	41	44	43	45	38	43	100	41	100	74	100

Table 9.3: Fractions of events belonging to the different classes. All fractions are expressed in percent and rounded to the nearest integer percentage. In background events without genuine top quarks (W+jets, Z/ $\gamma^*$ , diboson), a genuine associated b-jet does not exist and the choice is therefore never correct. Since a reliable simulation of the QCD multijet background was not feasible, results for this background are not included.

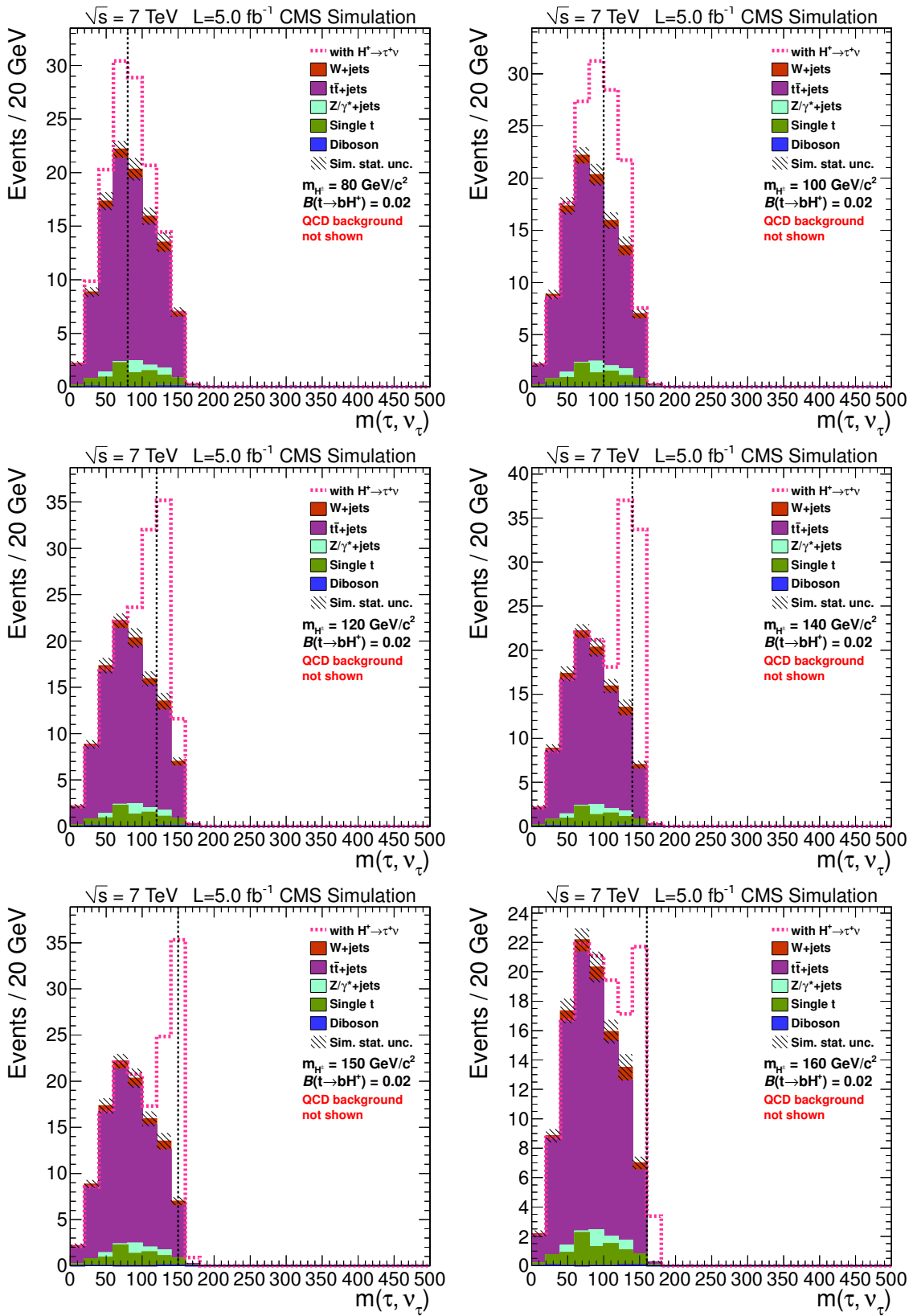


Figure 9.6: Invariant mass distributions calculated using the *better*  $p_v^z$  solution.

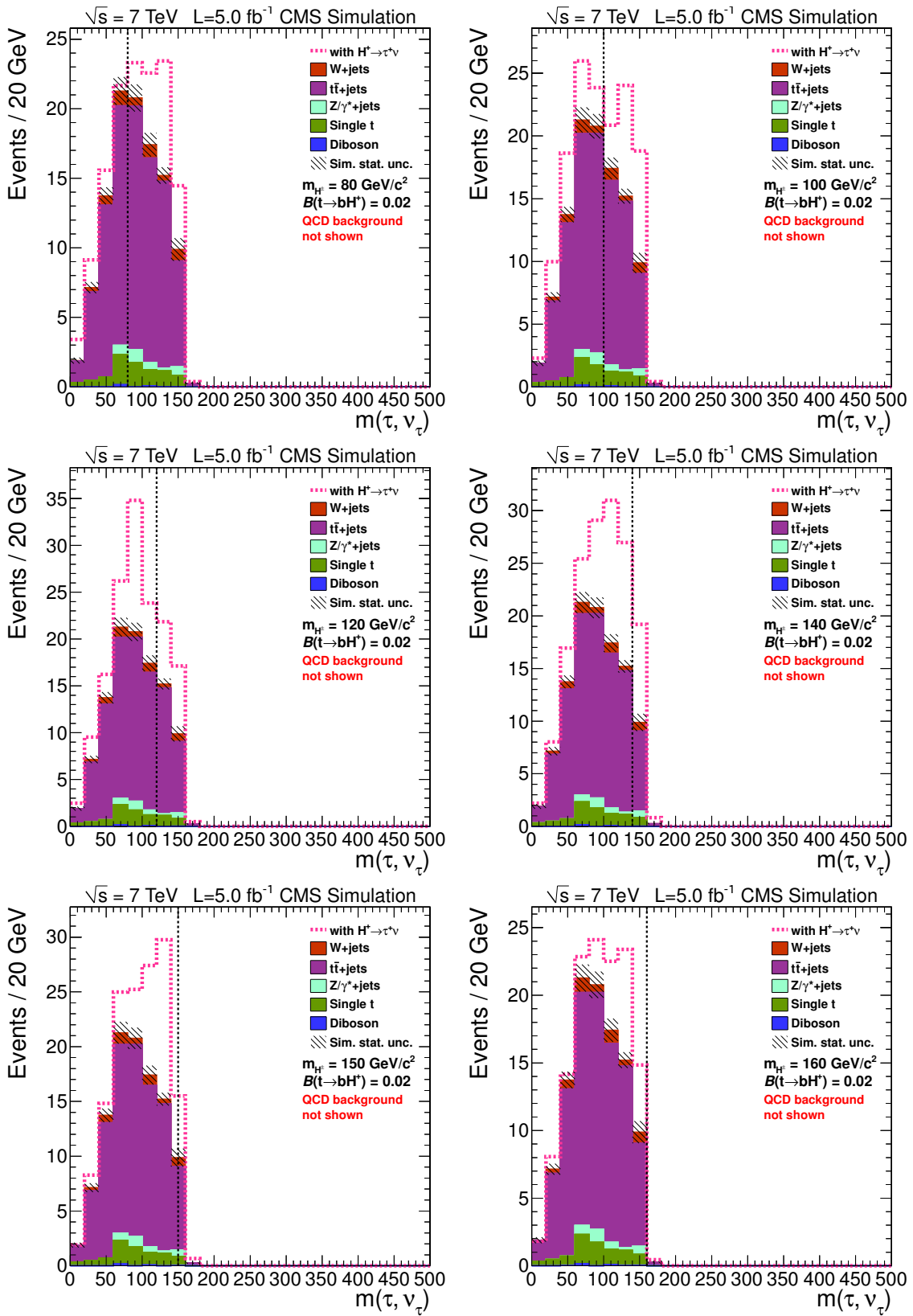


Figure 9.7: Invariant mass distributions calculated using the *wrong*  $p_\nu^z$  solution.

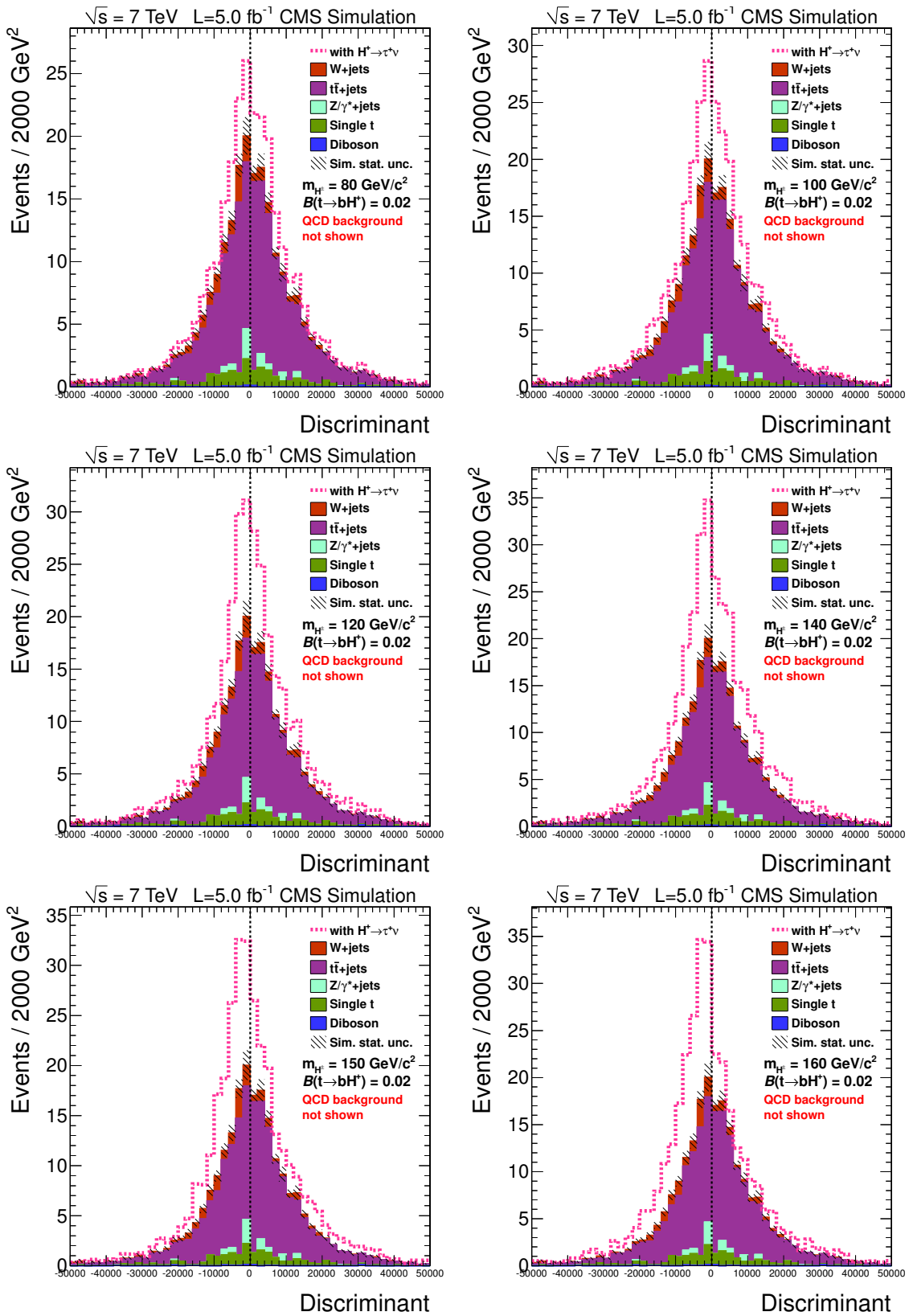


Figure 9.8: Distribution of discriminants of the invariant mass calculation.

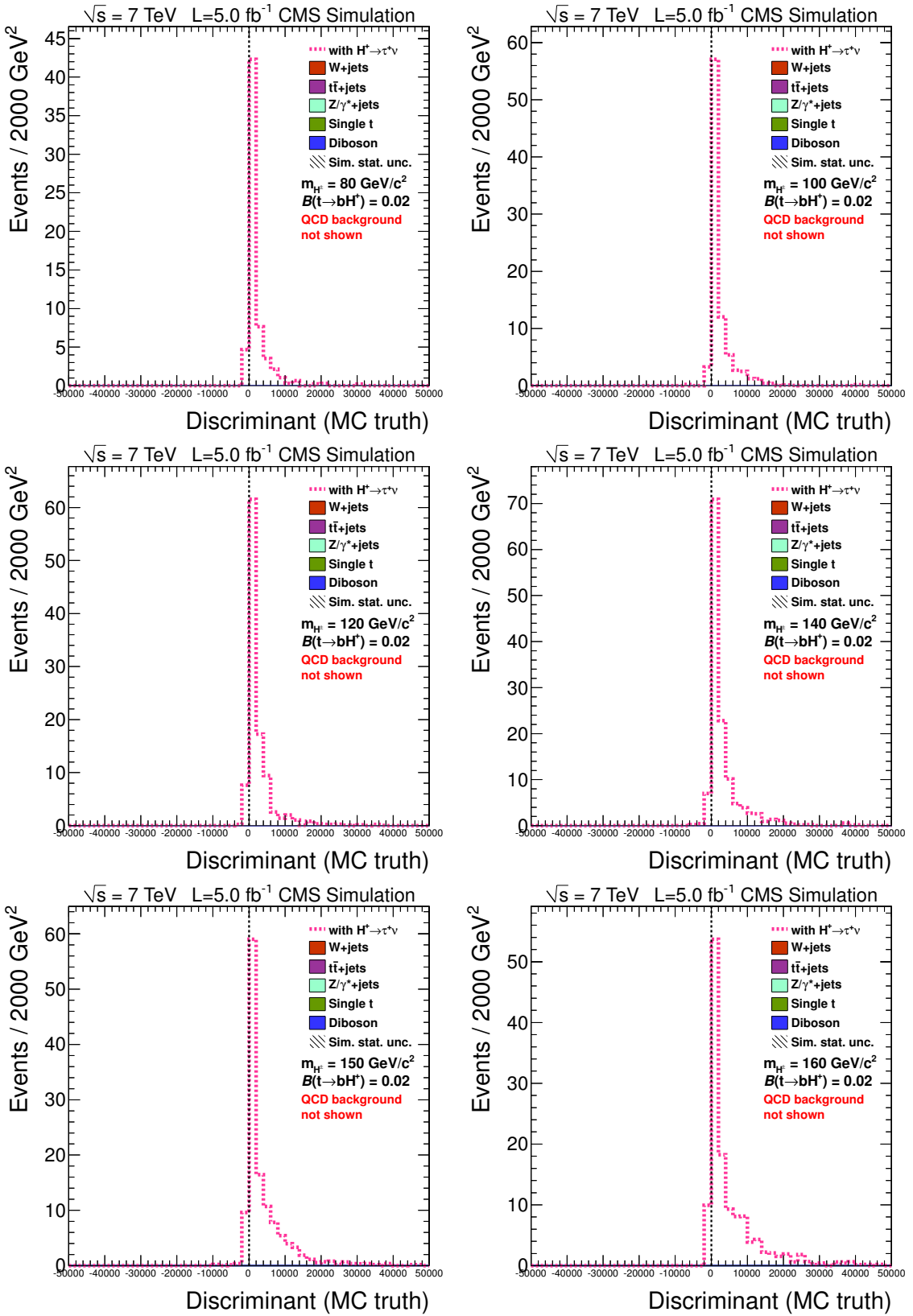


Figure 9.9: Distribution of discriminants in simulated signal events calculated using the true particle momenta.

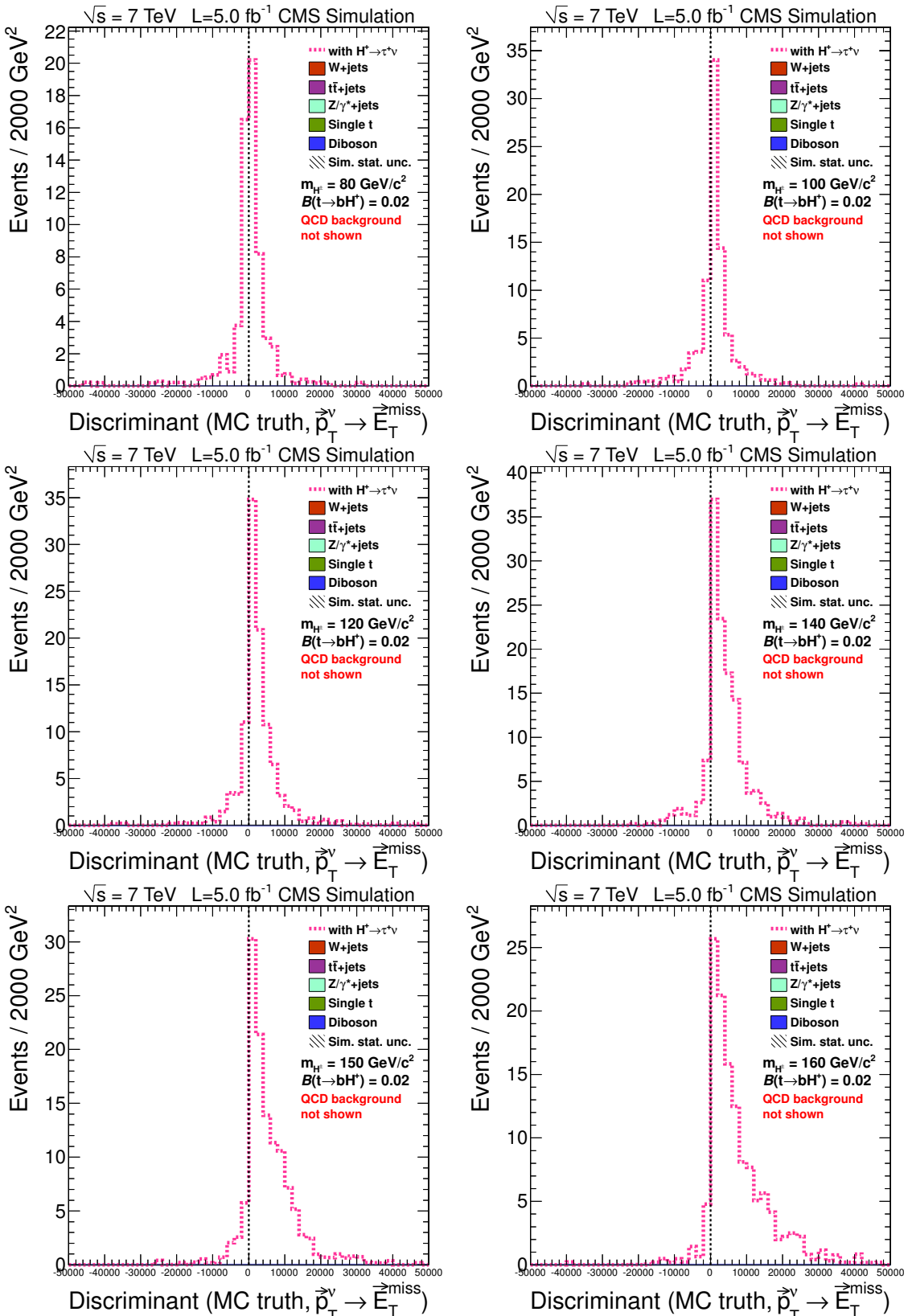


Figure 9.10: Distribution of discriminants in simulated signal events calculated using the true particle momenta, but replacing the transverse momentum vector of the neutrino pair with the true  $\vec{E}_T^{\text{miss}}$  calculated as the transverse momentum vector of *all* the neutrinos in the simulated event.

Event class	Signal dataset $M_{H^\pm}$ (GeV)						Background dataset						
	80	90	100	120	140	150	155	160	W+jets	t\bar{t}	Z/\gamma^*	Single top	Diboson
Positive discriminant	49	49	49	45	44	37	35	25	30	54	38	44	40
Negative discriminant	51	51	51	55	56	63	65	75	71	46	60	55	60
Pass loose $m_t$ selection	64	71	68	70	65	57	54	50	39	68	71	57	54
Pass medium $m_t$ selection	55	59	56	58	53	45	43	34	31	59	69	51	36
Pass tight $m_t$ selection	51	54	51	52	48	39	37	29	27	56	60	49	36

Table 9.4: Classification of simulated events by the discriminant and the success of recovery in the case of a negative discriminant. All values in percent and rounded to the nearest percent point. If no  $m_t$  selection is applied (*none* scenario), the fraction of passing events is always 100%.

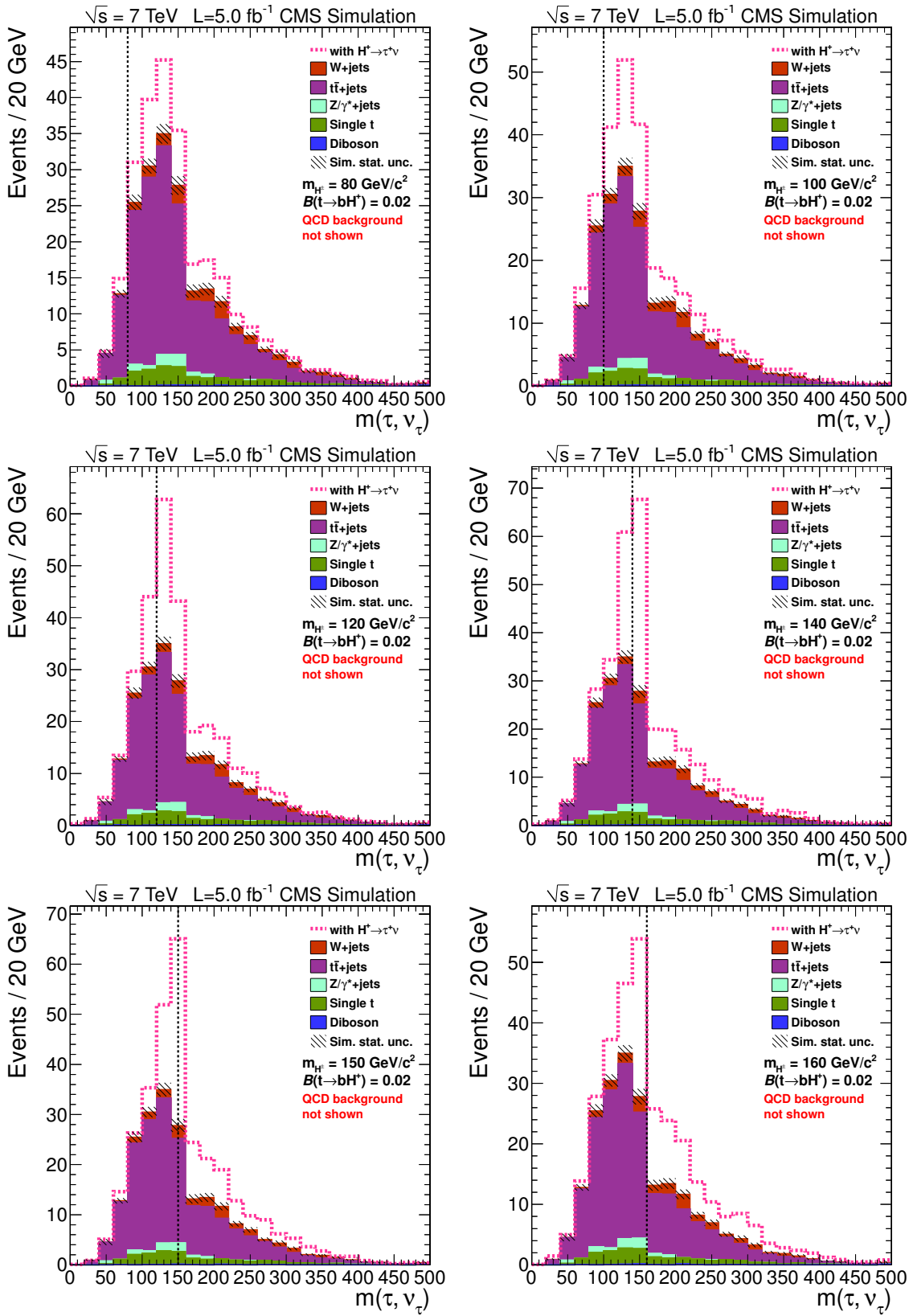


Figure 9.11: Invariant mass distributions with **no**  $m_t$  selection.

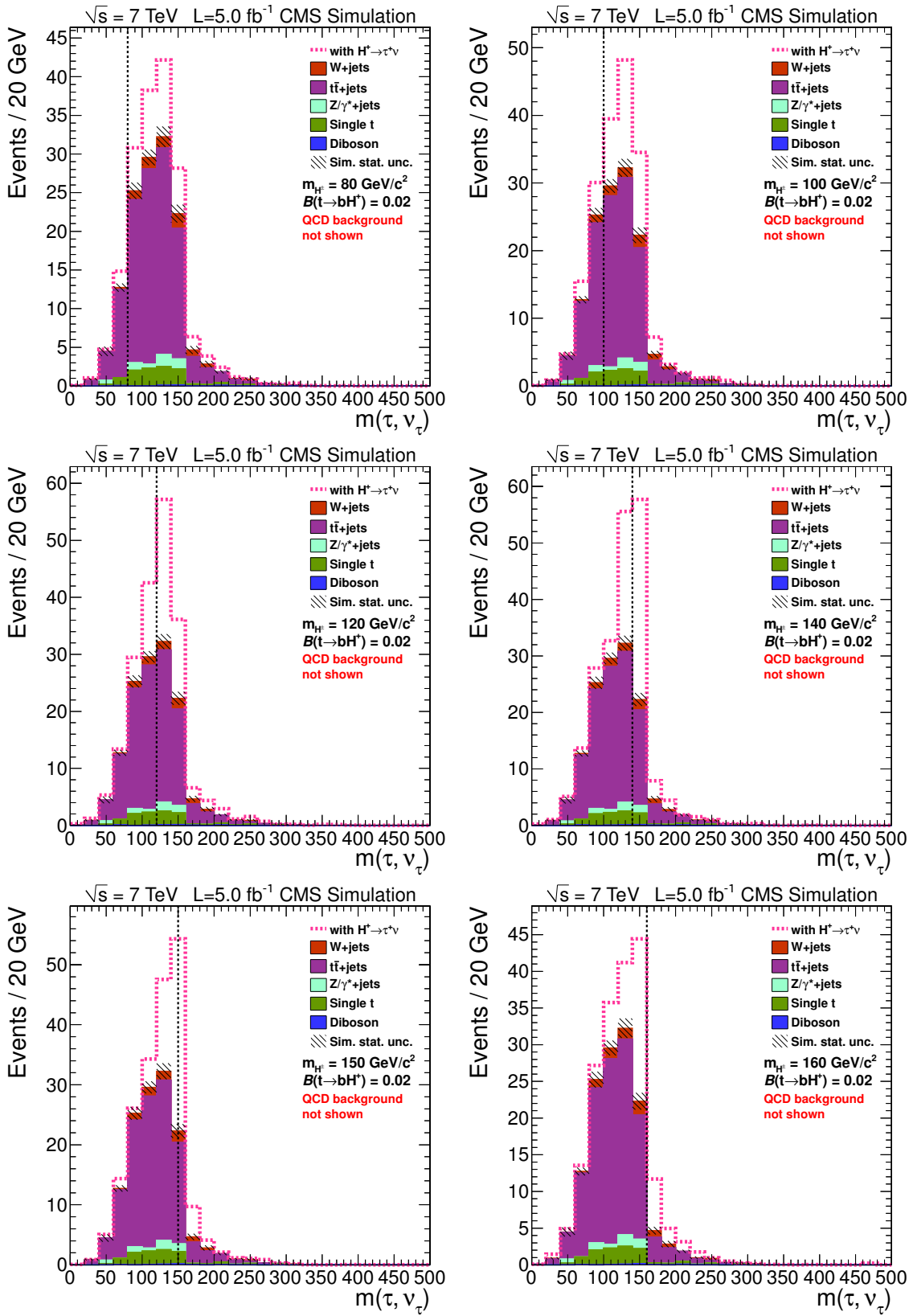


Figure 9.12: Invariant mass distributions with **loose**  $m_t$  selection.

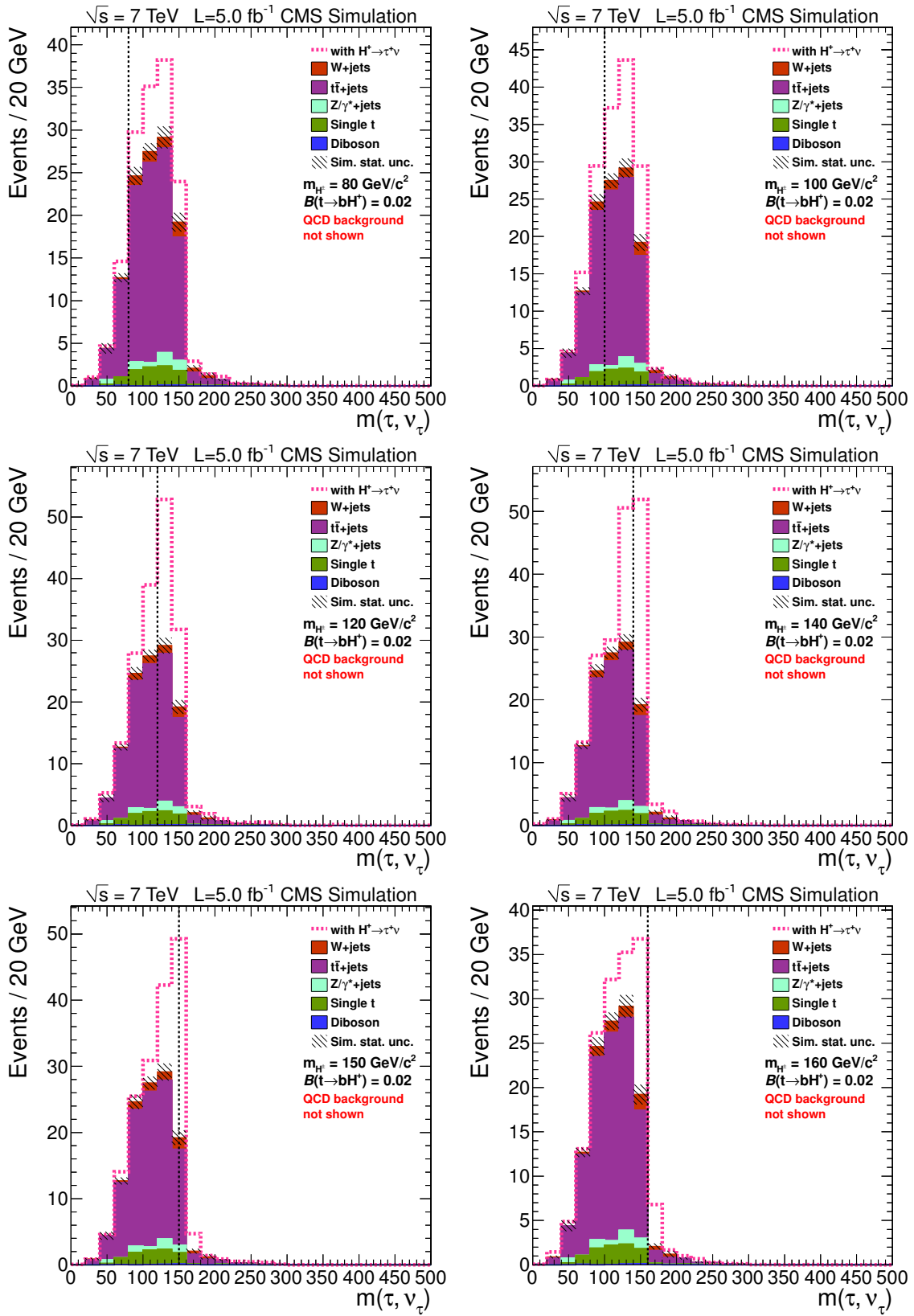


Figure 9.13: Invariant mass distributions with **medium**  $m_t$  selection.

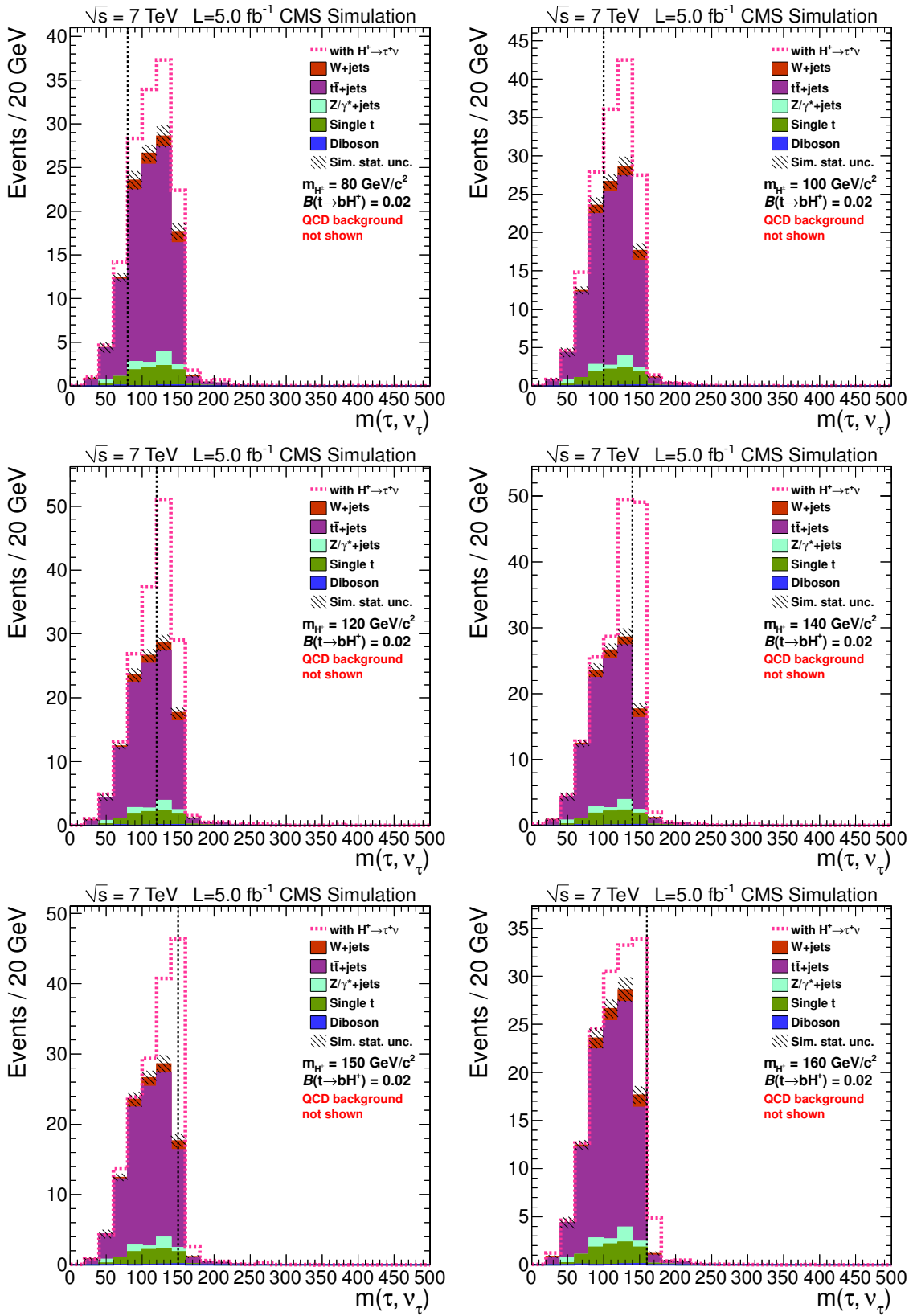


Figure 9.14: Invariant mass distributions with **tight**  $m_t$  selection.

## **Part III**

# **Results and discussion**

## 10 Results

L&S will tell.

---

Ancient proverb

### 10.1 Expected limits for the signal branching ratio

Expected limits on the signal branching ratio  $\mathcal{B}(t \rightarrow H^\pm b) \times \mathcal{B}(H^\pm \rightarrow \tau^\pm \nu_\tau)$  were calculated using the modified frequentist  $CL_s$  technique [102–104] implemented in the L&S software package [105]. The ‘LHC’ approach to specifying the test statistic and treatment of systematic uncertainties is used. This approach was agreed on by the CMS and ATLAS collaborations [106]. The complete statistical method used to set the limits is explained in Ref. [42]. Expected limits for the *tight* top quark invariant mass selection scenario were failed to be produced for technical reasons.

As the object here is only to find out, how the *expected limits* that can be set using the invariant mass distribution compare to those that can be set using the transverse mass, only the expected limits are shown while the *observed limits* (i.e. the ‘data points’ in colloquial terms) are not. Due to the blinding of the data explained in Section 1, observed limits could have been shown only for a small fraction of the recorded data in any case.

Even for the expected limits, *the results presented here are by no means definite and final*, though they do provide evidence in the search for the mass variable that is likely to give better sensitivity to a possible signal. There are the following two significant differences between the presented preliminary analysis and the next presentation of  $H^\pm$  search results that is in preparation. First, only the systematic uncertainties of the event yields (i.e. the normalization of the event distribution), not those of the shapes of the distributions are taken into account. This is expected to provide a reasonable approximation and to give physically sensible results. The reason for this approximation is the unfinished development of a more adequate treatment of systematic uncertainties. Second, at the time of the preparation of this thesis, the  $\tau$  embedding method for background measurement presented in Section 8.1 is still under re-validation because of new, subtle effects that were found with an increased number of simulated events and the fact that there are major changes in the present analysis compared to Ref. [22], for which the method was developed [107]. Therefore, the electroweak (including  $t\bar{t}$ ) background with genuine  $\tau$  leptons is not measured from data here but estimated from simulation instead.

The lowest expected limits using the transverse mass could be obtained using the *medium* back-to-back cut scenario. The expected median reaches from 2.5% ( $M_{H^\pm} = 80$  GeV) down to 0.37% ( $M_{H^\pm} = 160$  GeV). Over most of the mass range, the lowest expected limits using the invariant mass could be obtained using the *loose* back-to-back cut scenario and the *medium* top quark invariant mass ( $m_t$ ) selection scenario. These lead to an expected median between 1.9% ( $M_{H^\pm} = 80$  GeV) and 0.13% ( $M_{H^\pm} = 160$  GeV). The optimal expected limits using the transverse and the invariant mass are shown in Fig. 10.1, including with confidence bands corresponding to one and two standard deviations. To facilitate comparison between using the two mass variables, the corresponding median expected limits are shown together in Fig. 10.2. Depending on the  $H^\pm$  mass, the median expected limit obtained using the invariant mass is about equal ( $M_{H^\pm} = 120$  GeV) to almost three times lower ( $M_{H^\pm} = 160$  GeV) than the limit obtained using the transverse mass.

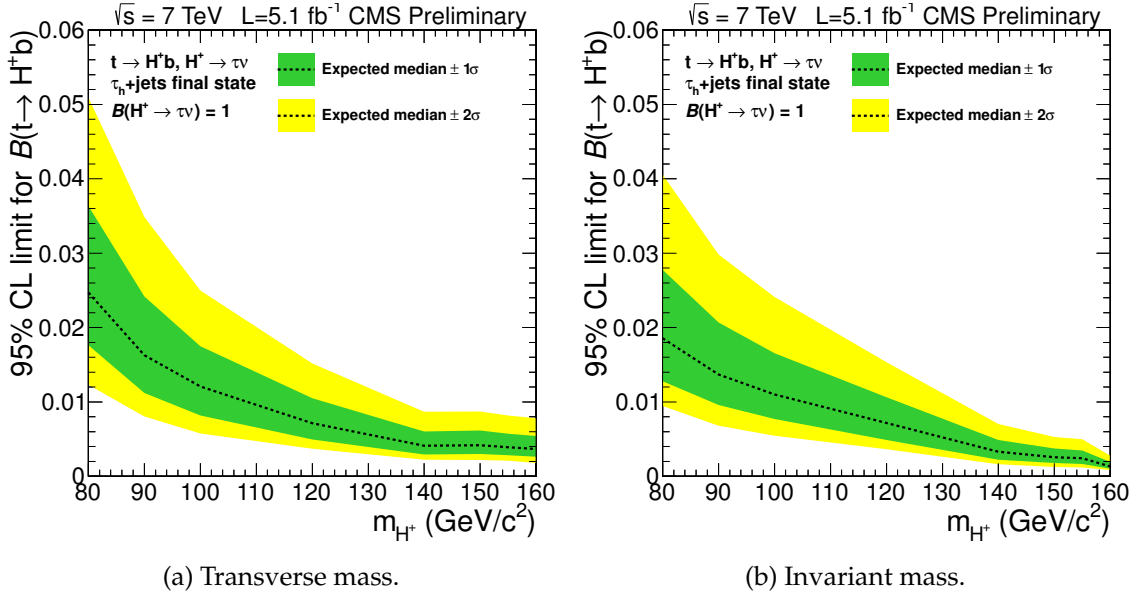


Figure 10.1: Optimal expected limits on the signal branching ratio obtained using the transverse mass (*medium* back-to-back cut scenario) and the invariant mass (*loose* back-to-back cut scenario, *medium*  $m_t$  selection scenario).

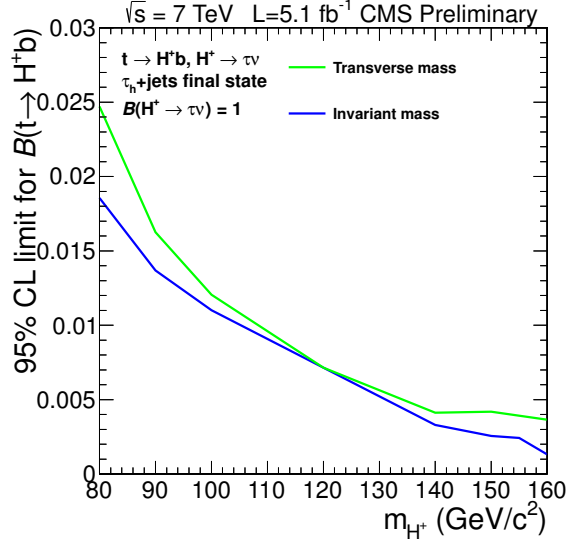


Figure 10.2: Comparison of the optimal median expected limits obtained using the transverse and the invariant mass.

To allow comparison of the different back-to-back cut scenarios, the median expected limits corresponding to them are shown in Fig. 10.3. The median expected limits corresponding to the different  $m_t$  selection scenarios are shown in Fig. 10.4, all obtained using the *loose* back-to-back cut scenario, as this was found to give optimal results when using the invariant mass.

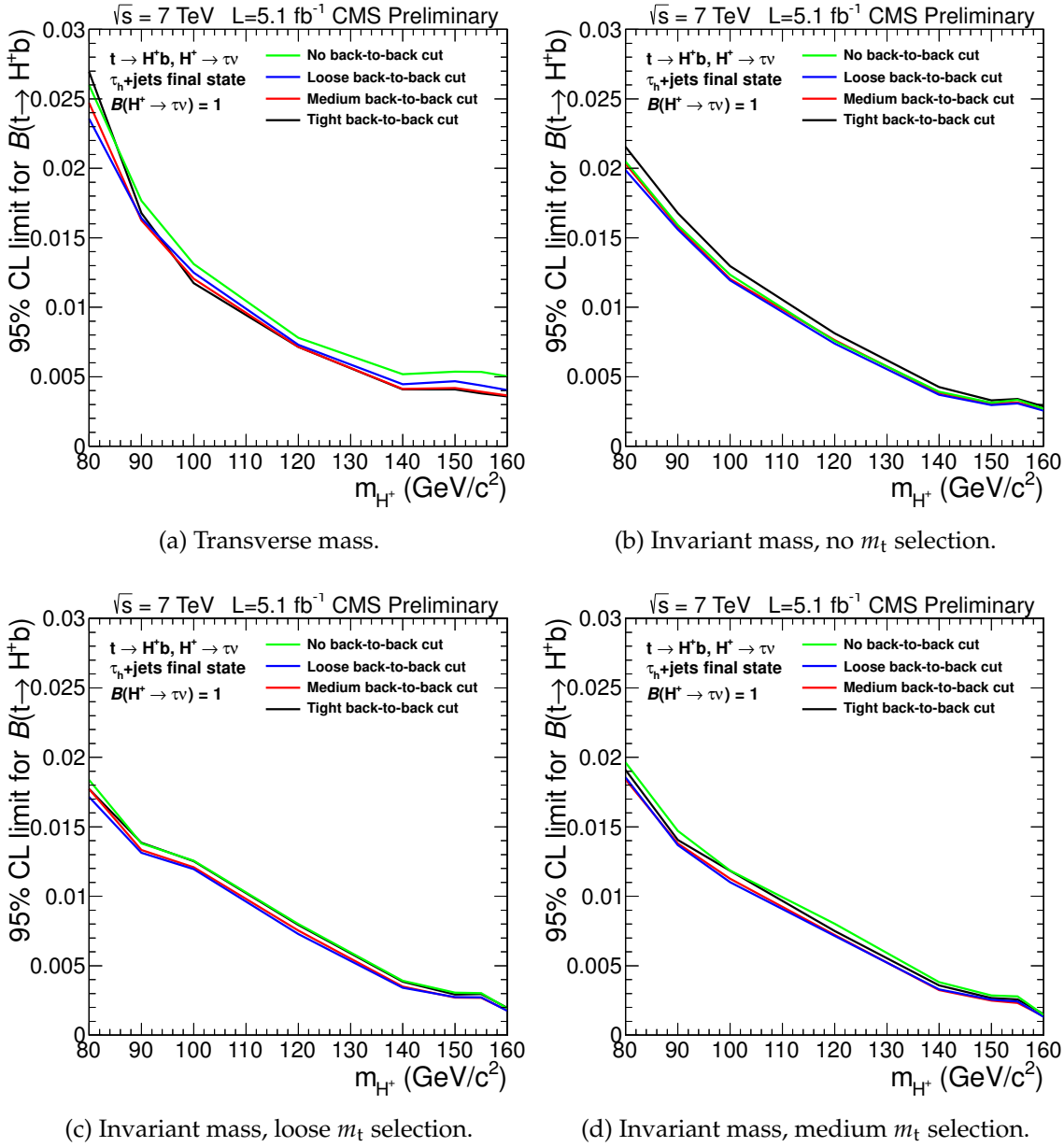


Figure 10.3: Influence of the choice of back-to-back selection scenario on the median expected limit.

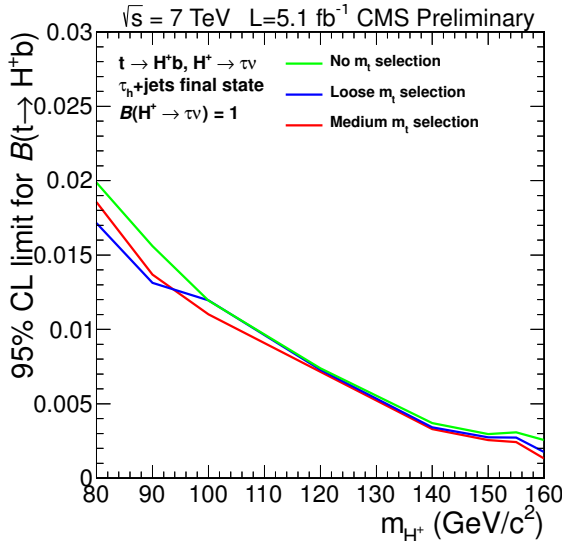


Figure 10.4: Influence of the choice of top quark invariant mass selection scenario on the median expected limit.

## 10.2 Systematic uncertainties

The systematic uncertainties that influence the limit calculation are estimated based on variations of the parameters of the analysis. In the preliminary analysis presented here, only the systematic uncertainty of the normalization of each distribution, not that of its shape, have been considered. They are all taken into account as relative uncertainties, i.e. their absolute size is proportional to the observed number of events.

Systematic uncertainties that are expected to have the largest impact on both the transverse and invariant mass distribution are those related to the identification of  $\tau$  leptons as well as the energy scale of hadronic jets,  $\tau$ -jets, and the  $E_T^{\text{miss}}$  contribution from unclustered energy deposits in the detector. The systematic uncertainty related to b-tagging could also influence the invariant mass distribution. The reason why the above are thought to be of importance for the distribution shapes is that they are related to the physics objects used to obtain these shapes. Other systematic uncertainties (e.g. those related to the trigger, pile-up modelling, or the cross sections) have similar absolute values, but are expected to mostly affect the total event yield, not the distribution shapes. The systematic uncertainties taken into account in the analysis as well as approximate values used for them are shown in Table 10.1.

	HH/HW	QCD multijets	W+jets	t̄t	Z/γ*	Single top	Diboson
Trigger, τ part			7	7		7	
Trigger, $E_T^{\text{miss}}$ part	10		10	10	10	10	10
Tau identification	6		6	6	6	6	6
Energy scale, τ-jets	3		3	3	3	3	3
Energy scale, hadr. jets	3		3	3	3	3	3
Energy scale, unclust. $E_T^{\text{miss}}$	1		1	1	1	1	1
Lepton (e, μ) veto	< 1		< 1	< 1	< 1	< 1	< 1
b-tagging	4			3		4	
b-mistagging			9		8		7
QCD bkg measurement		19					
Cross section	$^{+5}_{-6}$		5	$^{+5}_{-6}$	4	8	4
Luminosity	2		2	2	2	2	2
Pile-up modelling	5		5	5	5	5	5

Table 10.1: Systematic uncertainties taken into account in the preliminary analysis and their approximate values in percent. The exact values of some uncertainties depend on the used optimization scenario ( $m_t$  selection, back-to-back cut).

### 10.3 Correspondence between invariant mass and rest mass

To find out how well the position of the  $H^\pm$  peak in the reconstructed invariant mass distribution of the  $H^\pm$  samples corresponds to the charged Higgs boson rest mass, the invariant mass distributions were fitted with Gaussian as well as Breit–Wigner distributions. The fit functions are given by the expressions

$$f_G(m) = \frac{N}{\Gamma\sqrt{2\pi}} \exp\left(-\frac{(m-\mu)^2}{2\Gamma^2}\right) \quad (\text{Gaussian}), \quad (10.1)$$

$$f_{BW}(m) = \frac{N}{2\pi} \frac{\Gamma}{(m-\mu)^2 + \Gamma^2/4} \quad (\text{Breit–Wigner}), \quad (10.2)$$

where each function has three parameters to be determined by fitting: the normalization  $N$ , the mean (Gaussian) or median (Breit–Wigner)  $\mu$ , and the width  $\Gamma$ . Note that the mean of a Breit–Wigner distribution is undefined, since the integral  $\int_{-\infty}^{\infty} m f_{BW}(m) dm$  diverges.

The fits were performed on invariant mass distributions of signal samples obtained using the *medium* top invariant mass selection scenario, since this gives the lowest expected limits for the signal branching ratio and is therefore the most attractive scenario. The log-likelihood method was used for fitting the parameters. The fit range was adjusted separately for each signal sample, since the shapes of the distributions varied qualitatively with the  $H^\pm$  mass. This variation may be due to the relatively limited phase space available to the decay products of the top quarks. The invariant mass distribution of the tau-and-neutrino system fall off sharply near the top quark rest mass, while it falls off more gently towards the low-mass end of the spectrum. This limits the feasibility of fitting it with a Gaussian or a Breit–Wigner distribution, which are both symmetric with respect to their maximum.

The fit ranges and the results of the fits are shown in Table 10.2. The fitted invariant mass distributions are shown in Appendix D. For charged Higgs boson masses in the range 120–160 GeV, the fitted mean/median of the invariant mass peak is within  $\pm 10$  GeV of the rest mass, and in most cases within  $\pm 2 \times$  (fit error). Results for the Gaussian and the Breit–Wigner distribution are similar.

Rest mass	Fit range	Gaussian fit		Breit–Wigner fit	
		Fitted mean	$\chi^2/\text{d.o.f.}$	Fitted median	$\chi^2/\text{d.o.f.}$
80	80–160	$119 \pm 8$	3/13	$120 \pm 9$	4/13
90	70–160	$120 \pm 5$	5/15	$120 \pm 6$	5/15
100	90–165	$126 \pm 4$	8/12	$127 \pm 5$	9/12
120	80–165	$129 \pm 3$	24/14	$132 \pm 3$	16/14
140	110–165	$142 \pm 2$	16/8	$143 \pm 2$	14/8
150	130–170	$147 \pm 2$	29/5	$148 \pm 2$	27/5
155	140–170	$153 \pm 1$	8/3	$153 \pm 1$	8/3
160	140–175	$154 \pm 2$	14/4	$155 \pm 2$	15/4

Table 10.2: Invariant mass fit results. The columns of fitted means also show the fit error. Fit ranges were roughly chosen to give a  $\chi^2/\text{d.o.f.}$  ratio as close to 1 as possible. All rest masses, ranges and means in GeV.

#### 10.4 Distribution of events in the transverse mass–invariant mass plane

As was discussed in the introduction (Section 1), the signal sensitivity might be improved further by considering the distribution of events as a function of both the transverse and the invariant mass. As of the preparation of this thesis, the option of using a two-dimensional distribution to calculate the expected limits was not yet implemented technically, so that no expected limits are shown. Instead, only the distributions of events in the transverse mass–invariant mass plane are shown for the  $t\bar{t}$  background (Fig. 10.5) and the signal plus combined background (excluding QCD multijets) in the different  $m_t$  selection scenarios (Figs. 10.6–10.9). This is to give a qualitative idea of how well the background peak due to the W boson—most clearly visible in the  $t\bar{t}$ -only distribution in Fig. 10.5—is separated from the signal peak and how stricter  $m_t$  requirements influence the distribution. It can also be seen that the fraction of events below the straight line  $m_T = m$  is relatively small. This is in agreement with the expectation that  $m_T \leq m$ .

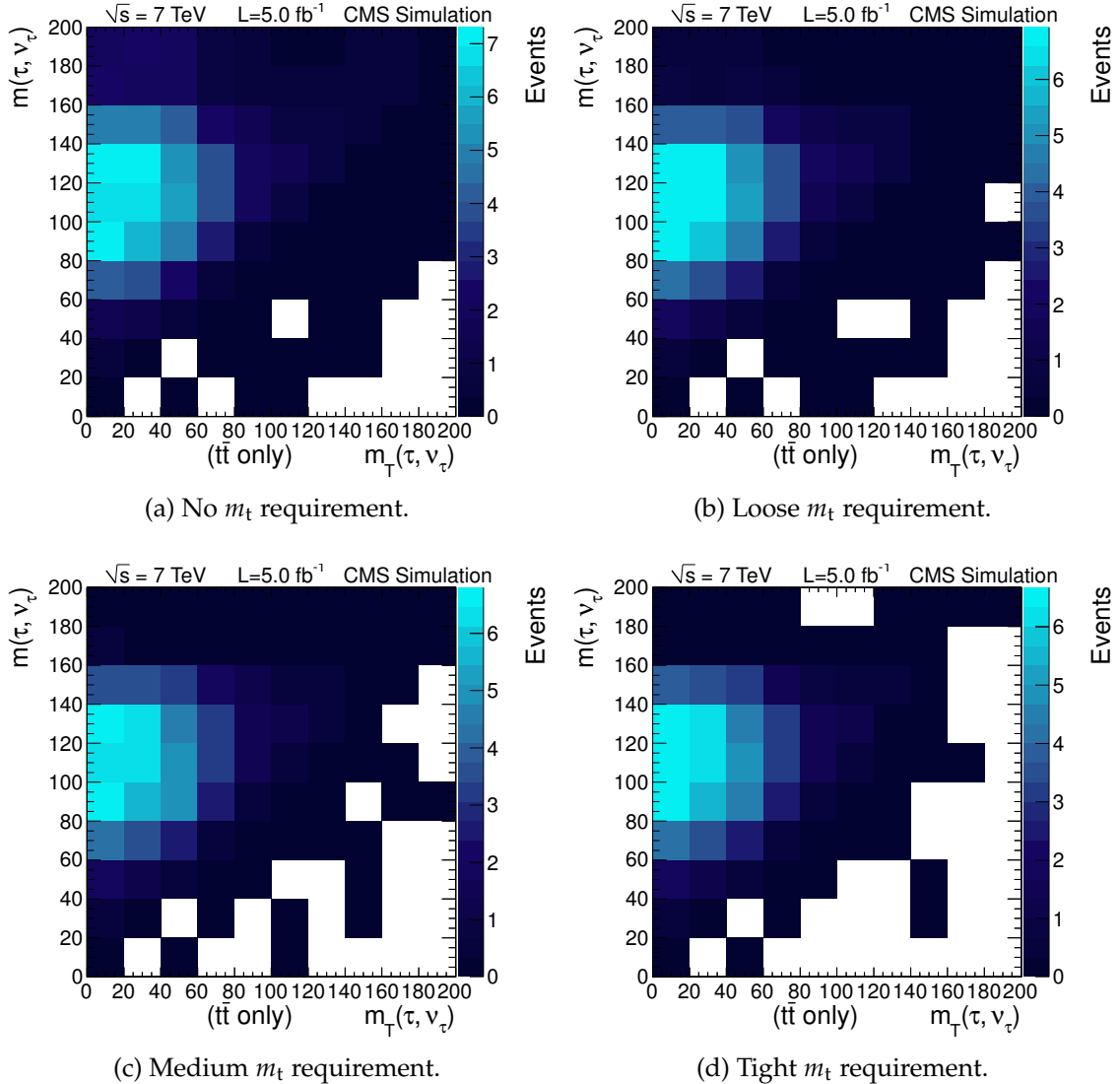


Figure 10.5: Transverse mass vs. invariant mass distribution of the  $t\bar{t}$  background, using different top invariant mass requirements.

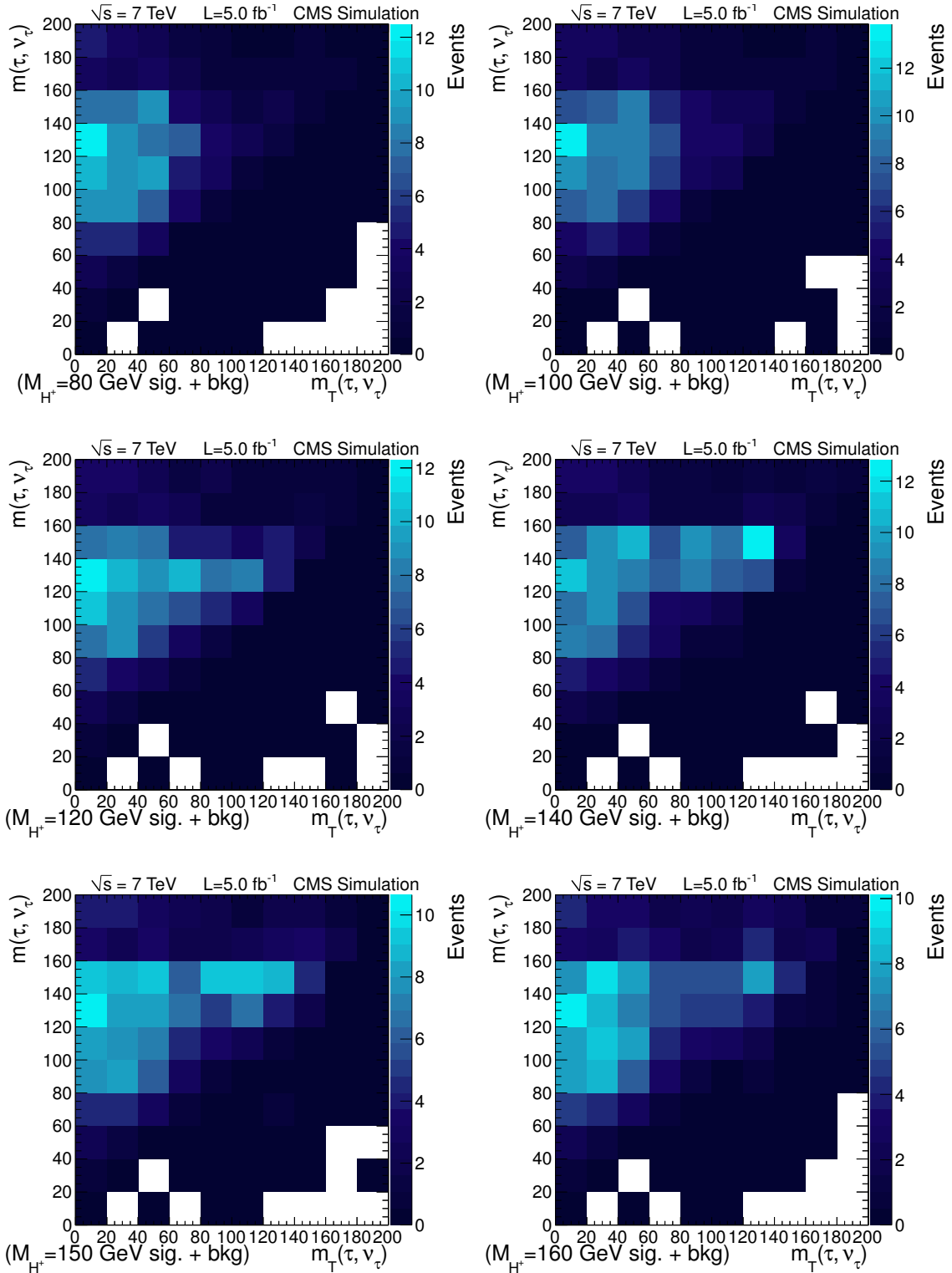


Figure 10.6: Transverse mass vs. invariant mass distribution of background plus signal using **no top invariant mass requirement**. **QCD background not included.**

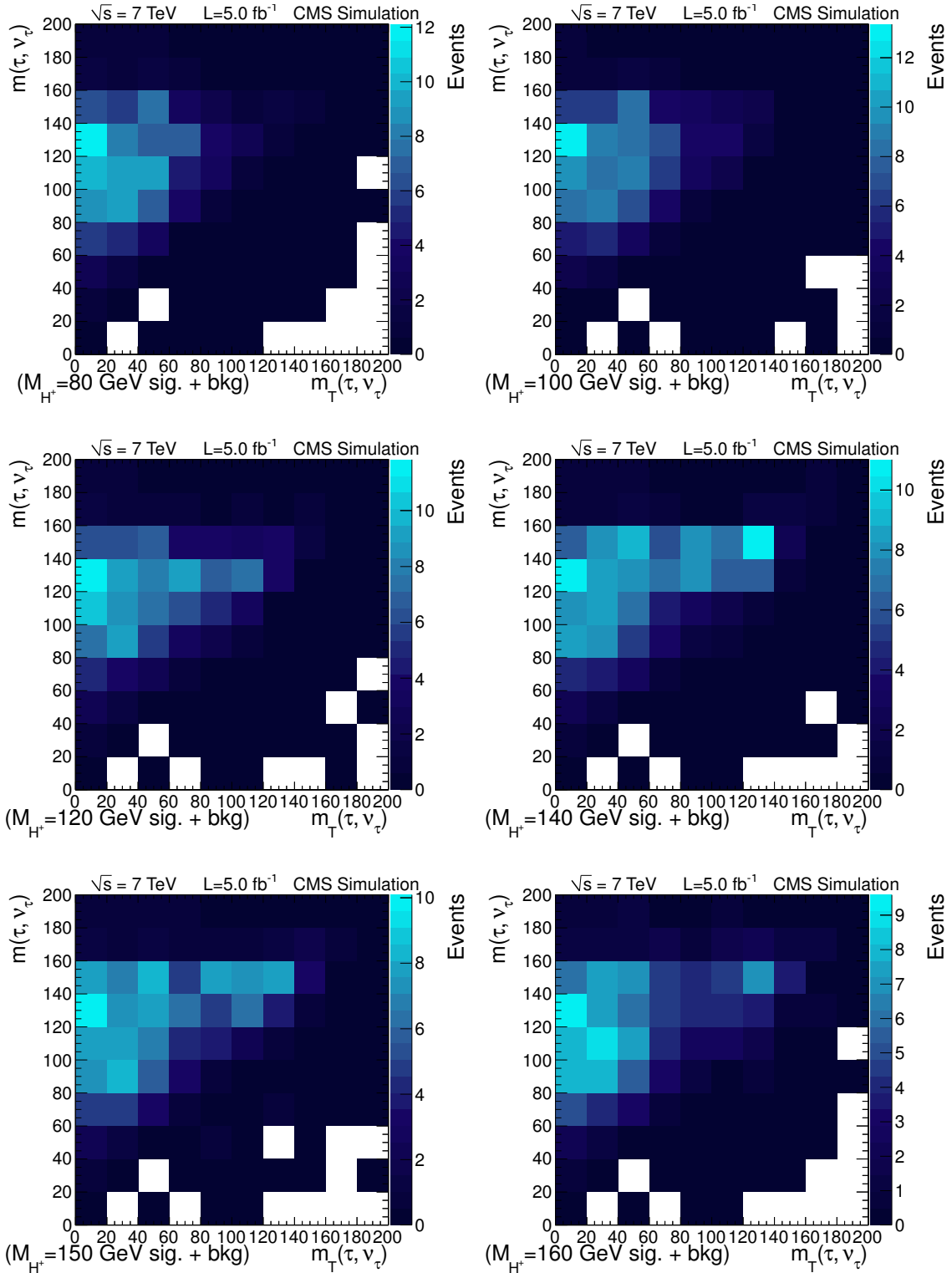


Figure 10.7: Transverse mass vs. invariant mass distribution of background plus signal using the **loose top invariant mass requirement**. **QCD background not included.**

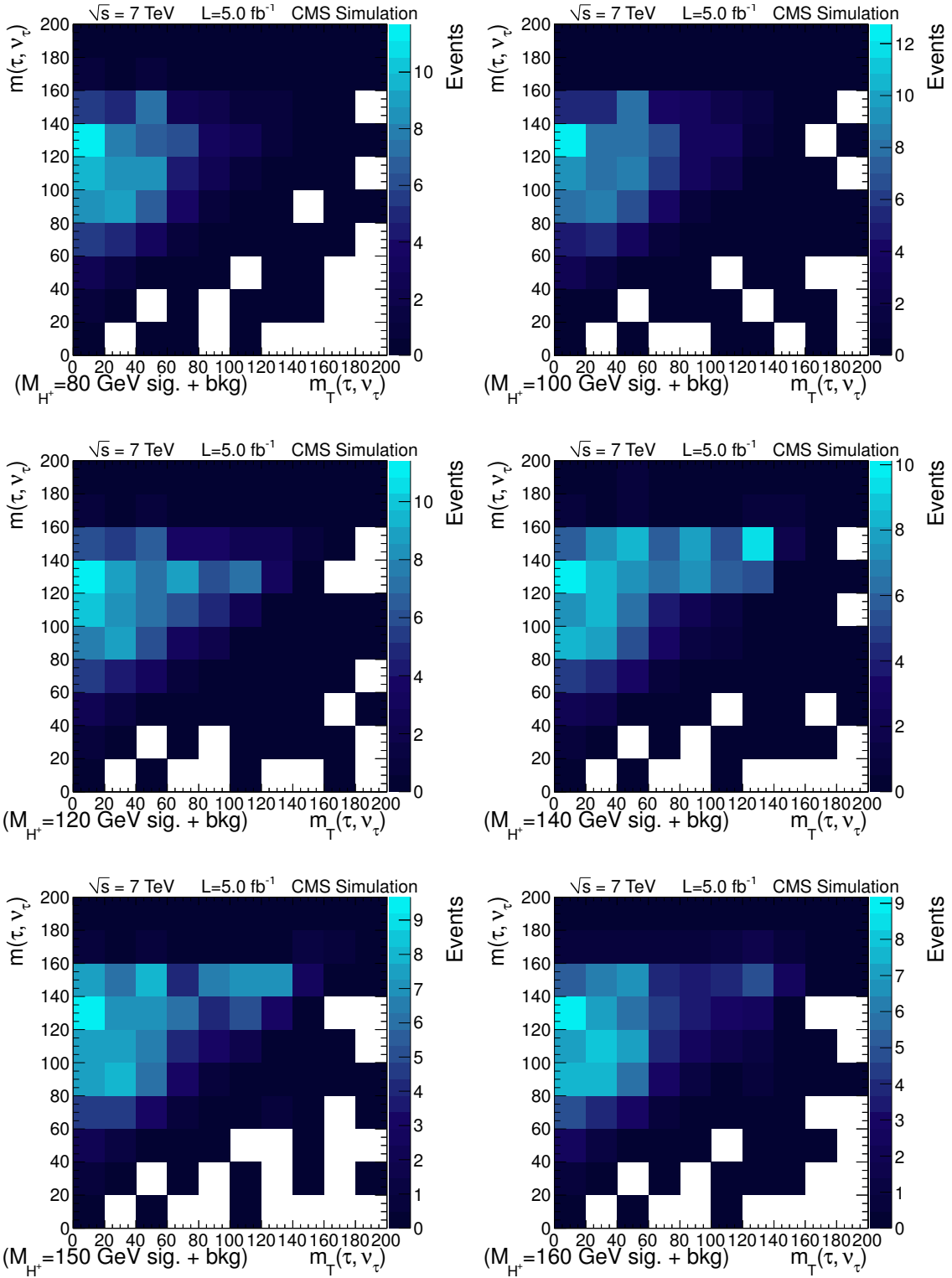


Figure 10.8: Transverse mass vs. invariant mass distribution of background plus signal using the **medium top invariant mass requirement**. **QCD background not included.**

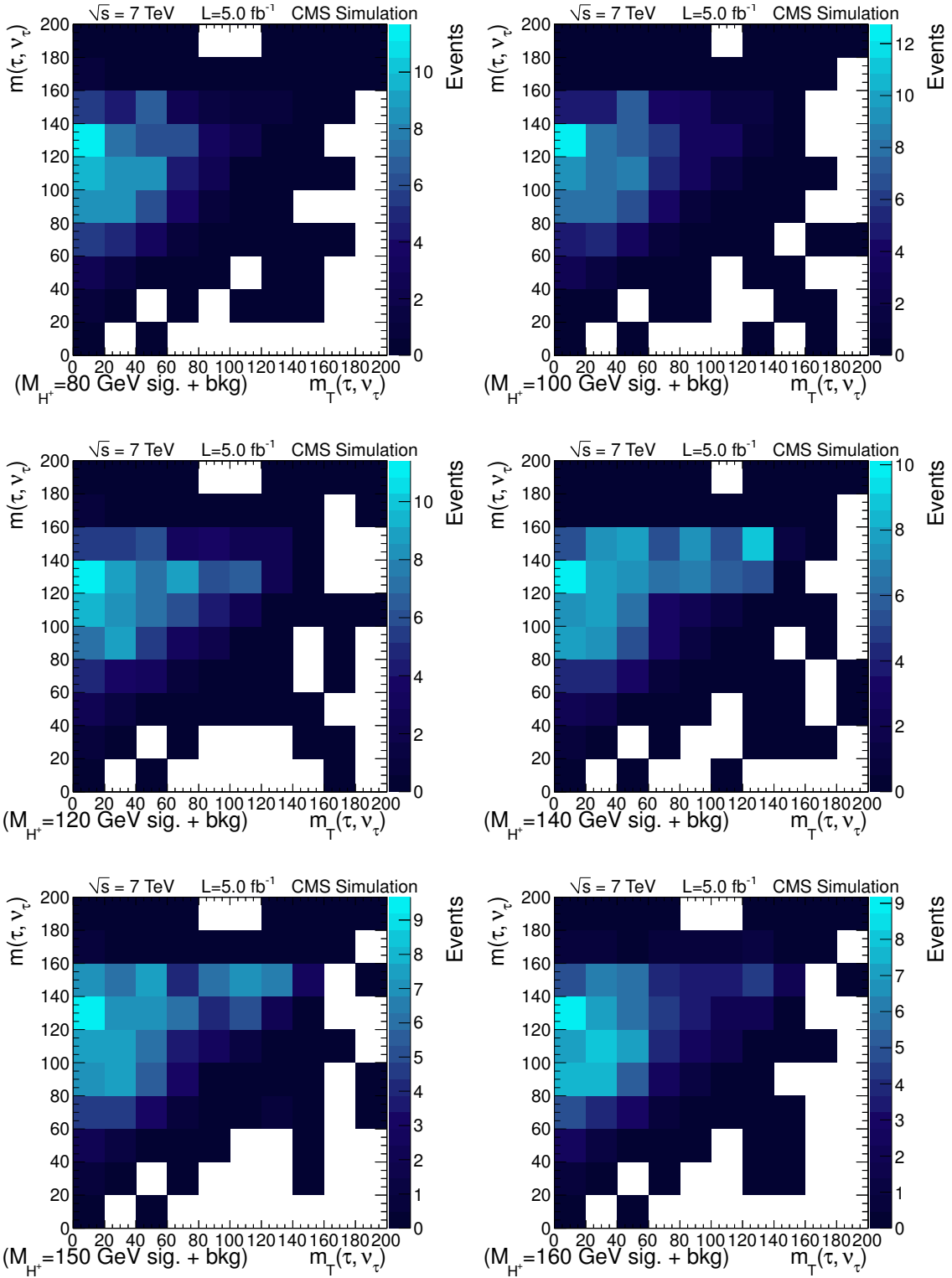


Figure 10.9: Transverse mass vs. invariant mass distribution of background plus signal using the **tight top invariant mass requirement**. **QCD background not included.**

## 11 Conclusions

All particle physics is quite useless.

---

Oscar Wilde

An algorithm for reconstructing the invariant mass of a  $\tau$ -jet and a pair of tau neutrinos has been presented. The invariant mass distribution may be used to extract a possible signal in a search for light charged Higgs bosons (studied mass range: 80–160 GeV) produced in top quark decays and decaying to a tau lepton and a tau neutrino, as an alternative or complement to the currently used transverse mass distribution. It has been shown that the ambiguity caused by having two possible solutions arising in the invariant mass calculation can be resolved and that initially unphysical solutions may be recovered at least in some fraction of the events in which they appear. The invariant mass reconstruction algorithm has been shown to yield a physically sensible invariant mass distribution when used with simulated events. The position of the simulated  $H^\pm$  signal peak was determined by fitting the distribution and found to correspond well to the  $H^\pm$  rest mass, if  $M_{H^\pm}$  is in the range 120–160 GeV. At the lower end of the studied mass range (80–120 GeV), the position of the invariant mass peak was found to be shifted to a higher value with respect to the rest mass. This is due to the method used to select the invariant mass solution in cases where there are two possibilities, which works well for higher but not for lower masses.

The invariant mass reconstruction algorithm offers several opportunities for optimization. The method for selecting a solution for the neutrinos' longitudinal momentum in cases where there are two possible solutions is very simple, based only on one observable. A more sophisticated method, perhaps using several observables, might improve the selection efficiency of the better solution and thus give a reconstructed invariant mass distribution that is closer to the true distribution. This may improve the signal sensitivity at the lower end of the studied mass range, where the current solution selection method performs poorly, by giving both a sharper signal and  $W$  background peak in the invariant mass distribution.

A preliminary analysis using data from proton-proton collisions at  $\sqrt{s} = 7$  TeV recorded by the CMS experiment, corresponding to an integrated luminosity of about  $5.1 \text{ fb}^{-1}$ , has been performed to calculate the expected limits on the signal branching ratio,  $\mathcal{B}(t \rightarrow H^\pm b) \times \mathcal{B}(H^\pm \rightarrow \tau^\pm \nu_\tau)$ . The background contribution from QCD multijet events was measured from data, while the other background contributions were estimated from simulation. The analysis was done for several scenarios with slightly different event selection requirements. The results were compared to find the optimal scenarios. In the optimal respective scenarios, using the transverse mass and the invariant mass for signal extraction leads to median expected limits on the signal branching ratio of 0.37% to 2.5% and 0.13% to 1.9%, respectively, depending on the  $H^\pm$  rest mass. This means that the median expected limits that can be set using the invariant mass are *up to* almost three times lower compared to using the transverse mass. The relative improvement is larger at both ends of the studied mass range than in the middle. The improvement is expected to become smaller when possible new systematic uncertainties related to the invariant mass reconstruction are taken into account. Both using the transverse and the invariant mass, the analysis is much more sensitive to the presence of heavier charged Higgs bosons within the studied mass range than that of lighter ones.

Even better signal sensitivity might be achieved by using the distribution of events in the

plane of transverse mass versus invariant mass for signal extraction. The corresponding limits could not yet be set because of current technical limitations, but the distributions suggest that the simulated signal peak can be separated well from the background at least in the heavier mass range. The QCD background was not included in the distributions that lead to this statement, since it could not be simulated reliably.

Regardless of whether the transverse mass, invariant mass, or a combination of the two is used for signal extraction, the sensitivity of the analysis has been significantly improved since the last publication of results in May 2012 (Ref. [22]). In the meantime, the amount of recorded data available for the analysis has increased by a factor of five. This means that the next publication of the search results will provide much more quantitative knowledge about the existence or non-existence of charged Higgs bosons. We are living in interesting times.

We are matter wondering about itself,  
machines building machines to figure themselves out,  
a Universe creating great eyes to look at itself,  
to search for what may always have been everywhere  
or never anywhere.

We are matter that wants to find out.

## References

- [1] Particle Data Group, *Review of Particle Physics*, *Phys. Rev. D* **86** (2012).
- [2] S. Glashow, *Partial Symmetries of Weak Interactions*, *Nucl. Phys.* **22** (1961) 579–588.
- [3] S. Weinberg, *A Model of Leptons*, *Phys. Rev. Lett.* **19** (1967) 1264–1266.
- [4] A. Salam, *Weak and Electromagnetic Interactions*, in *Elementary Particle Physics: Relativistic Groups and Analyticity* (N. Svartholm, ed.), vol. C680519 of *Proceedings of the Eighth Nobel Symposium*, pp. 367–377, Almqvist & Wiksell, 1968.
- [5] F. Englert and R. Brout, *Broken symmetry and the mass of gauge vector mesons*, *Phys. Rev. Lett.* **13** (1964) 321–323.
- [6] P. W. Higgs, *Broken symmetries, massless particles and gauge fields*, *Phys. Lett.* **12** (1964) 132–133.
- [7] P. W. Higgs, *Broken symmetries and the masses of gauge bosons*, *Phys. Rev. Lett.* **13** (1964) 508–509.
- [8] G. S. Guralnik, C. R. Hagen, and T. W. B. Kibble, *Global conservation laws and massless particles*, *Phys. Rev. Lett.* **13** (1964) 585–587.
- [9] P. W. Higgs, *Spontaneous symmetry breakdown without massless bosons*, *Phys. Rev.* **145** (1966) 1156–1163.
- [10] T. W. B. Kibble, *Symmetry breaking in non-abelian gauge theories*, *Phys. Rev.* **155** (Mar, 1967) 1554–1561.
- [11] CMS Collaboration, *Observation of a new boson at a mass of 125 GeV with the CMS experiment at the LHC*, *Phys. Lett.* **B716** (2012) 30–61, [[arXiv:1207.7235](#)].
- [12] ATLAS Collaboration, *Observation of a new particle in the search for the Standard Model Higgs boson with the ATLAS detector at the LHC*, *Phys. Lett.* **B716** (2012) 1–29, [[arXiv:1207.7214](#)].
- [13] Y. Golfand and E. Likhtman, *Extension of the Algebra of Poincare Group Generators and Violation of P Invariance*, *JETP Lett.* **13** (1971) 323–326.
- [14] D. Volkov and V. Akulov, *Is the Neutrino a Goldstone Particle?*, *Phys. Lett.* **B46** (1973) 109–110.
- [15] J. Wess and B. Zumino, *Supergauge Transformations in Four-Dimensions*, *Nucl. Phys.* **B70** (1974) 39–50.
- [16] J. Gunion, H. Haber, G. Kane, and S. Dawson, *The Higgs Hunter’s Guide*. Frontiers in Physics Series. Addison-Wesley, 1990.
- [17] H. Georgi, *Model of soft CP violation*, *Hadronic J.* **1** (1978), no. 1.
- [18] L3 Collaboration, *Search for charged Higgs bosons at LEP*, *Phys.Lett.* **B575** (2003) 208–220, [[hep-ex/0309056](#)].
- [19] ALEPH Collaboration, *Search for charged Higgs bosons in  $e^+e^-$  collisions at energies up to  $\sqrt{s} = 209$  GeV*, *Phys. Lett.* **B543** (2002) 1–13, [[hep-ex/0207054](#)].

- [20] DELPHI Collaboration, *Search for charged Higgs bosons at LEP in general two Higgs doublet models*, *Eur. Phys. J.* **C34** (2004) 399–418, [[hep-ex/0404012](#)].
- [21] OPAL Collaboration, *Search for Charged Higgs Bosons in  $e^+e^-$  Collisions at  $\sqrt{s} = 189 - 209$  GeV*, *Eur. Phys. J.* **C72** (2012) 2076, [[arXiv:0812.0267](#)].
- [22] CMS Collaboration, *Search for a light charged Higgs boson in top quark decays in pp collisions at  $\sqrt{s} = 7$  TeV*, *JHEP* **1207** (2012) 143, [[arXiv:1205.5736](#)].
- [23] ATLAS Collaboration, *Search for charged Higgs bosons decaying via  $H^+ \rightarrow \tau\nu$  in top quark pair events using pp collision data at  $\sqrt{s} = 7$  TeV with the ATLAS detector*, *JHEP* **1206** (2012) 039, [[arXiv:1204.2760](#)].
- [24] S. Weinberg, *Implications of dynamical symmetry breaking*, *Phys. Rev. D* **13** (1976) 974–996.
- [25] S. Weinberg, *Implications of dynamical symmetry breaking: An addendum*, *Phys. Rev. D* **19** (1979) 1277–1280.
- [26] L. Susskind, *Dynamics of spontaneous symmetry breaking in the Weinberg–Salam theory*, *Phys. Rev. D* **20** (1979) 2619–2625.
- [27] B. Lee, *Perspectives on Theory of Weak Interactions*, in *Proceedings of the XVI International Conference on High Energy Physics* (J. Jackson, A. Roberts, and International Union of Pure and Applied Physics, eds.), vol. 4, (Batavia, IL), National Accelerator Laboratory, 1972.
- [28] D. Ross and M. Veltman, *Neutral currents and the Higgs mechanism*, *Nuclear Physics B* **95** (1975), no. 1 135 – 147.
- [29] S. L. Glashow and S. Weinberg, *Natural conservation laws for neutral currents*, *Phys. Rev. D* **15** (1977) 1958–1965.
- [30] P. Fayet, *Supergauge Invariant Extension of the Higgs Mechanism and a Model for the electron and Its Neutrino*, *Nucl. Phys.* **B90** (1975) 104–124.
- [31] P. Fayet, *Supersymmetry and Weak, Electromagnetic and Strong Interactions*, *Phys. Lett.* **B64** (1976) 159.
- [32] P. Fayet, *Spontaneously Broken Supersymmetric Theories of Weak, Electromagnetic and Strong Interactions*, *Phys. Lett.* **B69** (1977) 489.
- [33] S. Dimopoulos and H. Georgi, *Softly Broken Supersymmetry and SU(5)*, *Nucl. Phys.* **B193** (1981) 150.
- [34] K. Inoue, A. Kakuto, H. Komatsu, and S. Takeshita, *Low-Energy Parameters and Particle Masses in a Supersymmetric Grand Unified Model*, *Prog. Theor. Phys.* **67** (1982) 1889.
- [35] K. Inoue, A. Kakuto, H. Komatsu, and S. Takeshita, *Renormalization of Supersymmetry Breaking Parameters Revisited*, *Prog. Theor. Phys.* **71** (1984) 413.
- [36] K. Inoue, A. Kakuto, H. Komatsu, and S. Takeshita, *Aspects of Grand Unified Models with Softly Broken Supersymmetry*, *Prog. Theor. Phys.* **68** (1982) 927.
- [37] CMS Collaboration, *Measurement of the  $t\bar{t}$  production cross section in pp collisions at with lepton + jets final states*, *Physics Letters B* **720** (2013), no. 1–3 83 – 104.

- [38] CMS Collaboration, *Measurement of the  $t\bar{t}$  production cross section in the all-jet final state in  $pp$  collisions at  $\sqrt{s} = 7$  TeV*, *JHEP* **1305** (2013) 065, [[arXiv:1302.0508](#)].
- [39] CMS Collaboration, *Measurement of the top-antitop production cross section in the tau+jets channel in pp collisions at  $\sqrt{s} = 7$  TeV*, *Eur. Phys. J.* **C73** (2013) 2386, [[arXiv:1301.5755](#)].
- [40] CMS Collaboration, *Evidence for associated production of a single top quark and w boson in pp collisions at  $\sqrt{s} = 7$  TeV*, *Phys. Rev. Lett.* **110** (Jan, 2013).
- [41] L. A. Wendland, *Identification of Hadronically Decaying Tau Leptons in Searches for Heavy MSSM Higgs Bosons with the CMS Detector at the CERN LHC*. PhD thesis, University of Helsinki, HU-P-D170, 2009.
- [42] M. J. Kortelainen, *Search for a Light Charged Higgs Boson in the CMS Experiment in pp Collisions at  $\sqrt{s} = 7$  TeV*. PhD thesis, University of Helsinki, HIP-2012-06, 2012.
- [43] D. Roy, *The hadronic tau decay signature of a heavy charged Higgs boson at LHC*, *Physics Letters B* **459** (1999), no. 4 607 – 614.
- [44] D. Roy, *Looking for the charged Higgs boson*, *Mod. Phys. Lett.* **A19** (2004) 1813–1828, [[hep-ph/0406102](#)].
- [45] CMS Collaboration, *The CMS experiment at the CERN LHC*, *JINST* **03** (2008).
- [46] CMS Collaboration, *CMS, the Compact Muon Solenoid: Technical proposal*, Tech. Rep. CERN-LHCC-94-38, CERN-LHCC-P-1, CERN, 1994.
- [47] CMS Collaboration, *CMS Physics: Technical Design Report Volume 1: Detector Performance and Software*. Technical Design Report CMS. CERN, Geneva, 2006.
- [48] W. Adam, B. Mangano, T. Speer, and T. Todorov, *Track reconstruction in the CMS tracker*, CMS Note CERN-CMS-NOTE-2006-041, CERN, 2005.
- [49] CMS Collaboration, *Tracking and Vertexing Results from First Collisions*, CMS Physics Analysis Summary CMS-PAS-TRK-10-001, CERN, 2010.
- [50] CMS Collaboration, *Measurement of Tracking Efficiency*, CMS Physics Analysis Summary CMS-PAS-TRK-10-002, CERN, 2010.
- [51] CMS Collaboration, *Measurement of Momentum Scale and Resolution of the CMS Detector using Low-mass Resonances and Cosmic Ray Muons*, CMS Physics Analysis Summary CMS-PAS-TRK-10-004, CERN, 2010.
- [52] K. Rose, *Deterministic annealing, clustering, and optimization*. PhD thesis, California Institute of Technology, 1991.
- [53] K. Rose, *Deterministic annealing for clustering, compression, classification, regression, and related optimization problems*, *Proceedings of the IEEE* **86** (1998), no. 11 2210–2239.
- [54] E. Chabanat and N. Estre, *Deterministic annealing for vertex finding at CMS*, in CERN-2005-002, pp. 287–290, 2005.
- [55] R. Frühwirth, W. Waltenberger, K. Prokofiev, T. Speer, and P. Vanlaer, *New developments in vertex reconstruction for CMS*, *Nucl. Instrum. Meth.* **A502** (2003) 699–701.

- [56] J. d'Hondt, P. Vanlaer, R. Frühwirth, and W. Waltenberger, *Sensitivity of robust vertex fitting algorithms*, *IEEE Trans. Nucl. Sci.* **51** (2004) 2037–2044.
- [57] T. Speer, K. Prokofiev, R. Frühwirth, W. Waltenberger, and P. Vanlaer, *Vertex fitting in the CMS tracker*, CMS Note CERN-CMS-NOTE-2006-032, CERN, 2006.
- [58] R. Frühwirth, W. Waltenberger, and P. Vanlaer, *Adaptive vertex fitting*, CMS Note CERN-CMS-NOTE-2007-008, CERN, 2007.
- [59] CMS Collaboration, *Tracking and Primary Vertex Results in First 7 TeV Collisions*, CMS Physics Analysis Summary CMS-PAS-TRK-10-005, CERN, 2010. Geneva, 2010.
- [60] CMS Collaboration, *Performance of CMS Muon Reconstruction in Cosmic-Ray Events*, *JINST* **5** (2010) T03022, [[arXiv:0911.4994](#)].
- [61] CMS Collaboration, *Performance of CMS muon reconstruction in pp collision events at  $\sqrt{s} = 7 \text{ TeV}$* , *JINST* **7** (2012) P10002, [[arXiv:1206.4071](#)].
- [62] S. Baffioni, C. Charlot, F. Ferri, D. Futyan, P. Meridiani, et al., *Electron reconstruction in CMS*, CMS Note CERN-CMS-NOTE-2006-040, CERN, 2007.
- [63] CMS Collaboration, *Electron reconstruction and identification at  $\sqrt{s} = 7 \text{ TeV}$* , CMS Physics Analysis Summary CMS-PAS-EGM-10-004, CERN, 2010.
- [64] E. Meschi, T. Monteiro, C. Seez, and P. Vikas, *Electron Reconstruction in the CMS Electromagnetic Calorimeter*, CMS Note CMS-NOTE-2001-034, CERN-CMS-NOTE-2001-034, CERN, 2001.
- [65] CMS Collaboration, *Studies of Tracker Material*, CMS Physics Analysis Summary CMS-PAS-TRK-10-003, CERN, 2010.
- [66] CMS Collaboration, *Isolated Photon Reconstruction and Identification at  $\sqrt{s} = 7 \text{ TeV}$* , CMS Physics Analysis Summary CMS-PAS-EGM-10-006, CERN, 2011.
- [67] CMS Collaboration, *Particle-flow commissioning with muons and electrons from J/Psi and W events at 7 TeV*, CMS Physics Analysis Summary CMS-PAS-PFT-10-003, CERN, 2010. Geneva, 2010.
- [68] CMS Collaboration, *Particle-Flow Event Reconstruction in CMS and Performance for Jets, Taus, and  $E_T^{\text{miss}}$* , CMS Physics Analysis Summary CMS-PAS-PFT-09-001, CERN, 2009.
- [69] CMS Collaboration, *Commissioning of the Particle-flow Event Reconstruction with the first LHC collisions recorded in the CMS detector*, CMS Physics Analysis Summary CMS-PAS-PFT-10-001, CERN, 2010.
- [70] CMS Collaboration, *Commissioning of the Particle-Flow reconstruction in Minimum-Bias and Jet Events from pp Collisions at 7 TeV*, CMS Physics Analysis Summary CMS-PAS-PFT-10-002, CERN, 2010.
- [71] CMS Collaboration, *Determination of Jet Energy Calibration and Transverse Momentum Resolution in CMS*, *JINST* **6** (2011) P11002, [[arXiv:1107.4277](#)].
- [72] CMS Collaboration, *The Jet Plus Tracks Algorithm for Calorimeter Jet Energy Corrections in CMS*, CMS Physics Analysis Summary CMS-PAS-JME-09-002, CERN, 2009.
- [73] CMS Collaboration, *Commissioning of TrackJets in pp Collisions at 7 TeV*, CMS Physics Analysis Summary CMS-PAS-JME-10-006, CERN, 2010.

- [74] S. Chekanov, *Jet algorithms: A Minireview*, in *ANL-HEP-CP-02-103*, pp. 478–486, 2002. [hep-ph/0211298](#).
- [75] G. P. Salam, *Towards Jetography*, *Eur. Phys. J.* **C67** (2010) 637–686, [[arXiv:0906.1833](#)].
- [76] S. Catani, Y. L. Dokshitzer, and B. Webber, *The  $k_\perp$  clustering algorithm for jets in deep inelastic scattering and hadron collisions*, *Phys. Lett.* **B285** (1992) 291–299.
- [77] S. Catani, Y. L. Dokshitzer, M. Seymour, and B. Webber, *Longitudinally invariant  $k_\perp$  clustering algorithms for hadron hadron collisions*, *Nucl. Phys.* **B406** (1993) 187–224.
- [78] S. D. Ellis and D. E. Soper, *Successive combination jet algorithm for hadron collisions*, *Phys. Rev.* **D48** (1993) 3160–3166, [[hep-ph/9305266](#)].
- [79] J. Butterworth, J. Couchman, B. Cox, and B. Waugh, *KtJet: A C++ implementation of the  $k_\perp$  clustering algorithm*, *Computer Physics Communications* **153** (2003), no. 1 85 – 96.
- [80] M. Cacciari, G. P. Salam, and G. Soyez, *The anti- $k_t$  jet clustering algorithm*, *JHEP* **04** (2008) 063, [[arXiv:0802.1189](#)].
- [81] CMS Collaboration, *Algorithms for b Jet identification in CMS*, CMS Physics Analysis Summary CMS-PAS-BTV-09-001, CERN, 2009.
- [82] CMS Collaboration, *Performance of  $\tau$ -lepton reconstruction and identification in CMS*, *JINST* **7** (2012), no. 01.
- [83] CMS Collaboration, *Study of tau reconstruction algorithms using pp collisions data collected at  $\sqrt{s} = 7$  TeV*, CMS Physics Analysis Summary CMS-PAS-PFT-10-004, CERN, 2010.
- [84] CMS Collaboration, *Performance of Jet Algorithms in CMS*, CMS Physics Analysis Summary CMS-PAS-JME-07-003, CERN, 2007.
- [85] CMS Collaboration, *Performance of Track-Corrected Missing Transverse Energy in CMS*, CMS Physics Analysis Summary CMS-PAS-JME-09-010, CERN, 2009.
- [86] R. Wigmans, *Calorimetry*, in *International series of monographs in physics*, vol. 107. Oxford University Press, 2000.
- [87] CMS Collaboration, *Missing transverse energy performance of the CMS detector*, *JINST* **6** (2011) P09001, [[arXiv:1106.5048](#)].
- [88] S. Jadach, J. H. Kühn, and Z. Was, *TAUOLA – a library of Monte Carlo programs to simulate decays of polarized  $\tau$  leptons*, *Comput. Phys. Commun.* **64** (1991), no. 2 275 – 299.
- [89] S. Jadach, Z. Was, R. Decker, and J. H. Kuhn, *The tau decay library TAUOLA: Version 2.4*, *Comput. Phys. Commun.* **76** (1993) 361–380.
- [90] Z. Was, *TAUOLA the library for tau lepton decay, and KKMC / KORALB / KORALZ / ... status report*, *Nucl. Phys. Proc. Suppl.* **98** (2001) 96–102, [[hep-ph/0011305](#)].
- [91] J. Alwall, M. Herquet, F. Maltoni, O. Mattelaer, and T. Stelzer, *MadGraph 5 : Going Beyond*, *JHEP* **1106** (2011) 128, [[arXiv:1106.0522](#)].
- [92] F. Maltoni and T. Stelzer, *MadEvent: Automatic event generation with MadGraph*, *JHEP* **0302** (2003) 027, [[hep-ph/0208156](#)].

- [93] T. Sjöstrand, S. Mrenna, and P. Z. Skands, *PYTHIA 6.4 Physics and Manual*, *JHEP* **0605** (2006) 026, [[hep-ph/0603175](#)].
- [94] P. Nason, *A new method for combining NLO QCD with shower Monte Carlo algorithms*, *JHEP* **0411** (2004) 040, [[hep-ph/0409146](#)].
- [95] S. Frixione, P. Nason, and C. Oleari, *Matching NLO QCD computations with parton shower simulations: the POWHEG method*, *JHEP* **0711** (2007) 070, [[arXiv:0709.2092](#)].
- [96] S. Alioli, P. Nason, C. Oleari, and E. Re, *A general framework for implementing NLO calculations in shower Monte Carlo programs: the POWHEG BOX*, *JHEP* **1006** (2010) 043, [[arXiv:1002.2581](#)].
- [97] GEANT4 Collaboration, *GEANT4—A Simulation toolkit*, *Nucl. Instrum. Meth.* **A506** (2003) 250–303.
- [98] J. Allison, K. Amako, J. Apostolakis, H. Araujo, P. Dubois, et al., *Géant4 developments and applications*, *IEEE Trans. Nucl. Sci.* **53** (2006) 270.
- [99] CMS Collaboration, *Identification and Filtering of Uncharacteristic Noise in the CMS Hadron Calorimeter*, *JINST* **5** (2010) T03014, [[arXiv:0911.4881](#)].
- [100] B. P. Roe, H.-J. Yang, and J. Zhu, *Boosted decision trees, a powerful event classifier*, in *Statistical problems in particle physics, astrophysics and cosmology.*, C05-09-12, pp. 139–142, 2005.
- [101] CMS Collaboration, *Search for a W' boson decaying to a bottom quark and a top quark in pp collisions at  $\sqrt{s} = 7$  TeV*, *Physics Letters B* **718** (2013), no. 4–5 1229 – 1251.
- [102] A. L. Read, *Presentation of search results: the  $CL_s$  technique*, *J. Phys. G: Nucl. Part. Phys.* **28** (2002), no. 2693.
- [103] A. L. Read, *Modified frequentist analysis of search results (the  $CL_s$  method)*, in *CERN-OPEN-2000-205*, 2000.
- [104] T. Junk, *Confidence level computation for combining searches with small statistics*, *Nuclear Instruments and Methods in Physics Research Section A: Accelerators, Spectrometers, Detectors and Associated Equipment* **434** (1999), no. 2–3 435 – 443.
- [105] M. Chen and A. Korytov, “Limits and Significance.” <http://mschen.web.cern.ch/mschen/Lands/>.
- [106] ATLAS Collaboration, CMS Collaboration, and LHC Higgs Combination Group, *Procedure for the lhc higgs boson search combination in summer 2011*, Tech. Rep. CMS-NOTE-2011-005, ATL-PHYS-PUB-2011-11, CERN, 2011.
- [107] M. J. Kortelainen, *private communication*, June 25, 2013.

## **Part IV**

# **Appendix**

## A Signal trigger specifications

The trigger proceeds hierarchically on several levels, meaning that only those events that pass the Level-1 requirements are considered at Level-2 and so on. The requirements for an event to pass each level are listed below. N.B.: A *central jet* refers to a jet with pseudorapidity  $2.1 < |\eta| < 3.0$ , meaning that its direction is very close to the beam.

### Low-level trigger

**Level-1** Tau-jet selection using only calorimeter information. Corrected jet energies are used; the uncorrected energies corresponding to 52 GeV and 68 GeV are 32 GeV and 40 GeV, respectively.

- L1  $\tau$ -jet with  $E_T > 52$  GeV OR L1 central jet with  $E_T > 68$  GeV (runs  $\leq 167913$ )
- L1  $\tau$ -jet with  $E_T > 52$  GeV OR L1 central jet with  $E_T > 52$  GeV AND L1  $E_T^{\text{miss}} > 30$  GeV (runs  $\geq 170722, \leq 180252$ )

### High-level trigger, tau part

#### Level-2

- Reconstruction of a L2 calorimeter jet with radius 0.2 that must match the L1  $\tau$ -jet and have  $E_T > 35$  GeV,  $|\eta| < 3$

#### Level-2.5

- L2.5 fixed cone Particle Flow  $\tau$  matching the L2 jet object, with  $p_T > 35$  GeV and  $|\eta| < 2.5$
- The L2.5 leading track of the  $\tau$ -jet must have  $p_T > 20$  GeV

#### Level-3

- L3 charged hadron and gamma isolation with matching cone of 0.2, signal cone of 0.15, and isolation cone of 0.5. The requirement was that there should be zero candidates passing the following selection:
  - Tight isolation with charged hadron  $p_T > 1$  GeV and gamma  $E_T > 1.5$  GeV (runs  $\leq 173198$ )
  - Medium isolation with charged hadron  $p_T > 1$  GeV (runs  $\geq 173236$ )

### High-level trigger, missing transverse energy part

**Level-2** The forward hadron calorimeter was excluded in the L2  $E_T^{\text{miss}}$  calculation for runs  $\leq 167913$ , and included for runs  $\geq 170722$ .

- L2  $E_T^{\text{miss}} > 45$  GeV (runs  $\leq 165633$ )
- L2  $E_T^{\text{miss}} > 60$  GeV (runs  $\geq 165970$ )

## B Invariant mass distributions using different selection methods

The invariant mass distributions obtained using each of the six different selection methods are shown here, in Figures B.1 to B.6. In all cases, only events with a positive discriminant are included, as they are the only ones in which the  $p_\nu^z$  selection needs to be done. All selection methods are explained in Section 9.4. The max- $\Delta\eta$  method was chosen to be used for the analysis.

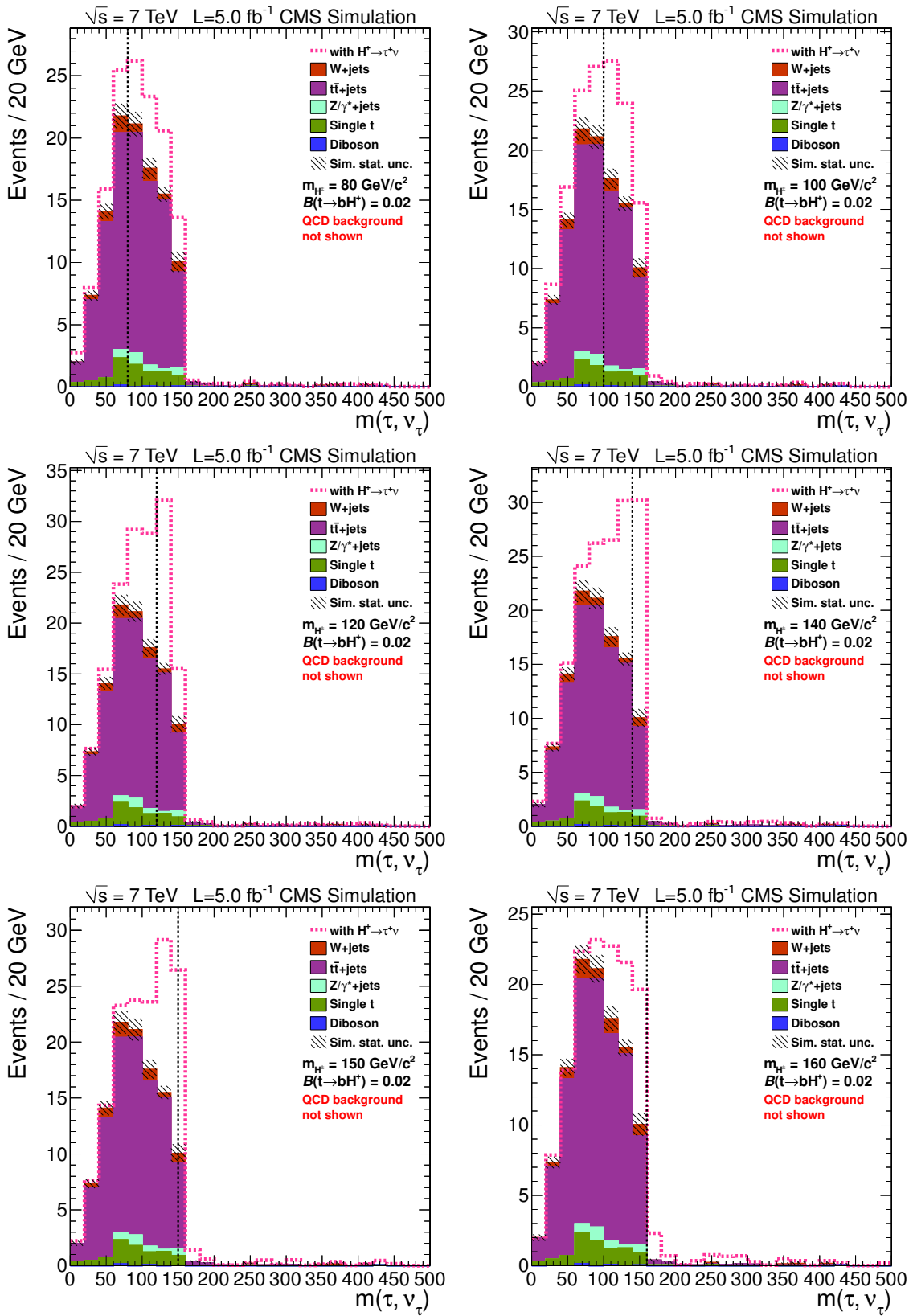


Figure B.1: Invariant mass distributions obtained using the max- $|p_\nu^z|$  selection method.

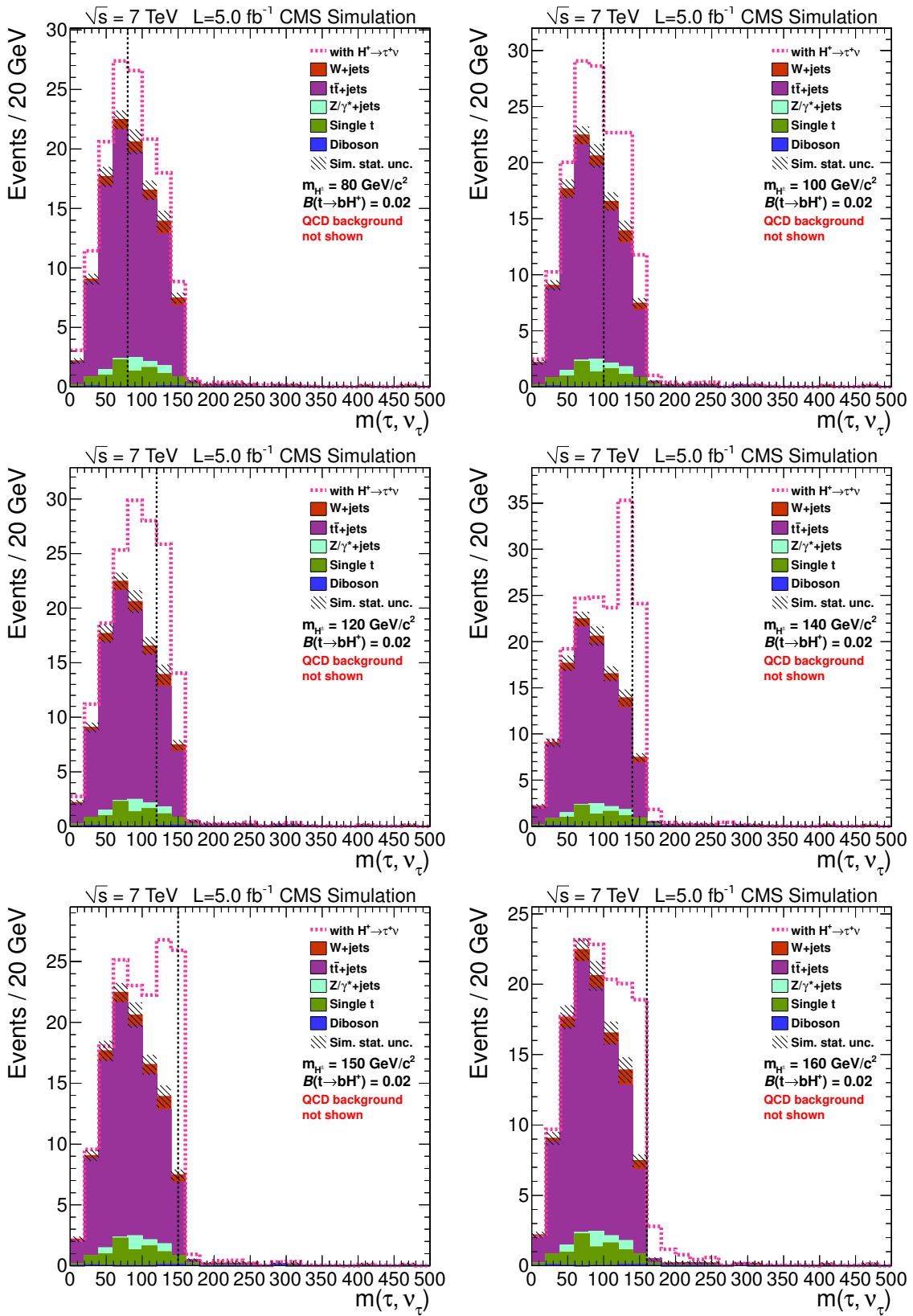


Figure B.2: Invariant mass distributions obtained using the min- $|p_\nu^z|$  selection method.

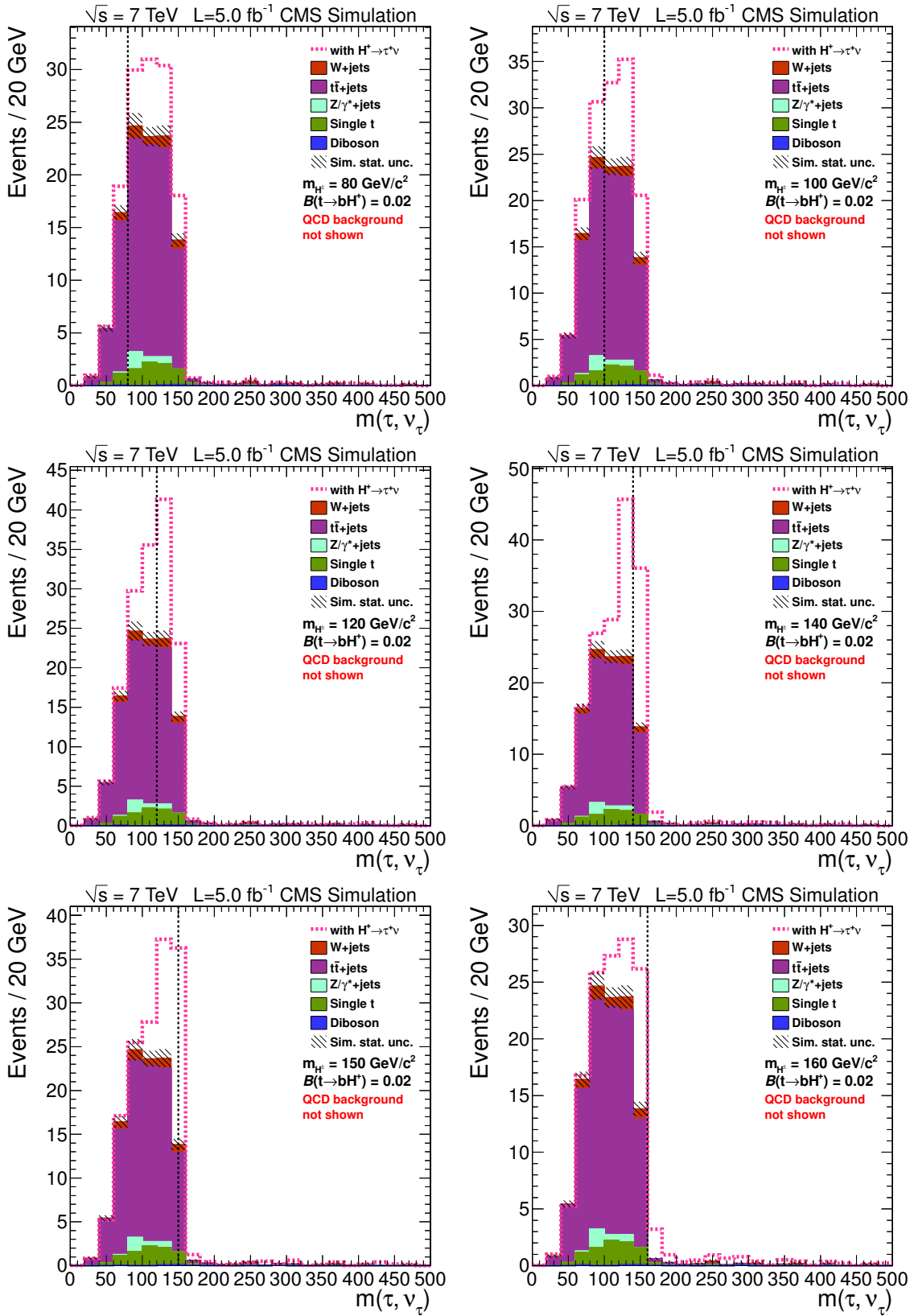


Figure B.3: Invariant mass distributions obtained using the max- $\xi$  selection method. **This method was chosen for the analysis.**

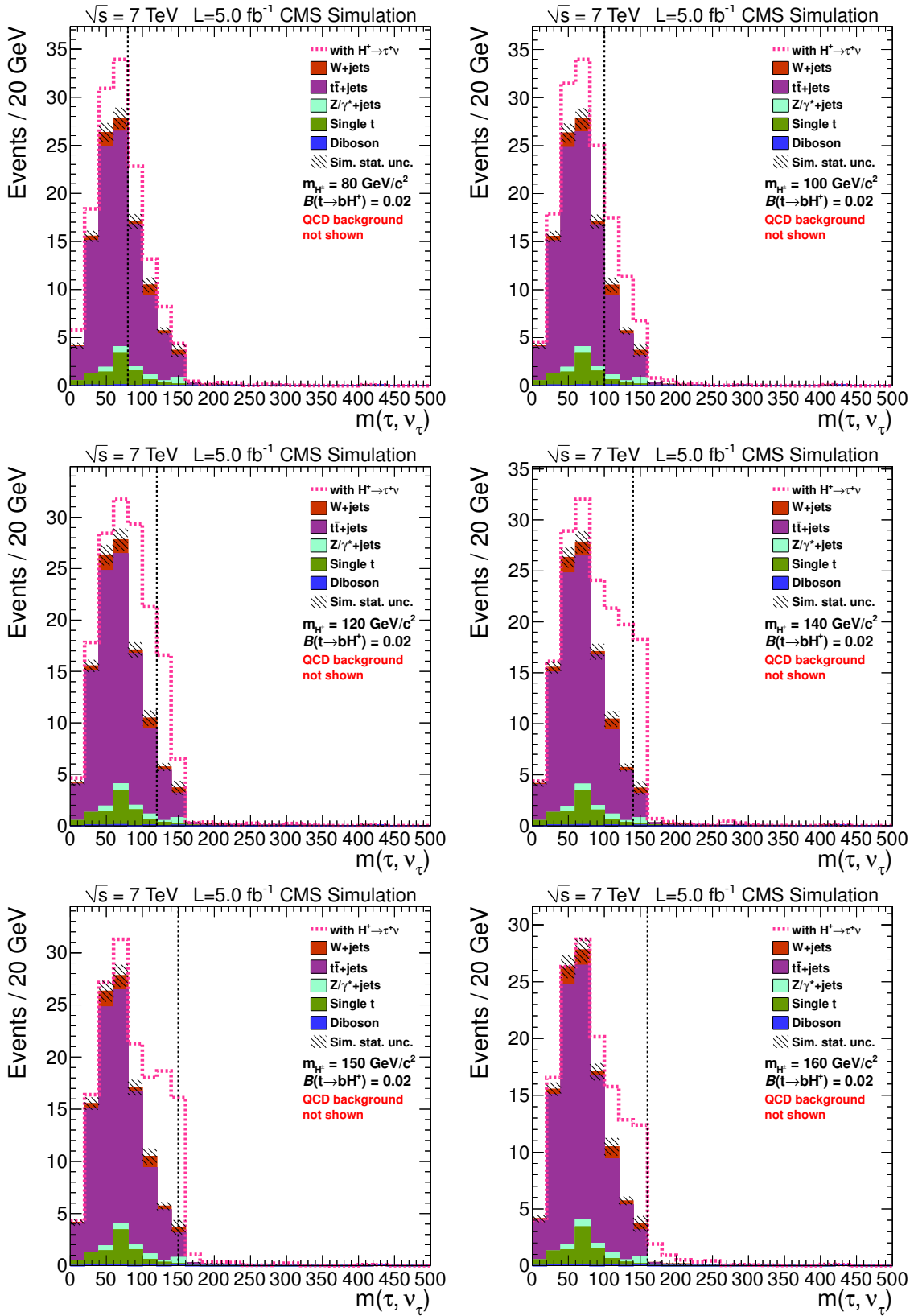


Figure B.4: Invariant mass distributions obtained using the min- $\xi$  selection method.

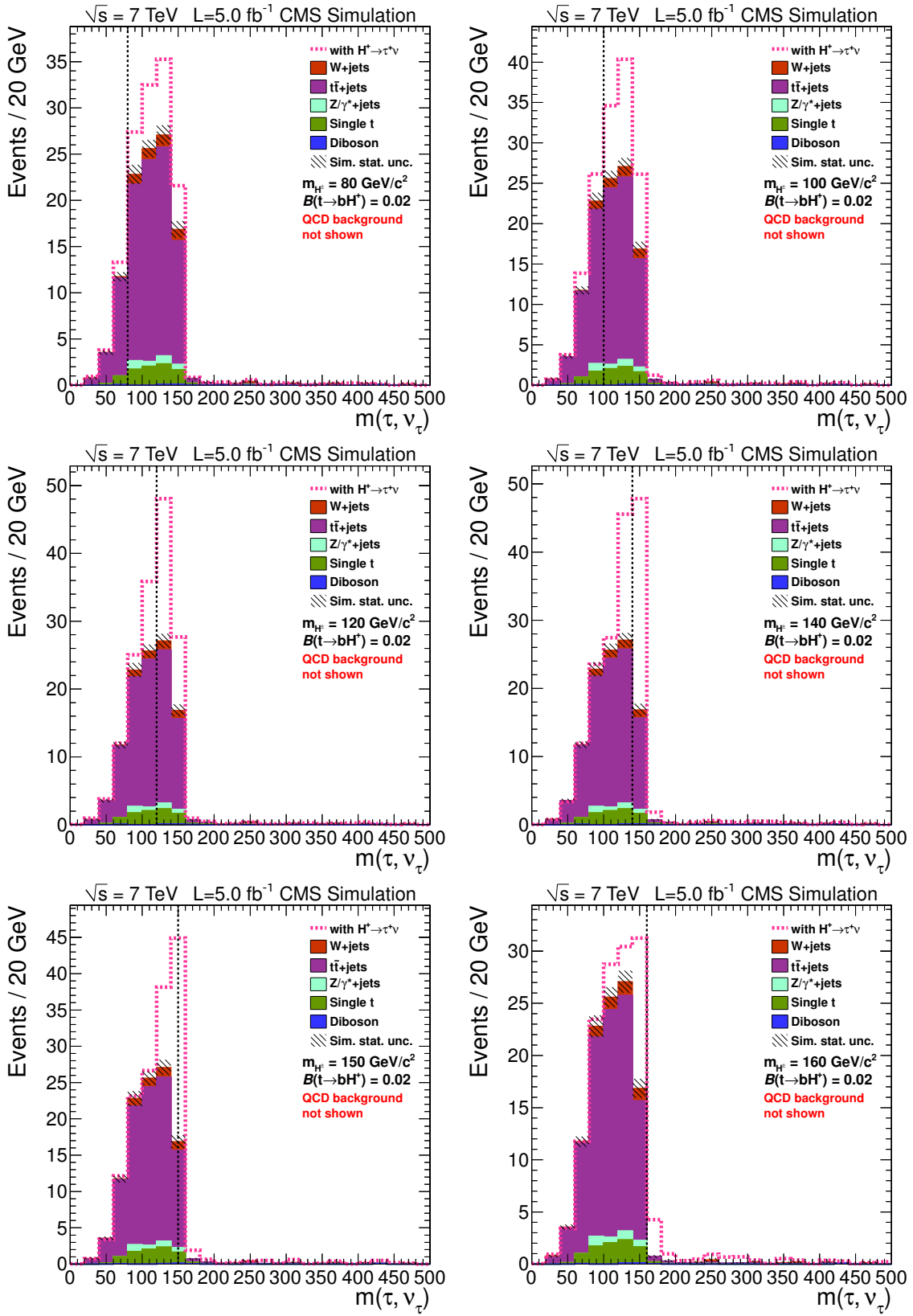


Figure B.5: Invariant mass distributions obtained using the max- $\Delta\eta$  selection method. This selection method was chosen to produce the final results.

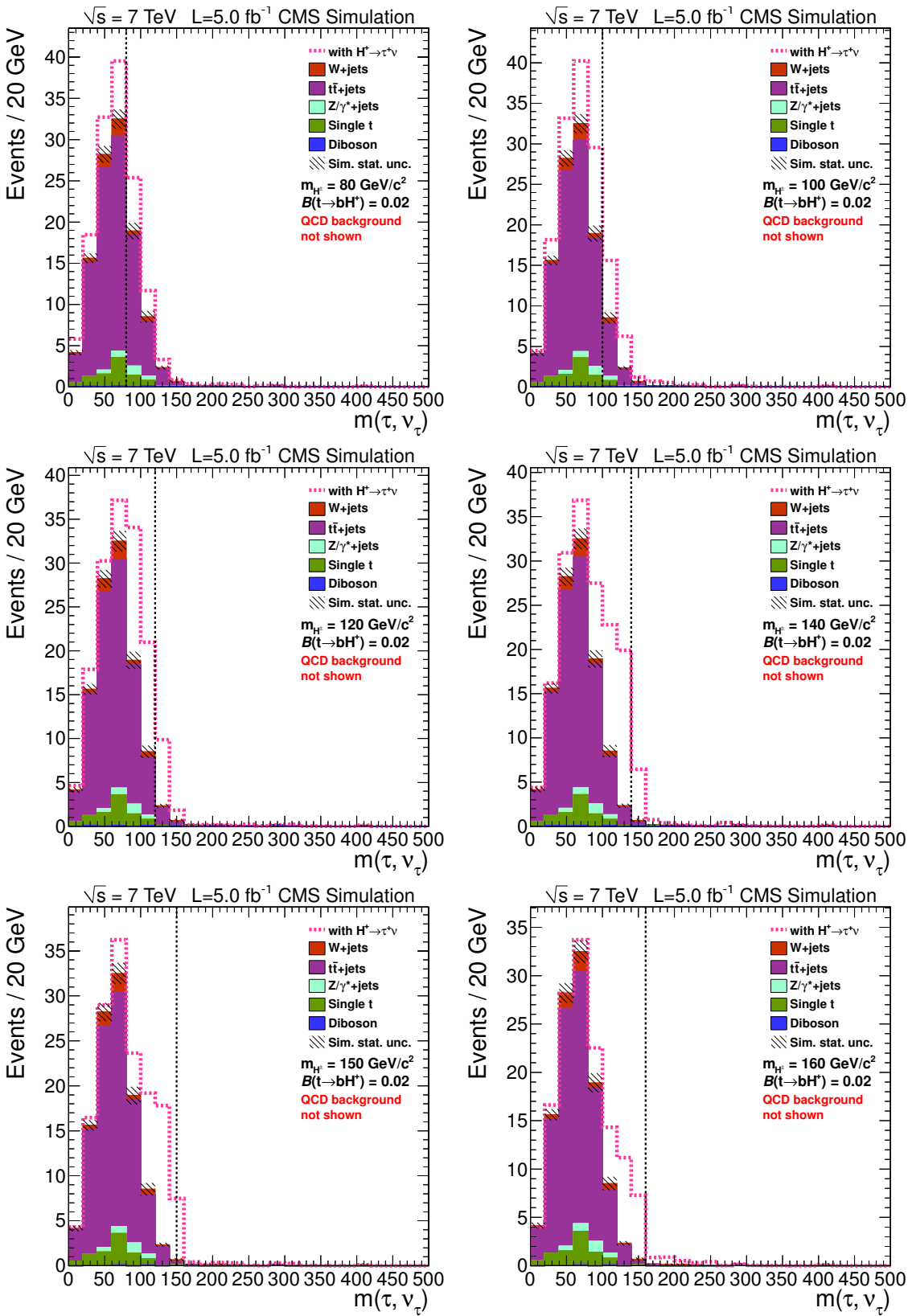


Figure B.6: Invariant mass distributions obtained using the min- $\Delta\eta$  selection method.

## C Transverse mass distributions

The transverse mass distribution of the tau-and-neutrino system for different  $H^\pm$  masses is shown in Figure C.1.

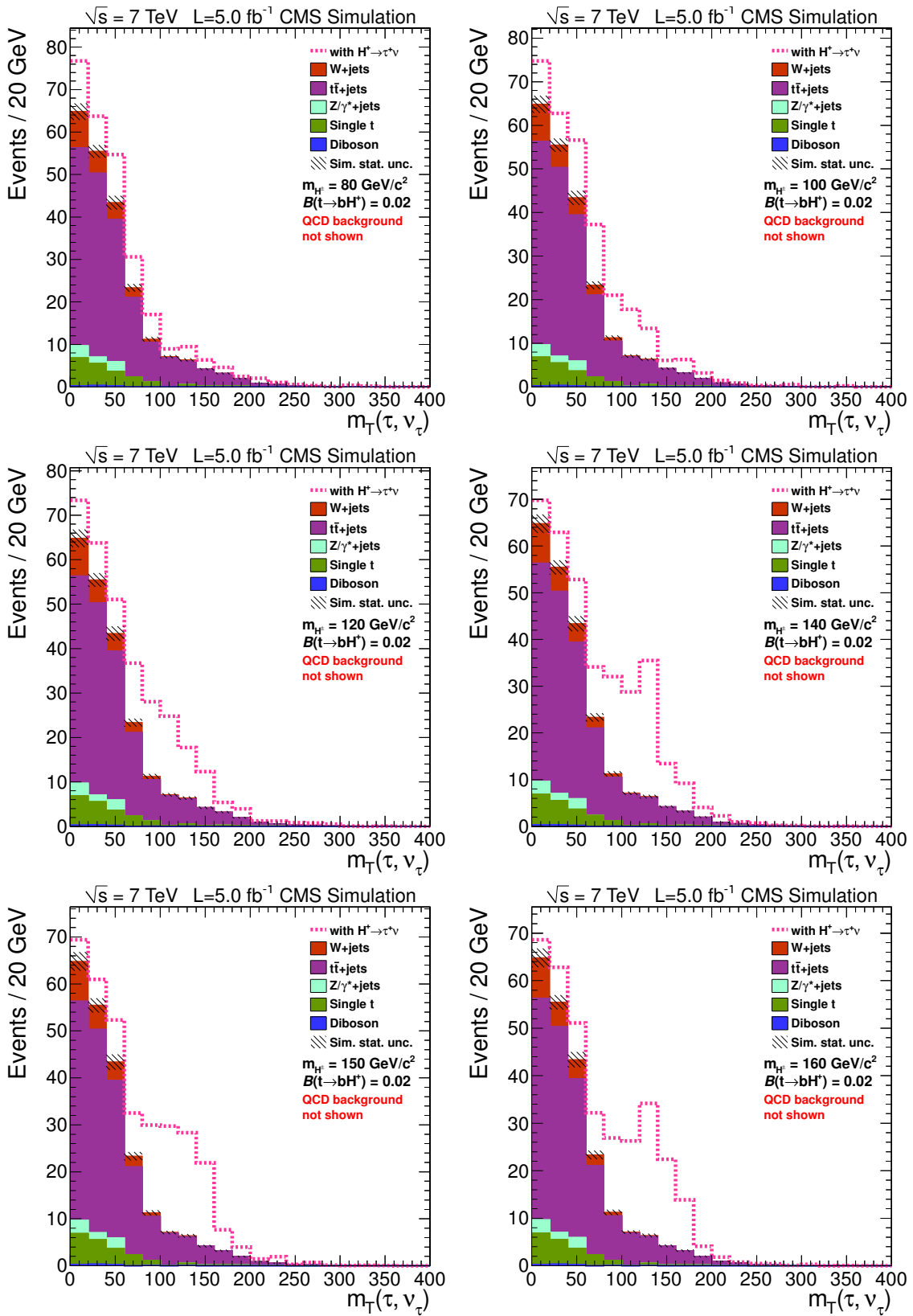


Figure C.1: Transverse mass distributions.

## D Invariant mass fits

Fits of the invariant mass distributions of simulated  $H^\pm$  signal events using Gaussian and Breit-Wigner distributions are shown in Figs. D.1 and D.2, respectively. The distributions were obtained using the *medium* top invariant mass requirement. The figures correspond to the data shown in Table 10.2. The fitted values of the three parameters in the distributions are shown in the figures, where `norm.` represents the normalization of the curve, `mean` is the mean (or, strictly speaking, median in the case of a Breit-Wigner distribution), and `width` describes the width of the distribution. Also shown is the value of  $\chi^2$  per number of degrees of freedom in the fit.

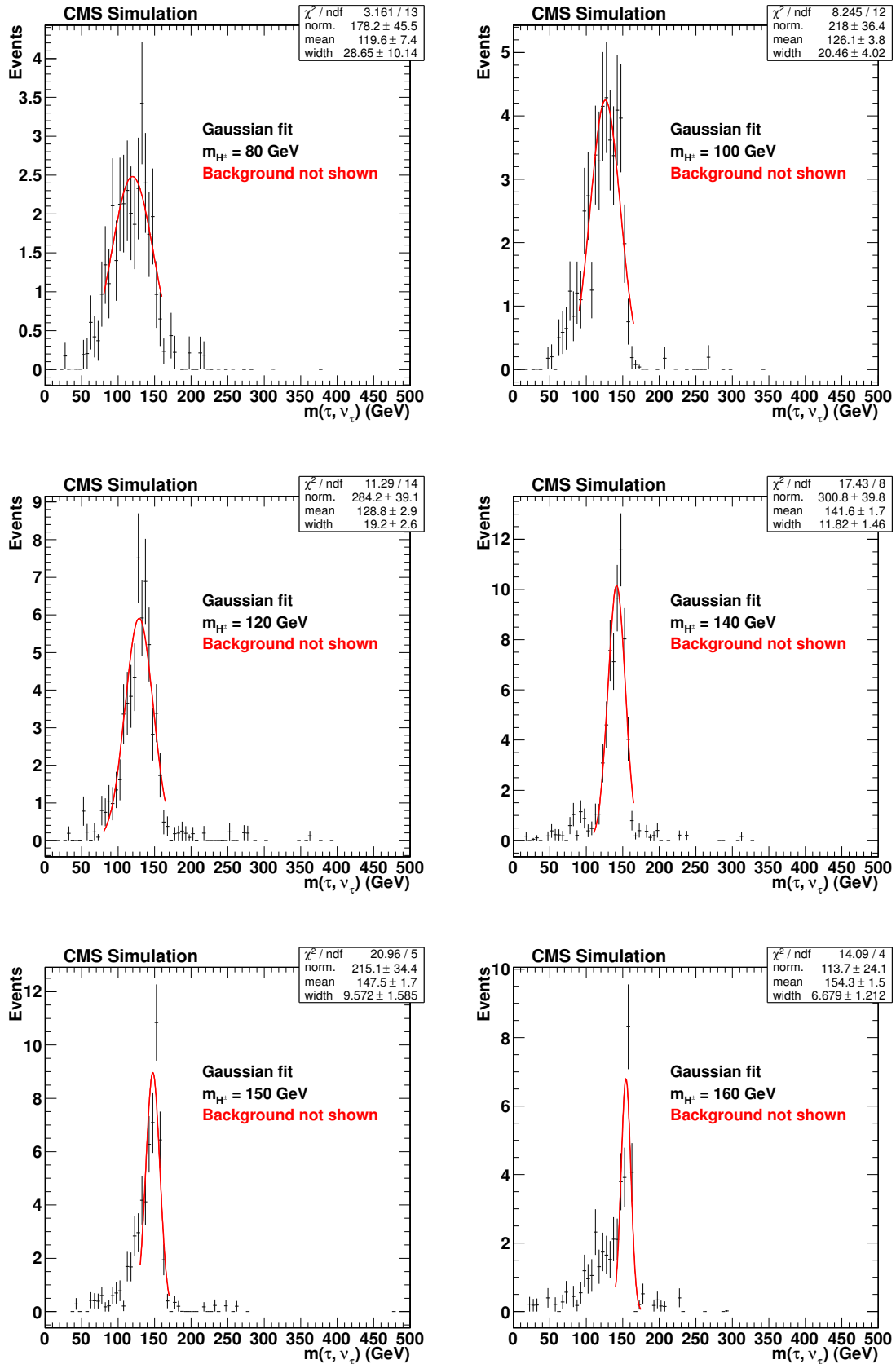


Figure D.1

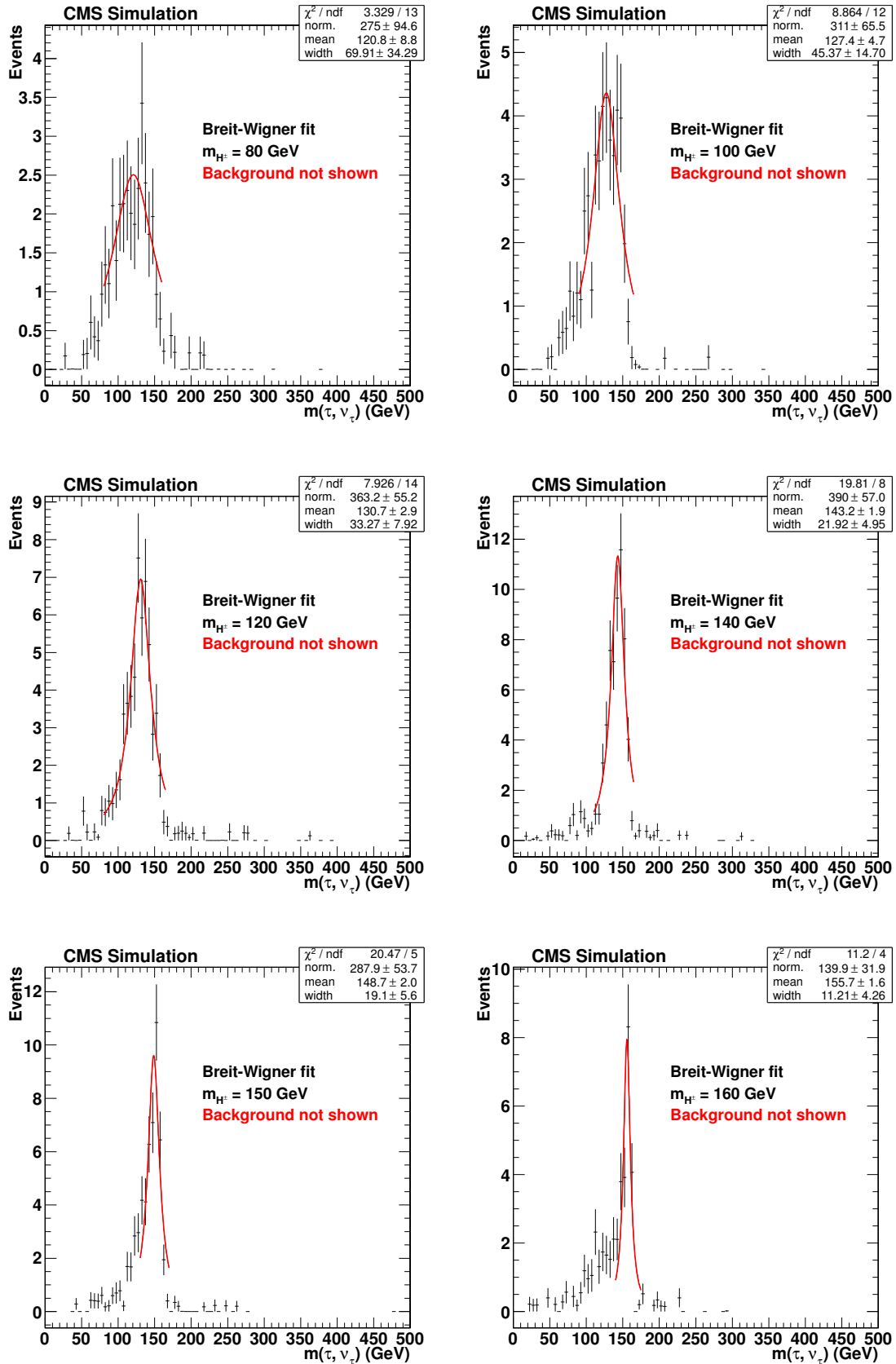


Figure D.2

## E Summary for non-physicists

The research presented in this thesis is in experimental particle physics, a field of science that is concerned with studying what the elementary particles that all matter is made of are and how they behave. Fundamental research in particle physics has relatively few practical (though some) practical applications, though many of the technologies developed for it are also adapted elsewhere and benefit human society directly. More importantly in the long run, particle physics is one of the most ambitious endeavours to understand how Nature works and what the Universe is made of.

The author's work is part of an analysis that uses data collected by the CMS experiment of the Large Hadron Collider. The role of the analysis is to search for a new kind of particle, the electrically charged Higgs boson. Charged Higgs bosons are hypothetical particles, whose existence is predicted by some theories. We try to either show their existence or their non-existence to a large degree of certainty. To do this, a careful statistical data analysis is necessary, consisting of many different parts whose functioning needs to be tested, understood, and constantly validated. Six people currently work on the analysis long-term, with students regularly joining the group for a few months to do a research project.

If charged Higgs bosons exist, they are almost certainly very short-lived, meaning that they decay to other particles right after being produced. This means that they have to be produced right where they are to be studied. Producing short-lived particles can be done by colliding other particles with a lot of collision energy. Collisions between elementary particles are very different from the collisions of common objects that are known from everyday experience. The initial particles can disappear and new particles be produced instead. It is a statistical process, meaning that the outcome is random, but each possible outcome has some fixed probability of occurring. The probabilities of some processes to happen are known more or less well. Others are only known to be smaller than some value, such as the probability of a charged Higgs boson being produced. Measuring this probability or a smaller upper limit for it is the goal of the analysis. If it turns out to be essentially zero, we can have large certainty that there are no charged Higgs bosons. Because the collisions are statistical processes, great numbers of collisions must be analyzed in order to reach conclusions.

Our analysis allows the search for charged Higgs bosons that decay to a tau lepton and a neutrino. From among the collision events, candidate events that look like they could have contained a charged Higgs boson are selected. Some known processes can also produce events that look very similar to what events with a charged Higgs boson might look like; they form the so-called background. The background must be measured or estimated based on computer simulations.

A quantity called the transverse mass is calculated using the energies and momenta (amounts of movement) of the tau lepton and the neutrino that might come from the decay of a charged Higgs boson. If charged Higgs bosons exist, there should be an excess of events with transverse mass near some value with respect to the background. This excess is called a signal peak.

As an alternative to the transverse mass, one can also calculate the invariant mass of the tau lepton and neutrino to look for a signal peak. Calculating ('reconstructing') the invariant mass is less straightforward than the transverse mass, because more approximations and assumptions need to be made. On the other hand, the invariant mass includes more of

the available experimental information and might therefore provide a better sensitivity to a possible signal.

It was the author's task to develop a method for calculating the invariant mass and finding out if it provides a better signal sensitivity than the transverse mass. In a preliminary data analysis, it was shown that the calculation method is adequate and that the invariant mass does provide a better signal sensitivity. This means that the analysis might be done using the invariant mass instead of the transverse mass in the future. Perhaps they can even be used simultaneously to give even better sensitivity, but this still needs to be tested.

## F Yhteenveto ei-fyysikoille

Tässä työssä esitetty tutkimus on kokeellista hiukkasfysiikkaa. Hiukkasfysiikka on luonnonpiteellinen ala, jonka päämääräänä on selvittää, mitkä ovat alkeishiukkaset, joista kaikki aine koostuu, sekä miten ne käyttäytyvät luonnossa. Perustavanlaatuisen hiukkasfysiikan tutkimuksella on suhteellisen vähän (mutta kuitenkin joitakin) käytännön sovelluksia. Toisaalta monia sitä varten kehitetyistä teknologioista on myöhemmin sovellettu muualakin ihmiskunnan hyödyksi. Pitkällä tähtäimellä tärkeämpi tosiasia lienee kuitenkin, että hiukkasfysiikka on yksi kunnianhimoisimmista yrityksistä ymmärtää, miten luonto toimii ja mistä maailmankaikkeus koostuu.

Tekijän työ on osa analyysia, joka käyttää suuren hadronitörmäyttimen (engl. *Large Hadron Collider*) CMS -kokeen tallentamaa dataa. Analyysin rooli on etsiä uudenlaista hiukkasta, sähköisesti varattua Higgsin bosonia. Varatut Higgsin bosonit ovat hiukkasia, joiden olemassaolo jotkut teoriat ennustavat, mutta joita ei ole vielä havaittu. Me yritämme osoittaa joko niiden olemassaolon tai olemassaolemannuuden suurella varmuudella. Tämän saavuttamiseksi tarvitaan huolellinen tilastollinen analyysi, joka koostuu monista eri palaista, joiden toimivuutta täytyy varmistaa, ymmärtää sekä jatkuvasti valvoa. Tällä hetkellä analyysia on tekemässä pitkääkäisesti kuusi henkilöä, joiden lisäksi opiskelijoita liittyy säännöllisesti mukaan ryhmään muutamaksi kuukaudeksi tekemään tutkimusprojektia.

Jos varattuja Higgsin bosoneita on olemassa, niillä on lähes varmasti erittäin lyhyt elinaika. Tämä tarkoittaa, että ne hajoavat muiksi hiukkasiksi nopeasti sen jälkeen, kun ne syntyvät. Tästä syystä niitä täytyy tuottaa siellä, missä niitä halutaan tutkia. Lyhytkäisiä hiukkasia voi tuottaa törmäytämällä muita hiukkasia suurella energialla. Alkeishiukkasten väliset törmäykset ovat hyvin erilaisia kuin arjesta tutut jokapäiväisten esineiden törmäykset. Alkuperäiset hiukkaset voivat kadota ja uusia hiukkasia syntyy. Se on tilastollinen prosessi siinä mielessä, että lopputulos on satunnainen, mutta jokaisella mahdollisella lopputulalla on joku tietty todennäköisyys esiintyä. Joidenkin prosessien tapahtumistodennäköisydet tiedetään enemmän tai vähemmän tarkasti. Toisten todennäköisyysille tiedetään vain joku ylräaja, kuten myös todennäköisyydelle tuottaa varattu Higgsin bosoni. Tämän todennäköisyyden laskeminen tai ylräajan asettaminen sille on meidän analyysin päämäärä. Koska törmäykset ovat luonteeltaan tilastollisia, täytyy analysoida suuri määrä törmäyksiä ennen kuin on mahdollista vetää johtopäätöksiä.

Analyysimme sallii varattujen Higgsin bosoneiden etsimisen, jotka hajoavat tau-leptoniksi ja neutriinoksi. Kaikista törmäystapahtumista valitaan sellaiset ehdokkaat, jotka näyttävät siltä, että niissä on saattanut esiintyä varattu Higgsin bosoni. Jotkut tunnetut prosessit tuottavat tapahtumia, jotka näyttävät hyvin samanlaisilta kuin miltä varatun Higgsin bosonin sisältävät saattavat näyttää. Nämä muodostavat niin sanotun taustan. Tausta täytyy mitata kokeellisesti tai mallintaa tietokonesimulaatioiden perusteella.

Mahdollisesti varatun Higgsin bosonin hajoamisesta tulevan tau-leptonin ja neutriinon energioista ja liikemääristä lasketaan suure, joka sanotaan poikittaiseksi massaksi. Jos varattuja Higgsin bosoneita on olemassa, meidän pitäisi havaita odotettua enemmän tapahtumia, joissa poikittainen massan on lähellä joitain tiettyä arvoa suhteessa taustaan. Tätä ylimäärästä sanotaan signaalihuipuksi.

On myös mahdollista laskea tau-leptonin ja neutriinon invariantti massa vaihtoehtona poikittaiseen massaan. Sen laskeminen ("rekonstruoiminen") on hankalampaa kuin poikittaisen massan, koska se vaatii useampia likiarvoistuksia ja oletuksia. Toisaalta invariantti

massa sisällyttää enemmän kokeellisesti määritettyä tietoa ja saattaa sen takia parantaa analyysin herkkyyttä mahdollisen signaalin etsimisessä.

Tekijän tehtävä oli kehittää keinot laskea invariantti mass sekä selvittää, antaako se suuremman signaaliherkkyyden kuin poikittainen massa. Alustavassa data-analyysissä pystytettiin osoittamaan, että laskemiskeino antaa järkeviä tuloksia ja että invariantti massa parantaa signaalherkkyyttä. Tämä tarkoittaa, että analyysissä saatetaan jatkossa käyttää invarianttia massaa poikittaisen massan sijaan. Mahdollisesti molempia voidaan jopa käyttää yhdessä yhä paremman herkkyyden saavuttamiseksi, mutta tästä täytyy vielä tutkia.

## G Zusammenfassung für Nichtphysiker|innen

Bei der Forschung, von der in dieser Abschlussarbeit berichtet wird, handelt es sich um experimentelle Elementarteilchenphysik, einen Bereich der Naturwissenschaften, der zu klären versucht, was die Elementarteilchen sind, aus denen alle Materie besteht, und wie sie sich verhalten. Grundlegende Forschung in der Teilchenphysik hat relativ wenige (wenngleich ein paar) praktische Anwendungen, aber viele der Technologien, die ursprünglich für sie entwickelt wurden, finden jetzt auch anderswo Anwendung und liefern der Menschheit so direkten Nutzen. Die auf lange Sicht wichtigere Tatsache ist jedoch, dass die Teilchenphysik eines der ehrgeizigsten Unterfangen mit dem Ziel darstellt, zu verstehen, wie die Natur funktioniert und woraus das Universum besteht.

Die Arbeit des Autoren ist ein Beitrag zu einer Analyse, welche Daten auswertet, die im CMS-Experiment des Großen Hadronen-Speicherrings (engl. *Large Hadron Collider*) gesammelt wurden. Die Rolle der Analyse ist es, nach elektrisch geladenen Higgs-Bosonen, einer neuen Art von Elementarteilchen, zu suchen. Die Existenz von geladenen Higgs-Bosonen wird von manchen Theorien vorausgesagt. Wir versuchen, entweder ihre Existenz oder ihre Nicht-Existenz mit großer statistischer Sicherheit zu belegen. Damit dies gelingt, ist eine sorgfältige statistische Datenanalyse notwendig, die aus vielen Bausteinen besteht, deren Funktionieren sichergestellt, verstanden und immer wieder überprüft werden muss. Zur Zeit arbeiten sechs Leute dauerhaft an der Analyse. Zusätzlich beteiligen sich regelmäßig Studenten für ein paar Monate daran, um ein Forschungsprojekt durchzuführen.

Falls geladene Higgs-Bosonen existieren, haben sie so gut wie sicher eine sehr kurze Lebensdauer. Das bedeutet, dass sie sofort nach ihrer Entstehung in andere Teilchen zerfallen. Daher müssen sie dort produziert werden, wo sie untersucht werden sollen. Kurzlebige Teilchen können erzeugt werden, indem man andere Teilchen mit viel Energie zusammenstoßen lässt. Zusammenstöße zwischen Elementarteilchen unterscheiden sich sehr von Zusammenstößen von Gegenständen, wie man sie aus dem Alltag kennt. Die ursprünglichen Teilchen können verschwinden und neue Teilchen erzeugt werden. Es handelt sich um einen statistischen Prozess, was bedeutet, dass das Ergebnis zufällig ist, wobei jedes mögliche Ergebnis eine bestimmte Wahrscheinlichkeit hat, einzutreffen. Die Wahrscheinlichkeiten mancher Prozesse sind mehr oder weniger gut bekannt. Von manchen anderen weiß man hingegen nur, dass sie kleiner als eine bestimmte Obergrenze sind. Dies gilt zum Beispiel für die Wahrscheinlichkeit, geladene Higgs-Bosonen zu erzeugen. Sie zu messen oder eine niedrigere Obergrenze für sie zu messen ist das Ziel unserer Analyse. Falls sich herausstellt, dass sie sehr nah bei null liegt, können wir mit relativ großer Sicherheit sagen, dass geladene Higgs-Bosonen nicht existieren. Weil die Teilchenkollisionen statistische Prozesse sind, muss eine große Zahl an Kollisionen untersucht werden, um Schlüsse ziehen zu können.

Unsere Analyse erlaubt die Suche nach geladenen Higgs-Bosonen, die zu einem Tauon und einem Neutrino zerfallen. Aus den Kollisionsergebnissen wurden Kandidaten-Ereignisse ausgewählt, die möglicherweise ein geladenes Higgs-Boson enthalten haben könnten. Einige bekannte Prozesse können ebenfalls Ereignisse erzeugen, welche denen sehr ähneln, die geladene Higgs-Bosonen erzeugen könnten. Diese Prozesse bilden den sogenannten Untergrund. Die Untergrund muss gemessen oder mithilfe von Computersimulationen abgeschätzt werden.

Um nach einem möglichen Signal zu suchen, wird eine Größe namens transversale Masse

berechnet. Dazu wird die Energie und der Impuls (die Bewegungsmenge) des möglicherweise aus dem Zerfall eines geladenen Higgs-Bosons stammenden Tauons und Neutrinos verwendet. Falls geladene Higgs-Bosonen existieren, sollte ein Überschuss an Ereignissen mit einer transversalen Masse um einen bestimmten (unbekannten) Wert gegenüber dem Untergrund zu beobachten sein. Diesen Überschuss nennt man eine Signal-Spitze (engl. *signal peak*).

Alternativ zur transversalen Masse kann auch die invariante Masse des Tauons und Neutrinos berechnet werden, um damit nach einer Signal-Spitze zu suchen. Die Berechnung („Rekonstruierung“) der invarianten Masse ist schwieriger als die der transversalen Masse, da mehr Näherungen und Annahmen nötig sind. Andererseits beinhaltet die invariante Masse mehr von den experimentell verfügbaren Informationen und bietet deshalb vielleicht eine größere Empfindlichkeit auf ein mögliches Signal.

Die Aufgabe des Autors war es, eine Methode zur Berechnung der invarianten Masse zu entwickeln sowie herauszufinden, ob diese eine größere Signalempfindlichkeit ermöglicht als die transversale Masse. In einer vorläufigen Datenauswertung wurde gezeigt, dass die entwickelte Methode angemessene Ergebnisse liefert und dass die invariante Masse größere Signalempfindlichkeit bietet. Das bedeutet, dass die Analyse in Zukunft möglicherweise die invariante statt der transversalen Masse nutzen wird. Vielleicht lassen sich die beiden auch kombinieren, um eine noch größere Empfindlichkeit zu erreichen; doch dies muss erst noch untersucht werden.